INFLUENCE OF RETROGRESSION AND RE-AGING TREATMENT ON MICROSTRUCTURE, MECHANICAL AND FATIGUE CRACK GROWTH BEHAVIOR OF ALUMINUM ALLOY 7010

Thesis

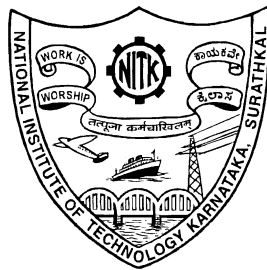Submitted in partial fulfillment of the requirements for the degree of

DOCTOR OF PHILOSOPHY

By

NANDANA M. S.

(MT14F10)

DEPARTMENT OF METALLURGICAL AND MATERIALS ENGINEERING

NATIONAL INSTITUTE OF TECHNOLOGY KARNATAKA, SURATHKAL, MANGALORE - 575025
OCTOBER 2020

DECLARATION

I hereby *declare* that the Research Thesis entitled "INFLUENCE OF RETROGRESSION AND RE-AGING TREATMENT ON MICROSTRUTCURE, MECHANICAL AND FATIGUE CRACK GROWTH BEHAVIOR OF ALUMINUM ALLOY 7010" which is being submitted to the **National Institute of Technology Karnataka, Surathkal** in partial fulfilment of the requirements for the award of the Degree of Doctor of **Philosophy** in the **Department of Metallurgical and Materials Engineering** is a *bonafide report of the research work carried out by me*. The material contained in this Research Thesis has not been submitted to any University or Institution for the award of any degree.

Nanday

NANDANA M S

Register Number: 148058MT14F10
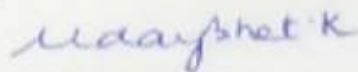
Department of Metallurgical and

Materials Engineering

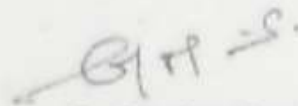Place: NITK Surathkal,

Date: 17|10|2020

CERTIFICATE

This is to certify that the Research Thesis entitled "INFLUENCE OF RETROGRESSION AND RE-AGING TREATMENT ON MICROSTRUTCURE, MECHANICAL AND FATIGUE CRACK GROWTH BEHAVIOR OF ALUMINUM ALLOY 7010" submitted by Mr. Nandana M S (Register Number: 148058MT14F10) as the record of the research work carried out by him, *is accepted as the Research Thesis submission* in partial fulfilment of the requirements for the award of degree of **Doctor of Philosophy**.

Research Guides

Prof. Udaya Bhat K.

Professor

Dr. Manjunatha C M.

Chief Scientist

Chairman – DRPC

Dept. of Metallurgical and Materials Engineering, NITK Surathkal

Srinivasnagar 575025, Mangalore, India

Dedicated

to

My Wife

ACKNOWLEDGEMENTS

ABSTRACT

The high strength aluminum alloys are widely used in construction of aircrafts structural components. From the safety and durability point of view these structures need to be highly damage tolerant under service loads. The damage tolerance behavior of these alloys when treated in retrogression and re-aging condition (RRA) is rarely studied. In the present research work the heat treatment of aluminum alloy 7010 is carried out at different aging conditions to study its influence on microstructure and mechanical properties. The mechanical properties and fatigue crack growth behavior is correlated to the modified microstructure of the alloy. The alloy is heat treated in standard peak-aging (T6), retrogression and re-aging (RRA) and over-aging (T7451) conditions. The microstructure is characterized by optical microscopy (OM), scanning electron microscopy (SEM), transmission electron microscopy (TEM), X-ray diffractometry (XRD) and differential scanning calorimetry (DSC). The mechanical characterization of the alloys is performed by conducting hardness tests, standard tensile tests and fracture toughness tests. The fatigue crack growth performance of the alloy in different aging conditions is determined by conducting constant amplitude (CA) fatigue crack growth rate (FCGR) tests and spectrum fatigue crack growth tests under fighter aircraft loading standard for fatigue evaluation (FALSTAFF). The fatigue crack growth behavior is also predicted adopting a two parameter crack growth law using already determined CA FCGR data. The results are compared with the experimentally determined spectrum fatigue crack growth behavior under FALSTAFF loading. The alloys are characterized for electrochemical corrosion behavior and exfoliation corrosion (EXCO) behavior. The alloy microstructure in RRA condition consists of two different kinds of matrix precipitates, namely large sized η' (MgZn$_2$) of size 15-20 nm along with the presence of metastable precipitates η' (MgZn$_2$) of size 5-8 nm. Unlike RRA treated alloy, T6 alloy microstructure consists of only η' (MgZn$_2$) of size 2-4 nm. The grain boundary precipitates in RRA treated condition is more similar to that of the over-aged condition i.e., discontinuous in nature unlike the continuous one present in the T6 condition of alloy. The retrogression performed at 200 ˚C for about 20 minutes of duration is optimized to obtain equivalent tensile strength as that of the T6 alloy. The FCGR behavior of RRA

treated alloy exhibited a considerable reduction in crack growth rate in the near-threshold regime compared to the T6 treated alloy. The crack growth reduction by about 2-3 time in RRA alloy along with increase in threshold SIF (ΔK_{th}) of about 0.6-1 MPa√m is evident. The fatigue crack surface roughness is measured to be higher in the near-threshold regime of the RRA alloy. The alloy microstructure consisting of increased inter-precipitate distance is correlated to the increased resistance to fatigue crack growth rate. The observed behavior of improved crack growth resistance has lead to higher damage tolerance of the RRA alloy under service loads. An improvement of fatigue crack growth life by about 22 % is evident. The corrosion and EXCO performance of the RRA alloy is better compared to the standard T6 treated alloy. The chemistry of grain boundary precipitates characterized by using TEM-EDS determined a higher content of copper on grain boundary precipitate (η) which leads to exfoliation corrosion resistance of the alloy.

CONTENTS

LIST OF FIGURES

LIST OF TABLES

NOMENCLATURE

ASTM	American Iron and Steel Institute
EDS	Energy Dispersive Spectroscopy
SAED	Selected Area Electron Diffraction
SEM	Scanning Electron Microscopy
TEM	Transmission Electron Microscopy
XRD	X-ray Diffraction
FCC	Face Centered Cubic
SCC	Stress Corrosion Cracking
RRA	Retrogression and Re-Aging
FALSTAFF	Fighter Aircraft Loading Standard For Fatigue evaluation
DSC	Differential Scanning Calorimetry
CT	Compact Tension
EXCO	Exfoliation Corrosion

CHAPTER 1

INTRODUCTION

Aluminum is one of the abundantly used materials for engineering applications. 8 % (by weight) of earth crust is occupied by aluminum. Aluminum alloys find their applications as engineering materials in load bearing structures of aerospace and automobiles, due to the combination of distinct mechanical and physical properties. Being one of the lightweight materials exhibiting high specific strength, makes it suitable for application in aircrafts and spacecrafts.

Aluminum in its pure form has a strength value of about 90 MPa. Hence, its usefulness for structural application in its pure form is limited. However, much larger strength could be achieved by incorporation of small quantities of alloying elements, like copper, zinc, manganese, silicon, magnesium, etc. In addition to the alloying elements and cold working, some of the alloys could be further strengthened by heat treatment. Using this combination of techniques, today aluminum alloys having a tensile strength of about 700 MPa, which is close to that of the low carbon steel have been developed. These alloys are used in aerospace, automobile, shipbuilding and other structural members due to their improved mechanical, electrical, physical and corrosion resistance properties (Austral Wright Metals 2014).

1.1 Alloy Classification

Aluminum alloys are mainly classified into two categories, namely

      1. Cast alloys

      2. Wrought alloys

These alloys could be further subdivided into heat treatable and non heat treatable alloys. Almost 80 % of the aluminum alloys are used in the wrought form, such as rolled foils, sheets and plates. Cast alloys are cost effective alloys due to their low melting point but have lower tensile strength compared to the wrought alloys. The

alloys are further designated by 4 digit numeric code in sequential order as shown in Table 1.1. The cast alloys are also numbered correspondingly with a decimal point.

Table 1.1 Cast and wrought alloy classification (Robinson 1990)

Wrought alloys	Designation	Cast alloys	Designation
Aluminum (Commercial pure> 99.9%)	1xxx	Aluminum (Commercial pure)	1xx.x
Copper	2xxx	Copper	2xx.x
Manganese	3xxx	Silicon + Copper/ magnesium	3xx.x
Silicon	4xxx	Silicon	4xx.x
Magnesium	5xxx	Magnesium	5xx.x
Magnesium and Silicon	6xxx	Unused	6xx.x
Zinc	7xxx	Zinc	7xx.x
Others (Lithium)	8xxx	Tin	8xx.x

1.2 Alloy Tempering Designation

Apart from classification based on the alloying elements and processing route, alloys could be heat treated to obtain better mechanical properties and are designated accordingly. Various tempering designations are listed in Table 1.2.

Table 1.2 Tempering conditions (Robinson 1990)

Temper designation	Heat treatment procedure
T3	Solution treated, cold worked and naturally aged
T4	Solution treated and naturally aged
T6	Solution treated and artificially aged
T7	Solution treated and over-aged
T8	Solution treated, cold worked and artificially aged
T73	Solution treated and fully over-aged artificially
T7451	Solution treated, stretched and artificially over-aged
T6I6	Solution treatment, pre-aging and interrupted aging.
HTPP	Solution treated, cooled and maintaining at lower temperature and then aging for long time
RRA	Solution treatment, pre-aging, reversion at higher temperature and again re-aging

1.3 Retrogression and Re-aging Treatment

The 7xxx alloys are mainly used in fabrication of structural members of the aircrafts. These alloys are generally treated in over-aged condition to impart the alloy with better resistance to stress corrosion cracking (SCC) but in turn the alloy incurs loss in its peak strength characteristics. Hence a multistep heat treatment called retrogression and re-aging (RRA) which consists of reversion and re-aging stages in addition to the standard peak-aging treatment is developed. This special type of heat treatment technique is adopted for improving the SCC resistance in high strength aluminum alloys (Bora 1974). By adopting the RRA treatment, the alloy retains high resistance to inter-granular corrosion and SCC without compensating the alloy's peak strength characteristics. After RRA treatment, the microstructure at the grain boundary remains identical to that of the over-aging state. The grain boundary precipitates

which are generally present in a continuous form, becomes disintegrated during RRA treatment which benefits the alloy in acquiring higher resistance to SCC.

The present study aims at optimizing the heat treatment process parameters, such as temperature and duration of the retrogression/reversion process for the aluminum alloy 7010 to secure strength and hardness similar to that of the peak-aged alloy. The microstructure under different aging conditions is investigated using optical microscopy, scanning electron microscopy and transmission electron microscopy (TEM). The fatigue crack growth (FCG) performance of this alloy is studied under constant amplitude fatigue loading condition at various stress ratio and also, under aircraft service simulating loads. This study is very much important before employing the RRA treated alloys for aircraft structures. Therefore the influence of heat treatment on fracture toughness and fatigue crack growth behavior is also studied and presented in this thesis in different chapters. In addition, the electrochemical corrosion and exfoliation corrosion behavior of alloy in RRA condition is compared with peak-aged and over-aged condition. The application of this heat treatment to 7010 alloy is expected to benefit the aircraft industries in designing the structural components, such as lug joints and fuselage components. These components which are feasible to remove and heat treated can be considered for improving the SCC resistance by subjecting them to RRA condition which can benefit in extending the life.

A detailed study on the literature review is reported in the second chapter, along with the objectives and methodologies adopted are described. The details about the alloy material, experimental procedure, and testing methodologies adopted for various tests are presented in the third chapter. The details of microstructural and mechanical characterization of the alloy under different aged conditions are presented in chapter four. The FCG behavior of the alloy is presented in chapter five. The corrosion and exfoliation corrosion behavior of the alloy is presented in chapter six. Finally, the outcome of the present study is discussed in chapter seven. The inference from the present study and scope for the future work is presented in chapter eight.

1.4 Scope of the Study

The study aims at optimizing the retrogression/reversion treatment parameters in modifying the microstructure at the grain boundary and at the grain interior. The influence of altered microstructure on the mechanical properties is investigated in detail. The effect of microstructure on the FCG behavior especially in the near-threshold regime of FCG at various stress ratios is focused. Further the influence of RRA treatment on the spectrum FCG behavior under fighter aircraft loading standard for fatigue evaluation (FALSTAFF) is investigated. The study reveals that the RRA does affect the alloy in terms of improving the life in FCG stage in addition to the earlier reported improvement in SCC resistance.

Page left intentionally blank

CHAPTER 2

LITERATURE REVIEW

2.1 Precipitation Strengthening (age hardening) in Aluminum Alloys

Alfred Wilm's accidental discovery during the 20th century has lead to the development of the age hardening process. He found that the hardness of an alloy after the solution treatment and quenching was relatively low, which subsequently increased upon time (aging). This method of aging was applicable for the alloys which exhibit decreasing solute solubility with decrease in temperature. Upon rapid cooling of alloy from solutionized condition will suppress the formation of new phases and exist as a supersaturated solid solution. When this quenched alloy was aged at an appropriate temperature and held for sufficient time duration, sub-microscopic precipitates of second phases were evolved, which increases the strength of the alloy. The mechanism involved was later understood with the use of sophisticated analytical tools such as X-ray diffraction and electron microscopes by Guinier and Preston (Mukhopadhyay 1994).

The sequence of precipitation is as follows:

Super-saturated solid solution ⟶ **Coherent precipitates** ⟶ **Semi-coherent precipitates** ⟶ **Stable incoherent precipitates**

The interaction of moving dislocations with the precipitates, size of the precipitates, and shape of the precipitate particles, their nature, the interface between the precipitates and the matrix determine the mechanical properties of the heat treated alloys. Most of the commercial wrought aluminum alloys that belong to 2xxx, 6xxx and 7xxx series are age hardenable alloys. These alloys gain the strength by formation of the nanoscale precipitates, which generally starts by formation of GP zones. These precipitates exhibit lower interfacial energy with the matrix and are fully coherent precipitates. For these precipitates, the energy barrier for the formation is less.

Subsequent aging transforms the GP zones to more stable precipitates. The stable and equilibrium precipitates have different crystal structures compared with the aluminum matrix. Age hardening was well studied in Al-Cu systems (Andersen et al. 2018; Ringer and Hono 2000).

2.2 Age Hardening in Al-Cu System

The precipitation sequence in aluminum alloys depends on the degree of super-saturation and the subsequent aging temperature. The precipitation sequence observed in Al–Cu systems is as follows (Ringer and Hono 2000) :

Super-saturated solid solution $\longrightarrow$ GP zones $\longrightarrow$ θ'' $\longrightarrow$ θ' $\longrightarrow$ θ (Al$_2$Cu)
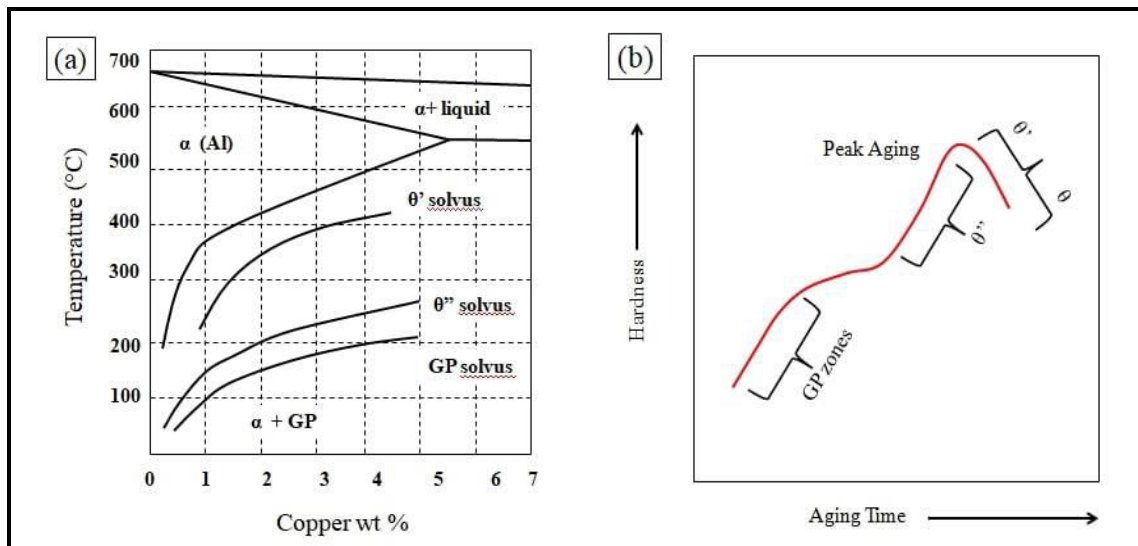
Fig. 2.1 a) Al-Cu phase diagram highlighting the metastable solvus lines b) Variation of hardness as the precipitate transform during aging (redrawn from Ringer and Hono 2000)

The Al–Cu phase diagram with the metastable solvus lines is shown in Fig 2.1. The complete precipitation sequence can only occur when the alloy is aged at temperatures below the GP zone solvus line. Different stages in the sequence of precipitation can be hindered by aging at suitably high temperatures. Aging at lower temperature leads to metastable precipitates, such as θ'' (coherent) and θ' (semi-coherent). Upon prolonged aging at the same temperature, these metastable precipitates transform into incoherent state. The precipitates formed during heat treatment hinder the motion of

dislocations due to the associated strain field around them generally due to change in crystal structure between the matrix and the precipitates, as shown in Fig 2.2.
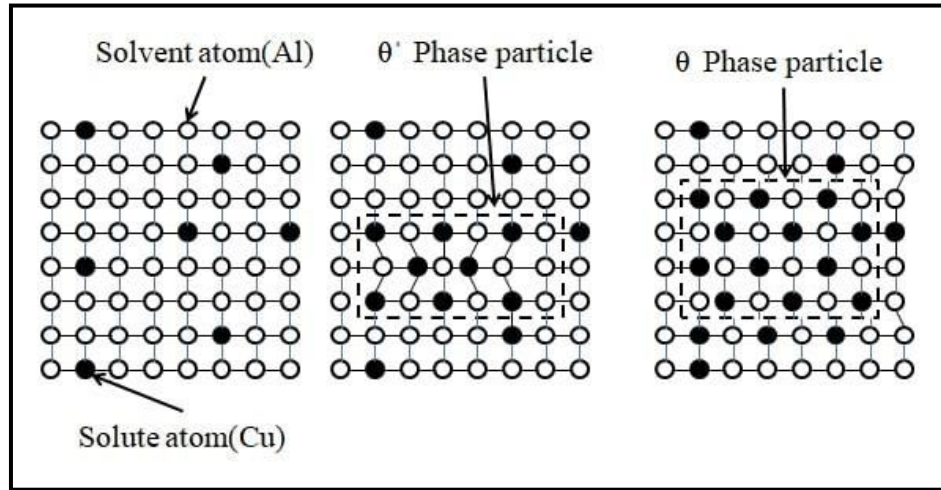
Fig. 2.2 Coherent and incoherent precipitates creating lattice strain in the matrix (Williamson and Smallman 1956)

Generally, when the precipitate size was small, they were coherent with the matrix and were deformable as the dislocation cut through them. While the precipitates become coarsened, they were incoherent and become non deformable. The dislocations bypass them, as shown in Fig. 2.3.
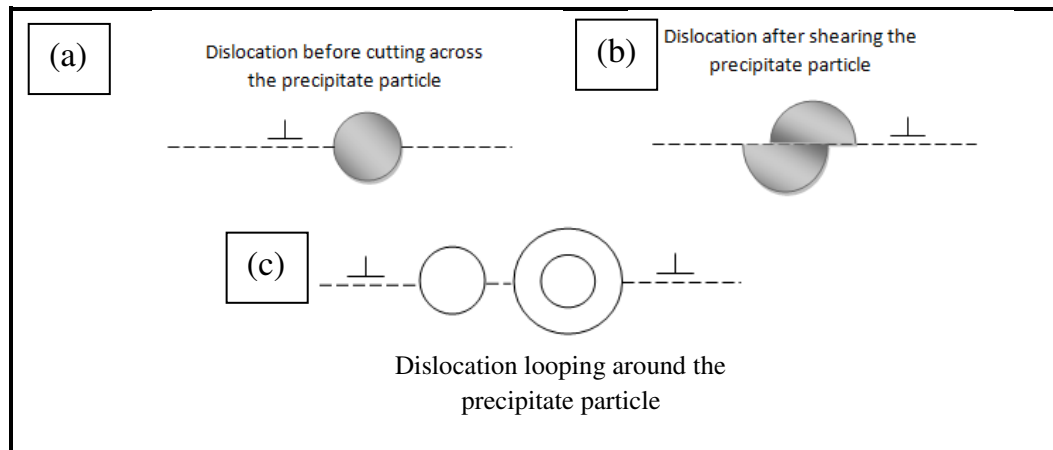
Fig. 2.3 Mechanism of dislocation motion across the precipitates; a, b) Dislocation shearing through the precipitates c) Dislocation looping around the precipitates (Chen et al. 2013b)

2.3 Precipitation Hardening in Al-Zn-Mg Systems

Aluminum alloys (7xxx) have been widely used in aerospace structural applications due to their high specific strength and good damage tolerant properties. Aluminum exhibits a FCC crystal structure as shown in Fig. 2.4 (a). The precipitate $MgZn_2$ exhibit a close packed hexagonal crystal structure as shown in Fig. 2.4 (b). These alloys exhibit a good response to age hardening characteristics and thereby impart better mechanical properties. The Al-Zn phase diagram is shown in Fig. 2.5 and isothermal section of Al-Zn-Mg system is presented in Fig. 2.6. The precipitation process in Al-Zn-Mg system is as follows:

SSSS $\longrightarrow$ GP zones (coherent) $\longrightarrow$ η' ($MgZn_2$ semi-coherent) $\longrightarrow$ η ($MgZn_2$, incoherent)
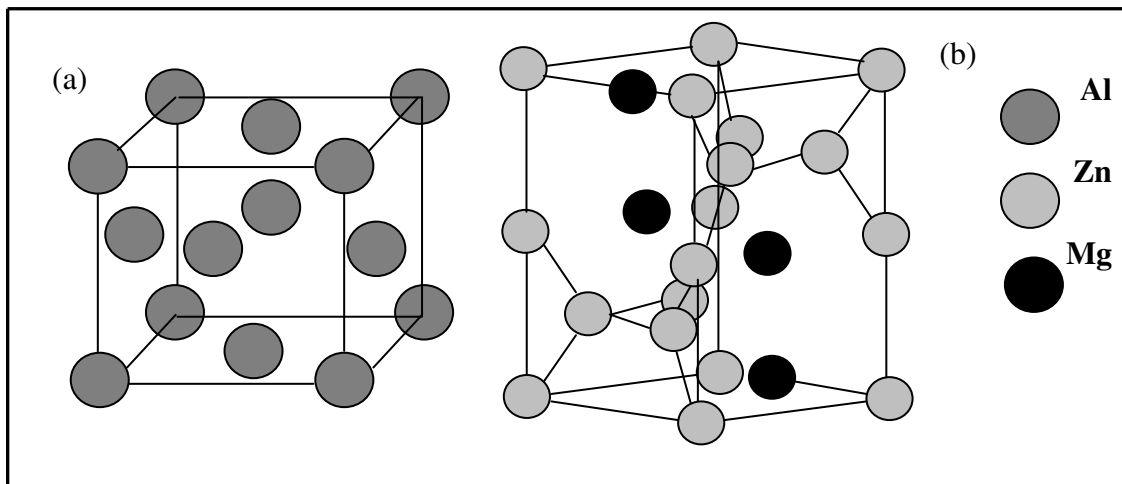
Fig. 2.4 a) Aluminum FCC crystal structure, b) $MgZn_2$ hexagonal close packed structure (redrawn from (Wu et al. 2010))
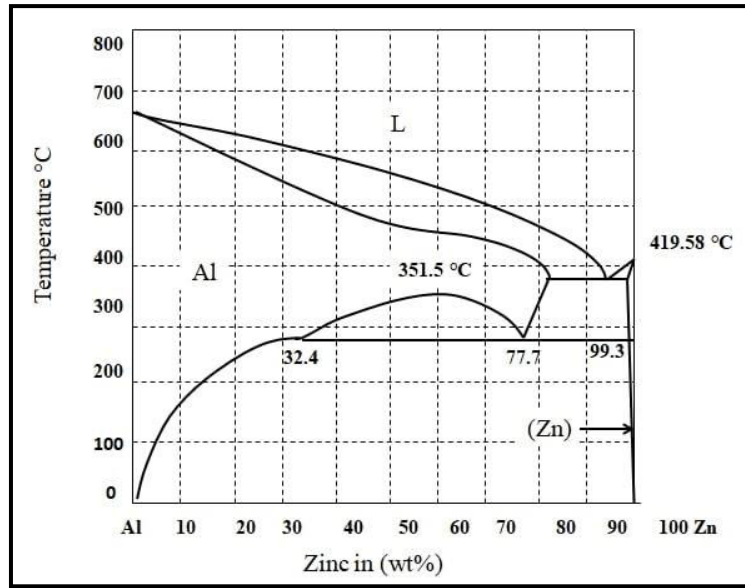
Fig. 2.5 Al-Zn phase diagram (ASM Handbook Vol 3 2004)
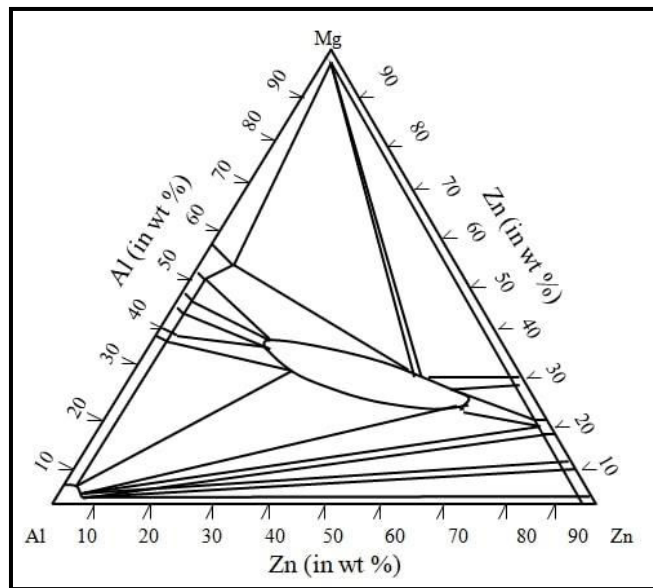
Fig. 2.6 Al-Zn-Mg isothermal section at 20°C (ASM Handbook Vol 3 2004)
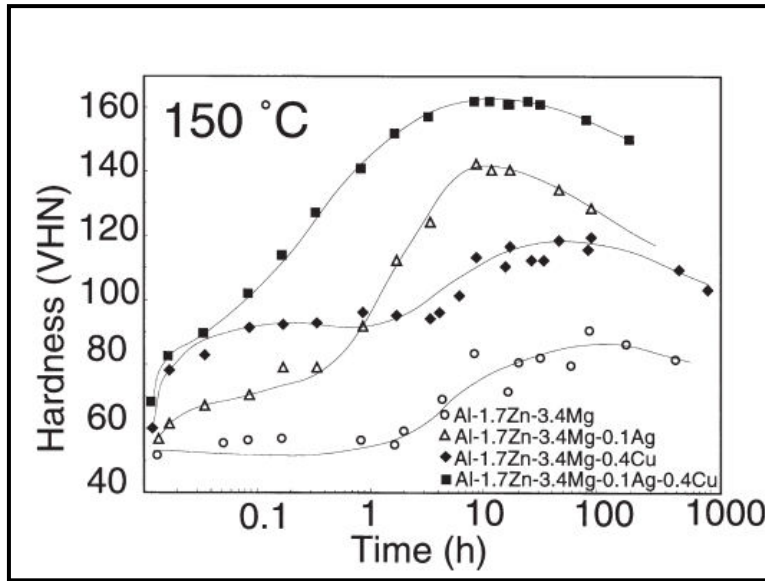
Fig. 2.7 Plot of hardness variation with the aging time at different aging temperatures (Ringer and Hono 2000)

The change in hardness profile with solute content and aging parameters is shown in Fig. 2.7. The GP (Guinier-Preston) zones are the cluster of atoms (500 atoms in one dimension) precede the formation of η' (semi-coherent) precipitates. The η' precipitates further transform into stable form, η (MgZn$_2$) instead of dissolution and re-precipitation. Controversies existed regarding the size, structure, chemistry, and morphology of the GP zones until the studies carried by Mukhopadhyay (1994), indicated that the GP zones in Al-Zn-Mg systems were spherical in shape. The GP zones were composed of Mg and Zn in equal proportions. The η' precipitates exhibited a hexagonal close packed structure with MgZn$_2$ stoichiometry which further transform into stable η form upon prolonged aging.

2.4 Retrogression and Re-Aging (RRA)

The conventional aging treatment, such as T6, which is a peak-aging condition attains highest strength but results with lower SCC resistance (Bobby Kannan et al. 2003). Unlike T6 over-aging provides better SCC resistance but leads to drop in 10-15 % of the peak strength (Rout et al. 2015a). A multistep aging treatment such as retrogression/reversion and re-aging (RRA) benefits in overcoming the drawbacks of both over-aging (T7) and T6 treatments. In a conventional over-aging treatment the

alloy gains higher SCC resistance but incurs with 25-30 % loss in peak strength of the alloy (Marlaud et al. 2010a).

In the RRA heat treatment, which is a double stage heat treatment carried on the T6 treated alloy. Firstly, the T6 alloy is subjected to an intermediate high temperature, i.e., temperature between solutionizing temperature and peak-aging temperature, called retrogression or reversion stage (Bora 1974). The alloy after reversion treatment again when subjected with T6 treatment called re-aging step of RRA treatment. The time duration of the high temperature reversion stage play an important role, that partially solutionizes the already T6 treated alloy microstructure. The strength gained after this stage of reversion was the minimum (Viana et al. 1999). During the second stage of heat treatment the solutes re-precipitate to acquire the lost mechanical strength. Cina (Bora 1974) proposed that the optimum RRA treatment was obtained by performing the retrogression to the minimum strength and re-aging to T6 condition. This results with higher strength properties (Fig. 2.8) in comparison to T6 treatment and higher level of SCC resistance compared to the T7451 condition.
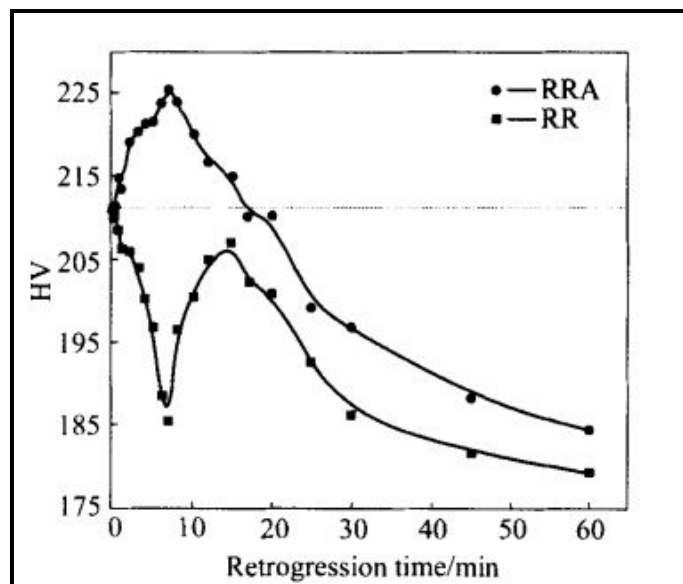
Fig. 2.8 Variation of hardness profile with RRA treatment (Ning et al. 2006)

Cina's heat treatment process involved retrogression at temperature range 220-280 °C for a short period of 1 to 30 sec, which was not suitable for aircraft components that are generally made of thicker sections. Later they adopted induction furnace heating for thicker sections which resulted in non uniform heating across the thickness due to

a short time of retrogression. The work was further extended by Wallace and team (Danh et al. 1983) to apply to thick plates by reducing the temperature of retrogression. They used a silicon oil bath for heat treatment. The work was later carried by conducting retrogression for varied temperatures from 160 °C to 220 °C. They claimed that reaching the minimum hardness point in retrogression curve was not necessary to get peak hardness after re-aging step. Retrogression time corresponding to the secondary peak in the retrogression stage/curve had gained higher SCC resistance retaining the T6 strength of the alloy.

There have been numerous studies related to the understanding of microstructural changes that benefitted the SCC resistance of these alloys. Many researchers have found that the grain boundary microstructural characteristics were the influencing factor in controlling the SCC. The first microstructural studies carried out by using TEM on the RRA alloy by Danh (1983) stated that, during the first stage of retrogression, GP zones were dissolved, which was followed by recovery of strength during the second stage. This was due to the re-precipitation of strengthening precipitates η'. The high density of the intermediate precipitates (metastable) that were homogeneously present in the matrix was responsible for the peak strength in T6 alloy. However, existence of η precipitates in grain interior were the cause for strength of over-aged alloy (T7). In over-aged condition the density of precipitates was reduced, and therefore the strength in T7 treated alloy was reduced compared to the T6 treated alloy. They also observed that the growth of GBP's during retrogression, which was suggested to have contributed to the resistance towards the SCC. RRA microstructure on the grain boundaries being similar to T7 temper, it was having higher SCC resistance than the T6 alloy. The hydrogen trapped at the crack tip was suggested to diffuse towards the grain boundary, where it gets condensed. This was understood to have influenced in improving the SCC resistance.

From the past studies, it was understood that during reversion treatment of the peak-aged or under-aged alloy, initially a minimum on the hardness plot was observed. This was followed by an increase in the hardness for continued reversion treatment. The initial minimum was due to the GP zones and η' precipitates which got dissolved while high temper reversion was carried. When this was continued for longer time,

the undissolved η' precipitates gets transformed into equilibrium η, achieving a local maximum on the hardness plot (Danh et al. 1983; Kanno and Araki 1994; Viana et al. 1999).

The re-aging step of RRA was understood with several other mechanisms, few researchers have stated that the growth of the partially dissolved η' precipitates during reversion stage was responsible for the regained strength (Park and Ardell 1984). It was proposed that the nucleation of new precipitates and also the transformation to stable precipitate form also contributed to the strength during the re-aging stage (Viana et al. 1999).

The study carried by Park and Adrell (Park and Ardell 1984), demonstrated a conflict with the earlier findings. The precipitation phenomenon in the T6 condition predominantly consisted of GP zones, whereas the RRA treated condition exhibited predominantly η' precipitates which were responsible for the peak strength (Adler et al. 1972). Further RRA heat treatment was carried out on the actual aircraft components made up of 7075-T6511 (Holt et al. 1999), with a component thickness of 0.75 inch, cut from the structural component removed from service due to corrosion. The component was subjected to RRA treatment, which resulted in strength matching the standard value, with significant improvement in the corrosion resistance.

The RRA behavior of 7010 extruded component was studied with the focus of short transfer ductility and SCC resistance by measuring electrical conductivity (Angappan et al. 2011). RRA heat treatment did not affect the ductility of alloy up to 30 min of retrogression without loss in peak strength. But after 30 min, a 6 % rise was observed in strength which again dropped after 50 min. The increase in SCC resistance indirectly measured by electrical conductivity was co-related to the enrichment of Cu on GBP's by diffusion from the PFZ surrounding it.

Studies carried by Talianker (1989) highlighted the change in the density of dislocation activity near the grain boundaries contributed to the improved corrosion resistance. Although it was stated that the diffusion of solute atoms, such as Zn and Cu contributed to the corrosion resistance, no concluding evidence was drawn.

A quantitative study was performed by using SAXS and APT by Marlaud (2010b) on different 7xxx series alloys that were heat treated to different aging conditions. It was understood that at a temperature up to 120 °C resulted in the precipitates composing of Cu in the range of 0-2 at %. By ramping up the temperature to 160 °C the Cu content was increased to 5-10 at %. At high temperature range say above 150 °C, the diffusivity of Zn, Mg and Cu atoms in Al lattice being approximately 4, 3 and 0.1 (unit in 10^{-20} m^2 $S^{-1)}$ respectively (Marlaud et al. 2010b). The lower diffusivity of Cu in Al was the direct evidence showing the shift in Cu content of precipitates from 1 to 15 at %, towards the equilibrium value as the heating was progressed.

A repetitious RRA treatment (2 to 4 times) was adopted (Peng et al. 2011), which resulted in the coarsening of matrix precipitates to size of about 4-25 nm compared to 10-40 nm in the T76 treated sample. At the same time grain boundary precipitates have grown to 85-96 nm in size. The ultimate tensile strength was retained up to 3 times of RRA which suddenly dropped after the 4th time of repetition. The electrical conductivity of 3 times the RRA sample was higher than the regular RRA sample. The Cu content of GBP's was much higher than the T76 sample. The Zn content of GBP's had decreased after repetitious RRA.

The evolution of precipitate microstructure during RRA was studied by Maralaud (2010b). It showed that difference in solute distribution within the grains of RRA and T6 treated samples. It was concluded from APT (atom probe tomography) that more number of solute clusters were present in between the precipitates in matrix compared to the T6 treated condition. The author had also observed the change in the composition of the precipitates by in-situ SAXS (Small Angle X-ray Scattering). Initially, the Cu content of precipitates observed to be 2 at %. The Cu content was increased to 5 at % with the retrogression at 185 °C after 20 min. They also observed a decrease in the Zn content of the precipitates with the retrogression time. The diffusion and substitution of Zn with Cu in the GBP's and matrix near the precipitates getting enriched with Zn was evident.

A study carried by performing retrogression at different heating rates (Li et al. 2010) such as low, medium and high rate indicated that reversion carried at a medium

heating rate (57 °C/min) was beneficial from the strength point of view. When the heating rate was low (4.3 °C/min) the alloy had sufficient time to reach the reversion temperature and therefore the strengthening precipitates in the grain interior undergone transformation into stable phases. These precipitates upon re-aging grow further making the matrix lower in supersaturation to have newer precipitates. In contrast at a high heating rate (340 °/min), the alloy was not provided with sufficient time for strengthening precipitates to grow. Instead, those present which were smaller than the critical size got dissolve completely and the stable precipitates got coarsened and formed incoherent precipitates leading to a reduction in the strength. It was concluded that the medium heating rate during reversion treatment was beneficial in obtaining the alloy with the highest strength as schematically depicted in Fig. 2.9.
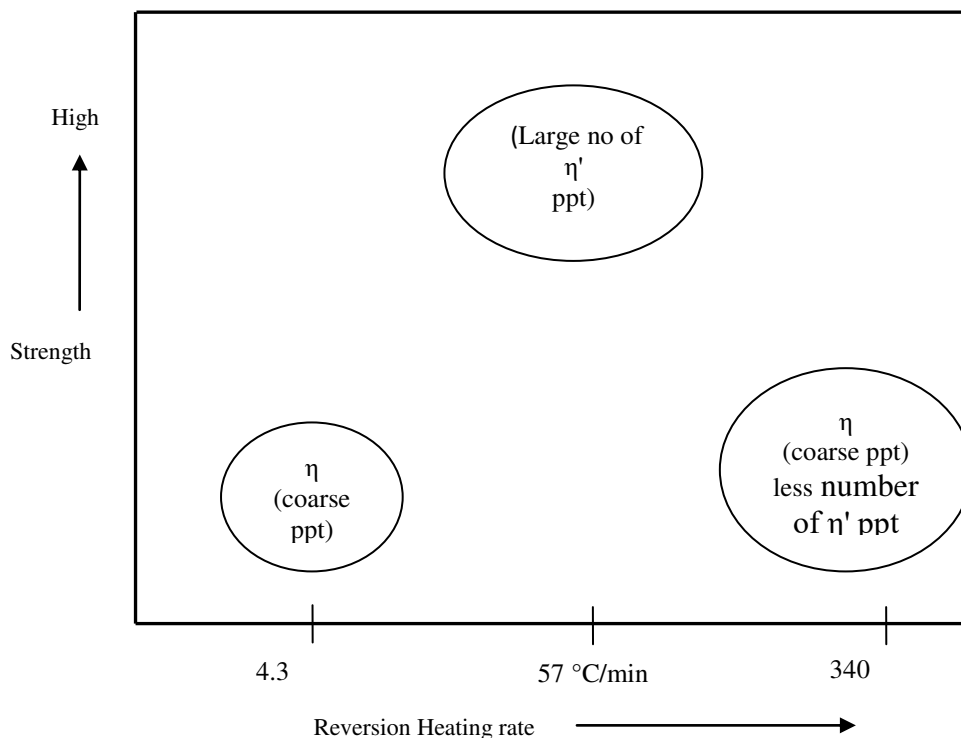
Fig. 2.9 Variation in strength properties with reversion heating rate

Although the heat treatment was invented to modify the microstructure at grain boundaries that benefitted SCC resistance, the literature study also suggests additional benefit of RRA in obtaining better strength and higher fatigue crack growth resistance. Therefore it is important to study its behavior under various stress ratio levels and under the service simulating loading conditions which is rarely studied.

2.5 Fatigue Failure

Fatigue being one of the dominant modes of failure that occurs in structures subjected to cyclic loading though the applied load below the yield strength of the material. The dislocation activity within the material forms persistent slip bands on the surface leading to localized plastic deformation. These are the regions on the surface leading to the formation of micro cracks that further propagate to ultimate failure of the component. The stages involved in a fatigue failure are presented in Fig. 2.10.

```
┌────────┐   ┌────────┐   ┌────────┐   ┌────────┐   ┌────────┐
│ Cyclic │→  │ Crack  │→  │ Micro  │→  │ Macro  │→  │ Final  │
│  slip  │   │nucleatio│   │ crack  │   │ crack  │   │fractur │
│        │   │   n    │   │ growth │   │ growth │   │   e    │
└────────┘   └────────┘   └────────┘   └────────┘   └────────┘

   ←─────────────────────────→          ←────────────────────→
  Fatigue crack initiation stage          Crack growth stage
```
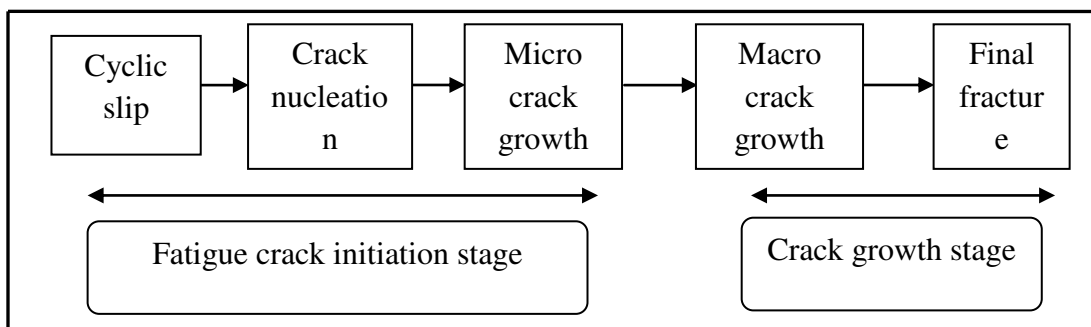
Fig. 2.10 Different stages during fatigue failure of a component

2.5.1 Crack initiation

The crack generally nucleates due to cyclic slip of dislocations leading to the slip band formation. This can occur even if the stress level being lower than the yield strength of the material. It is due to localized plastic deformation as a result of moving dislocations within the grains. Predominantly nucleation occurs at the surface, since the material exists only on one side, due to which surface grains are less constrained for a cyclic slip. Slip steps get created at the surface of the component and the new surface is exposed to the environment that further gets covered with the oxide layers. Hence, the cyclic slip is not completely reversible, i.e., one due to the oxide layer and the other due to strain hardening at the slip bands. Hence, there forms intrusions and extrusions (Fig. 2.11) at the surface that leads to crack nucleation (Schijve 2001). There are other promoting aspects, such as surface roughness resulting from corrosion pits and fretting fatigue.
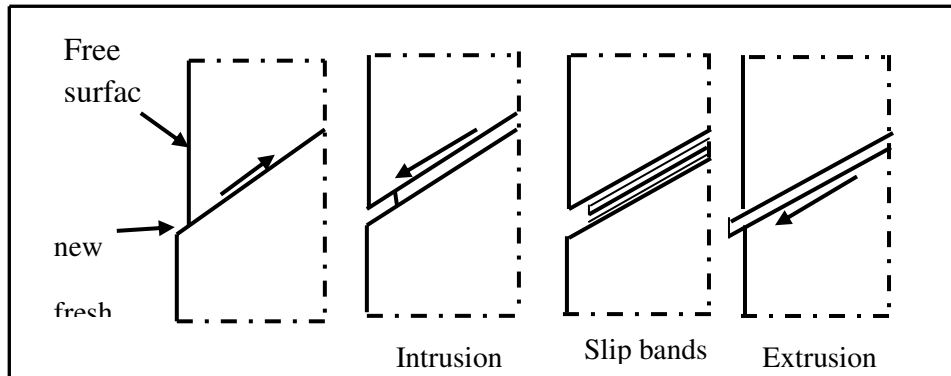
Fig. 2.11 Slip bands leading to formation of extrusions and intrusions and nucleation of crack (Schijve 2001)

2.5.2 Crack growth

The crack propagation is a bulk material phenomenon. The micro crack acts as a site for inhomogeneous stress distribution on a micro level with a high stress concentration at the crack tip. The cracks originated from the surfaces (extrusions and intrusions) will grow into neighboring grain and orient towards the preferred slip direction. In general, the crack will grow perpendicular to the direction of the load. The micro crack growth depends on the cyclic plasticity and the barrier to slip. It implies a threshold value of fatigue load for crack growth to take place. As the crack approaches grain boundary the crack growth rate decreases and growth rate further increases when the crack grows through the grain (Schijve 2001).

2.5.3 Crack nucleation at inclusions

The presence of inclusions at the material surface or at beneath the surface may lead to crack nucleation. Similarly, in aluminum alloys, they can originate at intermetallic inclusions. Inclusions do not affect the strength of the material but alter the ductility of the material due to the formation of voids during high plastic strain. In spite of having smaller plastic strain during high cycle fatigue, inclusions are considered to be foreign particles that may play a role in initiating cracks in high strength materials.

2.5.4 Crack growth barrier

All the cracks that nucleated will not grow under fatigue cycling. There exists a threshold value of cyclic load for crack growth to take place. At the sharp notch, there

can be many cracks originated but only those cracks which meet the criteria will start propagating. The restriction for propagation may be due to grain boundary obstacles or any type of hard particles at the crack tip that restrains the cyclic slip. Hence the fatigue limit is the largest cyclic stress amplitude which does not lead to continuous crack growth leading to failure. The fatigue limit is termed as the threshold for growth of crack and not for the nucleation of a crack. There also exists evidence for the growth of crack by looping the inclusions (Fig. 2.12).
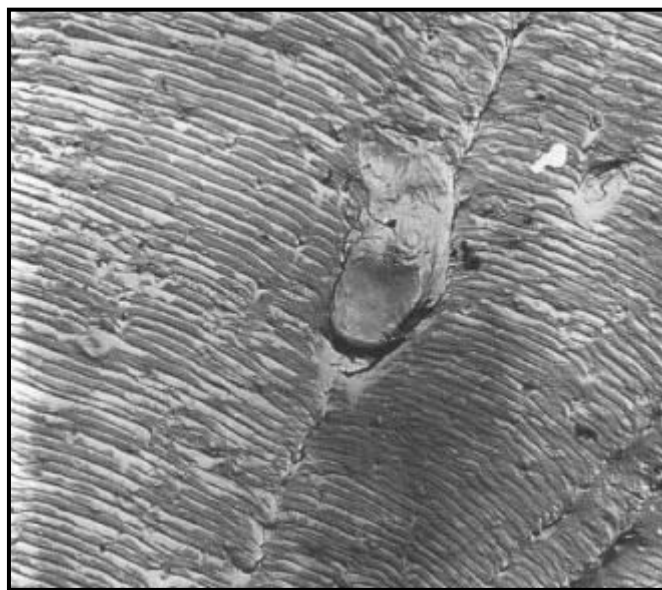
Fig. 2.12 Fatigue crack growth around the inclusion (Schijve 2004)

2.5.5 Fatigue striation formation

Once the fatigue crack is initiated, it is no more a surface phenomenon but a bulk material phenomenon. Though a number of cracks get formed, only the dominant one which is perpendicular to the maximum principal stress direction will propagate further. Slip deformation will occur at more than one slip planes. During cyclic loading, crack gets opened by plastic deformation which occurs at more than one slip system that appears on the maximum shear stress planes. Loading makes the crack extension by slip deformation caused by the flow of dislocations to the crack tip as shown schematically in Fig. 2.13. The deformation is not reversible, hence it induces marks on the crack surfaces that are called striations (Fig. 2.14), each striation spacing being equal to crack extension for each loading cycle.
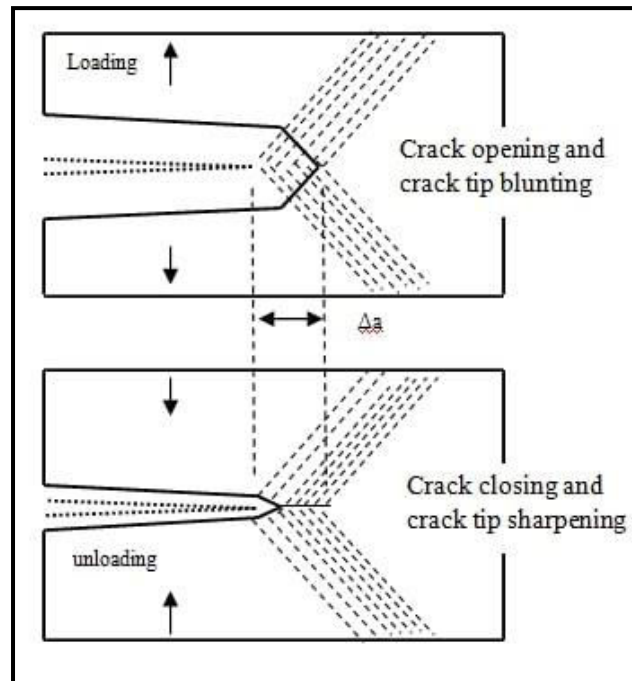
Fig. 2.13 Crack extension during single cyclic load (Schijve 2004)
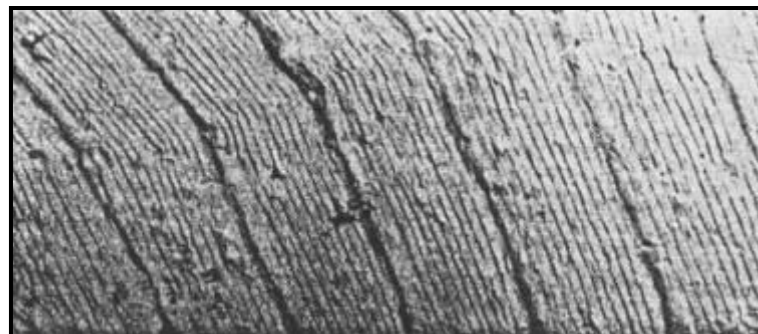
Fig. 2.14 Formation of striations during fatigue loading (Schijve 2004)

2.6 Fatigue Design Philosophy

Over the decades the structural design of aircraft evolved from safe life design to fail safe design to damage tolerant design. The safe life and fail safe design concepts make use of standard S-N data to estimate and predict life. However damage tolerance design concepts make use of associated failure modes, crack configuration, environmental and corrosion effects into consideration. In the safe life approach, the structure was considered to be failed when the crack gets nucleated. The components are not used further and were directly thrown out of service. The methodology proposes that by knowing the load and fatigue properties of the material, a component could be designed for a specific period of life by controlling the stress levels.

Mechanical component design was carried with the aim of serving for a particular period of time after which performance could not be guaranteed. This type of design was uneconomical and caused disasters which lead to the collapse of the concept but it is still used in the design of landing gears and other components (Daniel et al. 2014).

The fail safe design approach in contrast, considers a multiple load paths, even if one component fails, the overall structure remains intact and hence redundancy is provided to overall structure. The structural member would not fail without giving opportunity for damage detection. The design concept considers the presence of crack as starting point to estimate the remaining life. It mainly aims at redundant structures but does not always guaranty safe structures when it has multiple site damages. The continued use of aging aircraft is associated with an uncertainty concerning the location of crack initiation which leads a concern for the airworthiness of aircraft.

These concerns related to airworthiness have been overcome by the new concept of fatigue crack growth approach. It assumes initial structural damage and makes it mandatory to perform periodic inspection. In this approach, residual strength would be determined by fracture mechanics concepts. This concept was evolved by use of test by non destructive methods, such as visual inspections, radiography and eddy current methods to detect the micro cracks and internal voids. This method uses in-service data for new aircraft design (Daniel et al. 2014).

The continued research in the field of aircraft design over the last many years has lead to the understanding that the fatigue is a microstructural phenomenon consisting of crack nucleation as an invisible micro cracks at slip bands. It is understood that micro cracks can generally occur immediately, if the cyclic stress is above the fatigue limit. Once the crack is nucleated it is the inherent material microstructure that controls the nature of the crack growth in a structure. It can be slow or progressive growth depending on the grain boundaries, precipitates and other microstructural features with which crack interacts during loading.

2.7 Fatigue Crack Growth

In damage tolerance design criteria one has to regularly monitor the crack extension by various non destructive techniques. One would estimate the residual life of the Component by using design data and fatigue crack growth curves that are experimentally determined using fracture mechanics concepts for the particular material. The typical fatigue crack growth curve is shown in Fig. 2.15. A decreasing ΔK test has to be conducted by load shedding method until the crack growth rate of 1 x 10^{-6} mm/cycle is reached which is considered to be in the near-threshold regime (Chen and Chaturvedi 2000). Tested sample would then be subjected to increasing ΔK tests until final fracture of the sample.
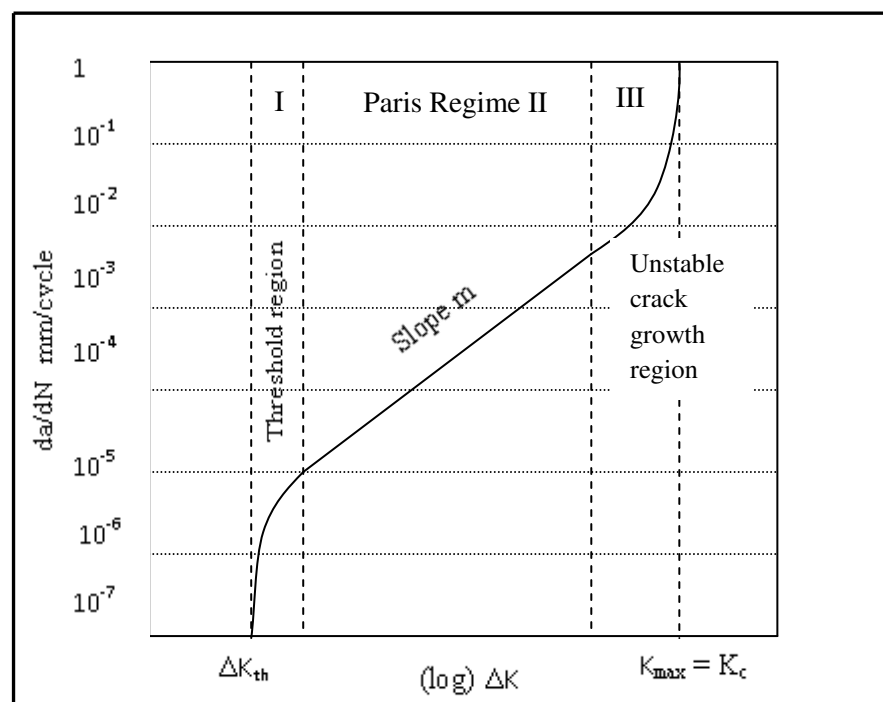
Fig. 2.15 Different regimes observed in the fatigue crack growth rate (da/dN vs ΔK) curve

The fatigue crack growth curve consists of three regimes, namely the crack threshold regime, the Paris' regime followed by final failure when ΔK reaches the critical value which is the fracture toughness of the material. Fatigue threshold regime plays an important role which depends on microstructure for several materials. Mean stress or stress ratio effect is also an important factor that influences the FCGR. In general

23

increase in mean stress, maintaining the amplitude stress has a negative effect and lowers fatigue life of the component. This is also termed as stress ratio effect on the FCGR curve. At same level of ΔK, increase in stress ratio R increases the crack growth rate.

Various factors that influence the FCGR were studied in the literature and noted that the crack closure due to various mechanisms, influence in reducing the crack growth rate. In this case the actual load experienced by the crack tip is different and much lower than the actual ΔK as per typical FCGR curve. Hence ΔK_{eff} (Fig. 2.16) is appropriate to consider as a similitude factor while deriving the FCGR curve.
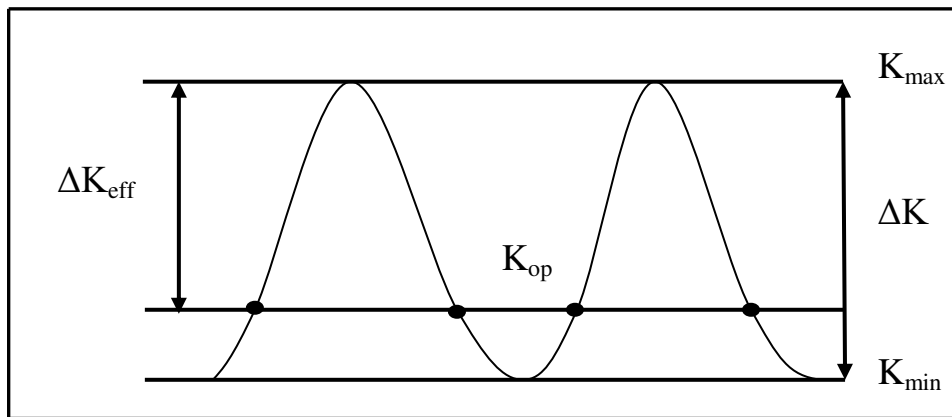
Fig. 2.16 Cyclic stress intensity level represented with ΔK_{eff} consideration as a similitude factor

Gysler and Lindigkeit (1981) studied the effect of microstructure on the fatigue crack growth of Al-Zn-Mg-Cu alloy in under-aging and over-aging conditions. The alloy aged below 100 °C showed no semi-coherent ή precipitates. Aging for 160 °C for 70 hours showed the formation of stable η precipitates at the grain boundary along with the formation of PFZ's. This over-aging condition resulted in the formation of hexagonal disc shaped ή precipitates of 20 nm in size in the matrix. The nature of the crack propagation rate, da/dN vs ΔK below ΔK value of 10 MPa√m, indicates microstructure change affecting the crack growth rate. The over-aged material had lower resistance and under-aged material showed higher resistance to the crack propagation. For the alloy consisting of shearable precipitates, which are formed by aging at 100 °C for various time intervals, no difference in crack propagation rate in the intermediate ΔK region (Paris' region) was observed. But there exists some

difference in the crack growth rate at the region of the threshold stress intensity range. On the contrary, over-aged condition exhibits lower crack propagation resistance.

Microstructural influence on the tensile deformation was studied by Srivatsan et al. (1997) during the study on fracture behavior of 7075 alloys. They stated that the hexagonal disc shaped ή precipitates which were coherent with the matrix being responsible for primary strengthening in age hardenable alloys. The grain boundaries were accommodated with equilibrium η precipitates and narrow precipitate free zones (PFZ). The T77 treated alloy had shown strength to be almost the same in both longitudinal and transverse directions. The macroscopic fracture was observed to be by shear and microscopic fracture was observed to be exhibited by both brittle and local ductile in nature which was co-related to cracking at the grain boundaries and micro void formation and coalescence, respectively.

The slip and fracture of age hardenable aluminum alloys mainly depends on the microstructure and deformation characteristics of the strengthening precipitates. The strengthening precipitates are either sheared or bypassed by dislocations. The shearable precipitates promote planar dislocation distribution. During cyclic loading, certain dislocations can move back to the original position on the same slip plane while unloaded, thereby hinder the crack growth. Whereas, with the non shearable precipitates the dislocations will loop around and will not roll back on the same slip plane and will unite with other dislocations and promote higher crack growth rate. On the other hand, the precipitates at the grain boundary and PFZ's also had an influence on the crack growth. The resistance offered by the PFZ's against the deformation was less compared to the bulk grain. Hence, the formation of voids on the grain boundary particles was easy and it promoted crack growth.

Desmukh et al. (2006) studied the crack propagation behavior on commercial 7010 alloy, subjected to different aging conditions, such as near peak-aged, peak-aged and over-aged. The studies showed that the crack propagation rate was least for the near peak-aged sample and maximum for over-aged sample. However, the over-aged sample possessed a higher fatigue crack propagation threshold (ΔK_{th}) and a higher value of the fatigue strength. It is concluded that the nature of the precipitates present

in the matrix, on the grain boundary and the PFZ adjacent to the grain boundary decides the fatigue behavior of an alloy. The over-aged alloy that deforms homogeneously owing to the presence of non shearable precipitates and coarse precipitates on the grain boundary with PFZ near the grain boundary, exhibited higher fatigue crack growth rate. Instead, the alloy with near peak and peak-aged conditions had shearable precipitates and less coarse GBP's with reduced PFZ width which exhibited lower fatigue crack growth rate. The over-aged alloy exhibited homogeneous material deformation as a result, no strain localization and hence fatigue crack growth rate was higher.

Recently work carried by Xia (2016) demonstrated an ultra low fatigue crack growth rate in high strength aluminum alloys after modifying the RRA treatment. The modified RRA involved lower retrogression temperature and longer retrogression time. This influenced in increasing the matrix precipitate size and modifying the PFZ width. This promoted a transgranular crack path than having mixed modes consisting of transgranular and intergranular fatigue crack growth.

The RRA study carried by Wang (2014) on 7050 alloys exhibited lower crack growth in Paris' regime compared to that of the T7451 condition. The wider PFZ and coarsened GBP's were responsible for faster crack growth rate in the high ΔK regime of fatigue crack growth. The void formation at the interface between GBP's and wider PFZ in T7451 condition promoted intergranular crack path in the high ΔK regime, whereas RRA exhibited preferentially transgranular nature of crack growth which benefitted in reducing crack propagation speed.

2.8 Aircraft Spectrum Loading

Although the standard experimental design data was generally used while designing the components, one has to test the alloy material for real time loading before it could be applied into real structures. The aircraft loading consists of various levels of loads, such as taxiing, take off, loads acted during high altitude cruising, gust loads, turbulence and finally the descent, and touchdown. Hence, it is extremely important to know the behavior of crack growth under standard service simulating loads. A mini-FALSTAFF load sequence is a short version of standard FALSTAFF load spectrum,

which is a standardized variable amplitude test load sequence developed for fatigue analysis of material used for fighter aircraft. One block of this load sequence consists of 18012 reversals at 32 different stress levels and presents loading equivalent to 200 flight hours.

The effect of mean stress on the fatigue crack growth is considered by invoking various closure mechanisms exhibit during variable amplitude loading which contribute to enhance the crack propagation life. A high-low and low-high sequence of loads influence the crack growth behavior differently. Elber (1970) had shown that in a fatigue cycle with zero to tensile loading, the crack gets closed before the zero load was reached. This was mainly due to the residual compressive stresses developed on the crack surface that make the surfaces contact each other before the minimum load in the fatigue cycle was reached. Hence retardation in fatigue crack growth was exhibited while the reduction in cyclic load was experienced by the crack tip. Research by Carvalho and Martins (2018) had shown the effect of single overload in fatigue cycle on the crack growth in aluminum alloy under different aging conditions.

The inability to accurately predict the fatigue crack growth under variable amplitude loading in aircraft is one of the major problems faced by the industry. The attempts to determine the crack growth rate using constant amplitude load data do not consider load interaction effects and leads to error of significant magnitude. Studies were carried to find out the effect of R ratio and material dependency on FCGR (Borrego et al. 2010) indicated that the crack closure in AlMgSi-T6 containing Cr and Mn, was dominated by roughness induced closure mechanism. The alloys without Cr and Mn were dominated by plasticity induced crack closure mechanism. The dispersoid particles which were rich in Cr/Mn promote planar slip and crack deflection resulting in tortuous crack path enhancing roughness induced crack closure. This retarded the crack growth rate. Fatigue crack growth studies carried on RRA treated 7010 sample carried at constant amplitude tests (Lin et al. 2014) has shown that the fatigue strength of RRA treated sample was between that of the T6 and the T7451 condition.

The effect of the corrosion environment on the fracture behavior of 7475-T7351 was studied (Chemin et al. 2015) and both retardation and acceleration of crack growth

rate was reported. Experiments on fatigue crack growth under TWIST (Transport aircraft Wing Structure) loading under ambient air, 3.5%, and 5% NaCl were compared. The number of flights required for the specimen to fracture increased in 5% NaCl sprayed specimen. Instead of the embrittlement effect, delay in crack growth was observed. As the crack surfaces come in contact with the saline environment, the exposed surfaces act as anodic with the adjacent region and triggers corrosion. The oxide film due to corrosion acts as a barrier for loading the crack front (Fig. 2.17). The barrier has to be broken for making the load to act on the material at the crack front and hence it takes more fatigue cycles to fracture. There exists a linear growth of the crack in the laboratory air environment with a drop in the crack growth rate. In contrast, a series of acceleration and retardation in the crack growth behavior was observed in a saline environment (Fig. 2.18).
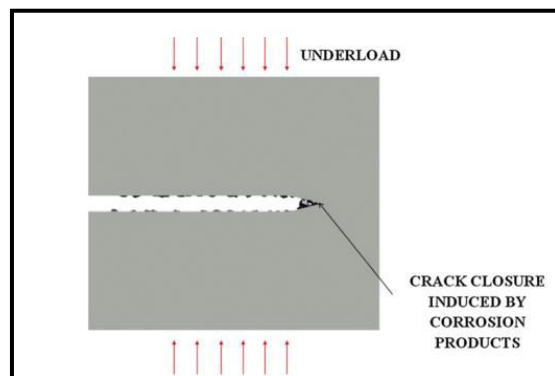
Fig. 2.17 Presence of the oxides on crack surfaces affecting crack growth (Chemin et al. 2015).

Crack growth observed under 5% NaCl had indicated a 10 times increase in fatigue life that depicts the effect of crack closure by the presence of oxides due to the corrosion and the presence of NaCl crystals. They accelerate and decelerate the crack growth rate which was responsible for the observed peaks and valleys, as shown in Fig. 2.18.
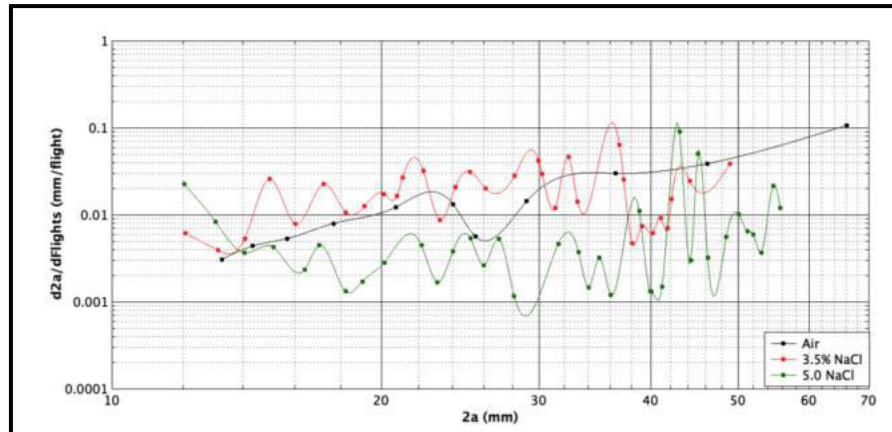
Fig. 2.18 Fatigue crack propagation rate in air, 3.5% and 5% NaCl (Chemin et al. 2015)

2.9 Tafel Plot

A basic procedure of evaluating I_{corr} is by Tafel plots. The presence of linear section in the E versus I curve is utilized in this method. The values corresponding to intersection point in the Tafel plot derives the E_{corr} and I_{corr}. Considering a uniform corrosion the corrosion current density is derived by dividing the I_{corr} by surface area. This way a Tafel extrapolation is used to determine the corrosion rate.

2.10 Research Gap

The reliability in application of RRA treated alloy to aircraft structural components is the utmost important before using it in real structures. From the literature it is understood that the FCGR studies on the RRA treated alloy at various stress ratios is not studied in detail. Also the performance of the RRA treated alloy subjected to fighter aircraft simulating loads such as FALSTAFF is not studied at all. It would be beneficial if this heat treatment could solve the problems faced by the aging aircrafts in solving corrosion related problems without sacrifice in the strength and fatigue crack growth performance of the alloy.

2.11 Objectives of the Present Study

From the review of literature it can be summarized that the RRA treatment, even though developed much earlier for retaining the peak strength of the alloy, presents

certain ambiguity on the fatigue performance of RRA treated alloy applied to structural components.

Hence following objectives were defined for the present study:

- To heat treat the alloy 7010 for T6 and RRA conditions and to characterize the microstructural features using various analytical tools, such as X-ray diffractometry, Differential Scanning Calorimetry, Optical Microscope, Scanning Electron Microscope, and Transmission Electron Microscope.

- To optimize the RRA heat treatment parameters, such as temperature and time of retrogression/reversion treatments based on the results of hardness and tensile test performance.

- To evaluate mechanical properties, such as tensile strength, microhardness, and fracture toughness of T6, T7451 and RRA treated alloy.

- To conduct constant amplitude fatigue crack growth rate tests as per ASTM E647 at different stress ratio (R= 0.1, 0.3, 0.5 and 0.7) on T6 and RRA treated alloys and compare the results.

- To conduct fatigue crack growth tests under spectrum loads i.e., Fighter Aircraft Loading Standard for Fatigue evaluation (mini-FALSTAFF) on the T6 and RRA treated alloys.

- To predict fatigue crack growth life under mini-FALSTAFF loading and compare the predicted results with that of the experimental results.

- To analyze the crack closure mechanism affecting the crack growth life for T6 and RRA treated alloys and to correlate the influence of microstructure on the fatigue crack growth behavior.
- To perform electrochemical corrosion tests and exfoliation corrosion tests on the heat treated alloys and evaluate the results.

CHAPTER 3

MATERIALS AND EXPERIMENTAL PROCEDURE

3.1 Base Material

The material used for the present research work was a commercial aluminum alloy AA 7010 in rolled form received in T7451 (over-aged) condition. The alloy composition determined by spark emission spectroscopy is presented in Table 3.1.

Table 3.1 Chemical composition of the AA7010 (wt %)

Zn	Mg	Cu	Zr	Fe	Si	Mn	Al
6.3	2.21	1.65	0.124	0.21	0.073	0.026	Balance

3.2 Peak-aging Treatment

The commercial alloy was received in over-aged condition which was solution treated by heat treating in a salt bath furnace maintained at 490 ˚C for 6 h. The solution treated alloy samples were quenched in water maintained at room temperature (25 ˚C). Further, these quenched alloy samples were aged at 120 ˚C for 24 h to obtain the T6 (peak-aging) condition (Wang et al. 2007). The heat treatment process is shown in Fig. 3.1.
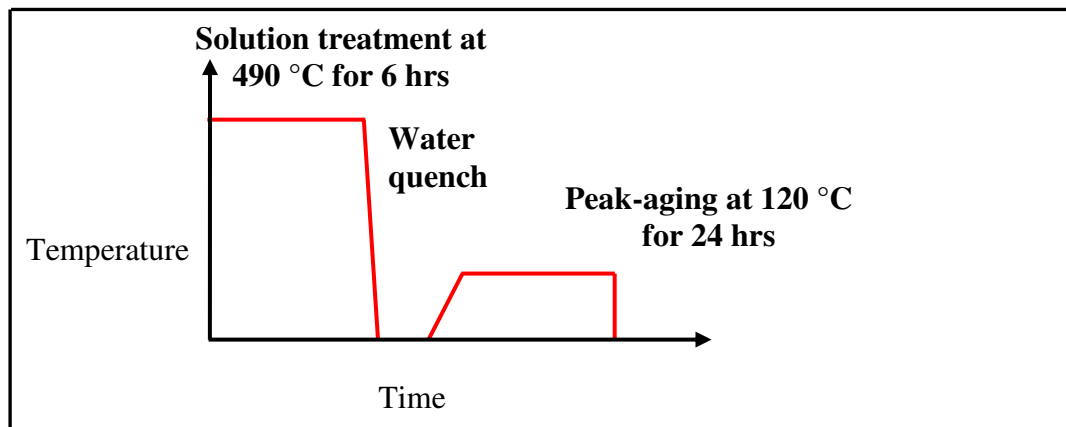
Fig. 3.1 Schematic representation of steps involved in peak-aging treatment

3.3 Retrogression and Re-Aging Heat treatment

The T7451 alloy was solutionized at 490 °C for 6 h and water quenched. It was then aged at 120 °C for 24 h to obtain T6 condition. The time duration of peak-aging treatment was optimized based on the results of hardness tests performed. Retrogression/reversion was carried by further treating the already T6 treated alloy at an elevated temperature of 200 °C for a short time interval. The alloy was again subjected to aging treatment at 120 °C for 24 h. The schematic representation of the steps involved in RRA treatment is shown in Fig. 3.2. The optimization of retrogression temperature and retrogression time was evaluated by performing a series of hardness tests on the heat treated samples (retrogression performing at different temperatures for different time intervals). The Retrogression was performed at a temperature range of 180–220 °C with different retrogression time intervals ranging for 10–60 min. Based on the results obtained, the retrogression carried out at 200 °C was considered as the optimum heat treatment for further studies. The different temper conditions performed is presented in Table 3.2.
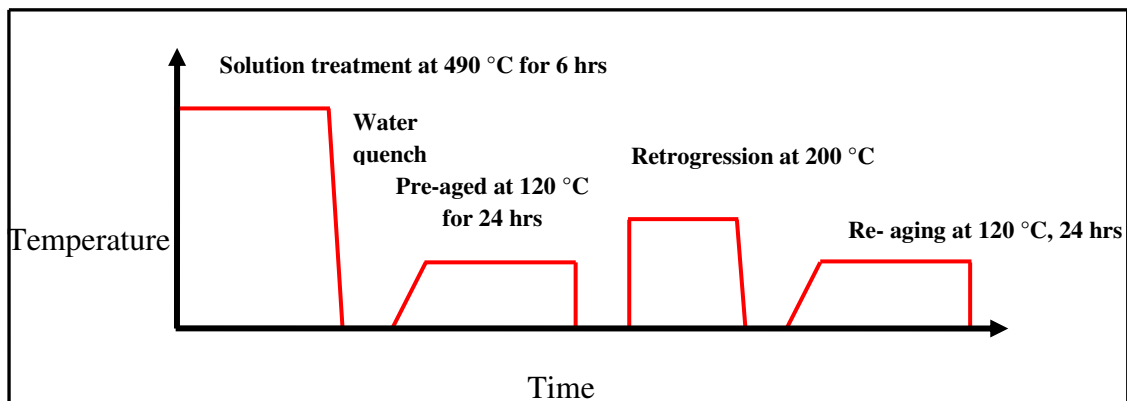
Fig. 3.2 Schematic representation of the RRA treatment

Table 3.2 Heat treatment steps adopted for AA7010

Tempering designation	Heat treatment description (measuring error ±2 °C)
T6	490 °C for 6 h + water quench + 120 °C for 24 h
RRA	490 °C for 6 h + water quench + 120 °C for 24 h+ 200 °C for 20 min + 120 °C for 24 h
T7451 (As received)	Solutionize + water quench + 115 °C for 8 h + 165 °C 16 h

3.3.1 Salt bath furnace

Figure 3.3 shows the salt bath furnace used for performing heat treatments on the received alloy. The furnace consists of stainless steel tank of 12 liters capacity. The temperature of the bath was controlled by using a PID controller attached to the furnace. The temperature measuring thermocouple was directly immersed in the salt bath. The salt mixture consisting of KNO_3 and $NaNO_3$ in 50:50 (wt %) fraction was used for solution treatment of the alloy at 490 ˚C. A mixture of salts containing KNO_3, $LiNO_3$ and $CaNO_3$ in the mole fraction of 0.58:0.31:0.11 was used for performing peak-aging (120 °C) treatment of the alloy. The salt bath furnace was used for the heat treatment process specifically to attain uniform heat treatment across the thickness of alloy.

Fig. 3.3 Salt bath furnace used to carry out heat treatment

3.4 Microstructural Characterization

3.4.1 Optical microscopy

Optical microscope (Zeiss make, model: AXIO Lab.A1) was used to observe the change in grain size and change in grain morphologies of the heat treated alloy samples. The samples were prepared by progressive polish on SiC emery papers of size 400, 800, 1200 and 2000 after which a cloth polish by using alumina paste and

finally etched by using Keller's etchant (190 ml distilled water, 5 ml HNO_3, 3 ml HCl and 2 ml HF) .

3.4.2 X-ray diffractometry

X-ray diffraction on the samples from the base material 7010 in T7451, T6 and RRA conditions were obtained by using an X-ray diffractometer (model JDX 8P, JEOL make, Japan) operated at 30 kV voltage and 20 mA current. A monochromatic copper K_{α} (λ=0.154 nm) radiation was used for obtaining the diffraction peaks. The diffraction peaks were collected in the range of 2θ values from 5 ° to 90 ° at the scan speed of 1 °/min and a step size of 0.02 °. The output data was analyzed by comparing with the standard JCPDS files to identify the corresponding peaks from the base material and the precipitates.

3.4.3 Differential scanning calorimetry

Differential scanning calorimetry (DSC) was performed on heat treated alloy sample with a heating rate of 10 °C/min using NETZSCH DSC 404 equipment. A 10 mg sample cut from the treated alloy was used to perform DSC experiments.

3.4.4 Transmission electron microscopy

Transmission electron microscope (JEM-2100, JEOL make) equipped with EDS (Oxford make) was used to characterize the nano scale precipitates evolved during different heat treatment processes. TEM samples were prepared by mechanically thinning down to 80 μm. Discs of 3 mm diameter were punched from the thin section and followed by lapping to make the sample flat. The samples were dimpled to 15 μm using the dimpling unit (Gatan make). The procedure adopted for TEM sample preparation is shown in Fig. 3.4. Ion milling was carried out on the dimpled region by using a Gatan PIPS instrument with a beam energy of 5 keV at a beam angle of 6 ° top and 6 ° bottom followed by fine milling at 2 keV. The ion milled sample near to the hole region was observed to reveal the microstructural features and to get the SAED patterns from the base material and the precipitates. The chemistry of the GBP's (grain boundary precipitates) was measured with help of the EDS attached to TEM. The TEM and sample preparation units are shown in Fig. 3.5.
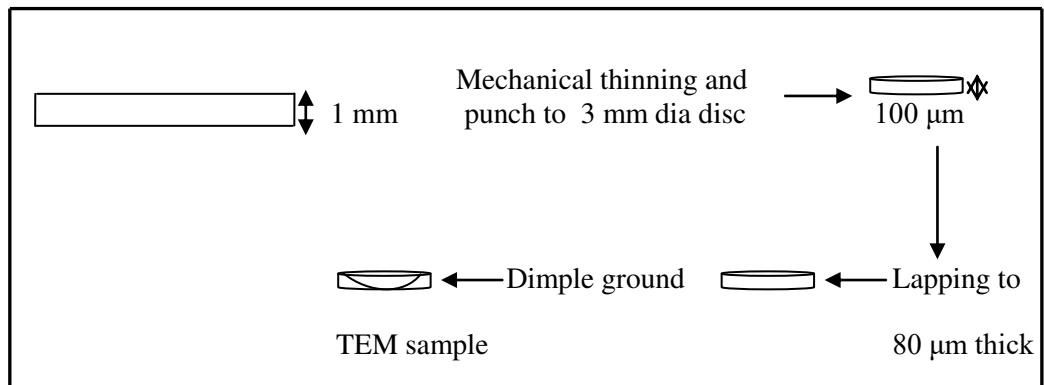
Fig. 3.4 TEM Sample preparation steps

Fig. 3.5 a) Transmission electron microscope JEOL-JEM 2100, b) PIPS ion milling unit

3.4.5 Scanning electron microscopy

The fracture surface morphologies of the tensile tested specimens, fracture toughness, and fatigue crack growth test specimens were analyzed by using a scanning electron microscope (SEM: JSM-6380LA model, JEOL make) equipment.

3.4.6 Confocal microscopy

The fatigue fractured surfaces were observed under a confocal microscope (Olympus LEXT 4000 make) to measure the surface roughness characteristics, such as peak roughness and average roughness after performing the fatigue crack growth tests.

3.5 Mechanical Characterization

A series of microhardness tests, tensile tests, and fracture toughness tests were carried to evaluate the mechanical properties.

3.5.1 Microhardness test

The hardness of the alloy samples in different heat treatment conditions was evaluated by performing the microhardness tests using Vicker's microhardness instrument (make Shimadzu, model: HMV-G 20ST). The indenter used was a square based pyramid indenter having 136 degree angle between the opposite faces. The indentation load applied was 500 gms and the indentation time maintained was 15 seconds. A microscope attached to the indenter set up was used to measure the indentation size. The direct readout Vicker hardness number (Hv) was recorded and an average of five readings were measured and reported with the standard deviation.

3.5.2 Tensile test

Standard tensile tests were performed by following ASTM E8 (ASTM E8 2010), using a universal testing machine (UTM, Shimadzu make, model: AG-X plus) of 100 kN capacity. During the test, a crosshead speed of 1 mm/min was maintained. Figure 3.6 shows the dimensions of the tensile test specimen which was cut such that the loading direction was along the longitudinal direction of rolling.
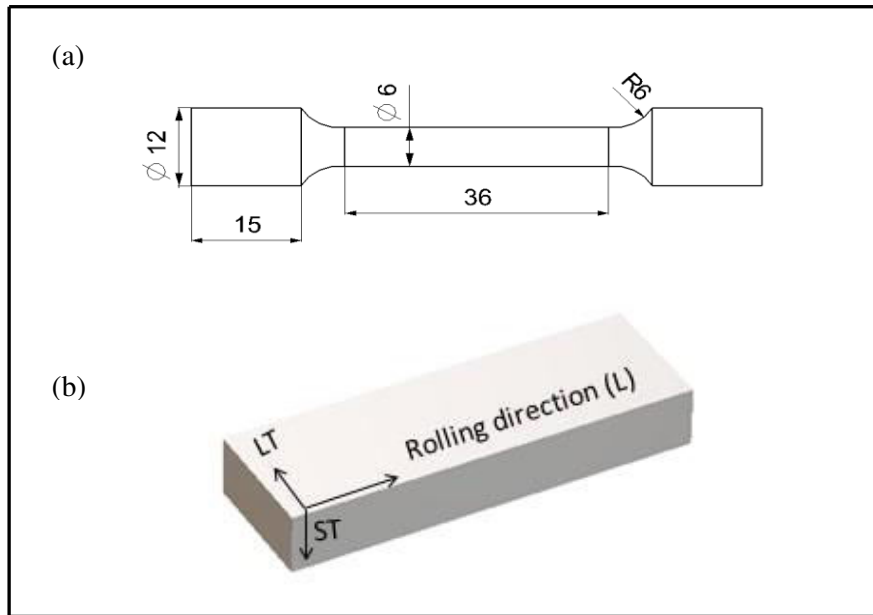
Fig. 3.6 a) Tensile test specimen (all dimensions in mm) b) Schematic representation of the rolled aluminum block

3.5.3 Fracture toughness test

Linear elastic fracture toughness tests were conducted on the compact tension specimens as per ASTM E399. The specimen was cut from the aluminum block such that the loading direction was along the longitudinal (L) and crack plane along LT direction. CT specimens were machined to a thickness of 25.6 mm as shown in Fig. 3.7. Fracture toughness of the material assumed as 30 MPa√m, with a known yield strength of the material (514 MPa for RRA condition). The minimum size of the CT specimen required to ensure plane strain condition is presented in Table 3.3. The thickness of the specimen considered is validated according to linear elastic fracture mechanics. The crack length including notch length (12.7 mm) with a fatigue pre-crack of 1.26 mm was maintained. During pre-cracking, a cyclic loading with K_{max} of less than (0.8*30 MPa√m) was maintained as per standard procedure.

Table 3.3 CT specimen size calculations

Thickness of the CT specimen	$B \geq 2.5(K_{IC} / \sigma_{YS})^2$	24 mm
Fatigue pre-crack length	$a \geq 2.5(K_{IC} / \sigma_{YS})^2$	24 mm
Width of the specimen	$W \geq 5(K_{IC} / \sigma_{YS})^2$	50 mm
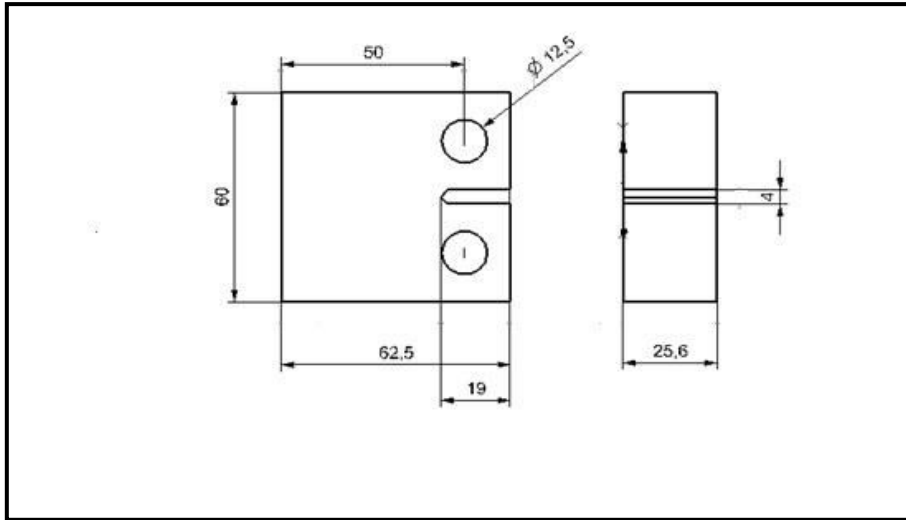
Fig. 3.7 Compact tension specimen for fracture toughness test (size in mm) (ASTM E399 2013)

3.6 Fatigue Crack Growth Tests

3.6.1 Fatigue crack growth rate (FCGR) tests under constant amplitude loads

FCGR tests under CA loading were performed on the CT specimens. The dimensions of the CT specimen used for testing is shown in Fig. 3.8. The tests were carried as per ASTM E647 at a different stress ratio, ranging from 0.1 to 0.7. The standard CT samples of 50.2 x 60 x 12.5 (W x H x B dimensions in mm) size were adopted for performing the tests. The samples were machined from a plate oriented in LT direction. A straight cut V notch was machined to initiate the pre-crack on the CT specimen. The FCGR tests were performed by using the Instron make machine, model:8801 of 100 kN capacity shown in Fig. 3.9 maintained in laboratory air atmosphere. The decreasing ΔK tests by load shedding method was carried until the near-threshold data are acquired, i.e., till the crack growth rate of 1×10^{-6} mm/cycle was reached. The specimen was then subjected to constant load (increasing ΔK) tests till the final fracture of specimen. The fractured surfaces were observed under a scanning electron microscope to reveal the fracture behavior at various domains of fatigue crack growth.
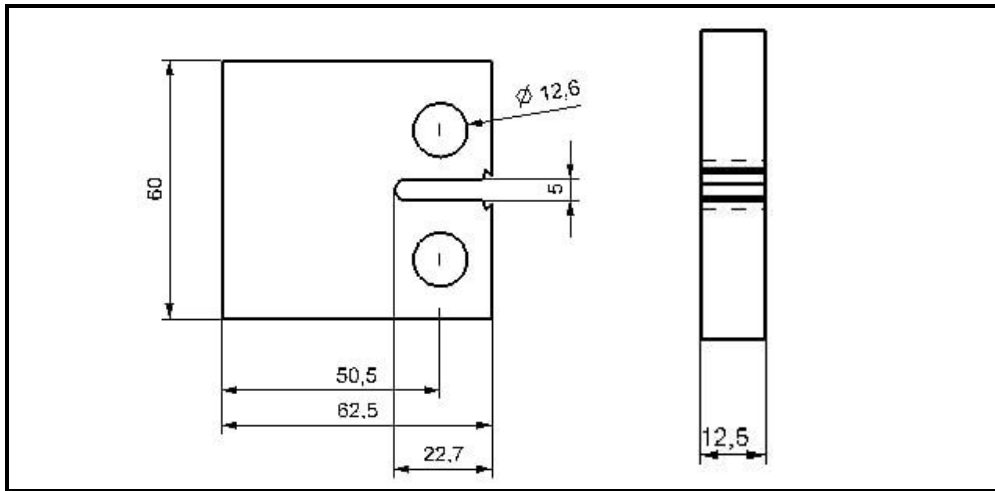
Fig. 3.8 Schematic diagram showing test specimens used to conduct FCGR tests; Compact tension (CT) (All dimensions in mm)
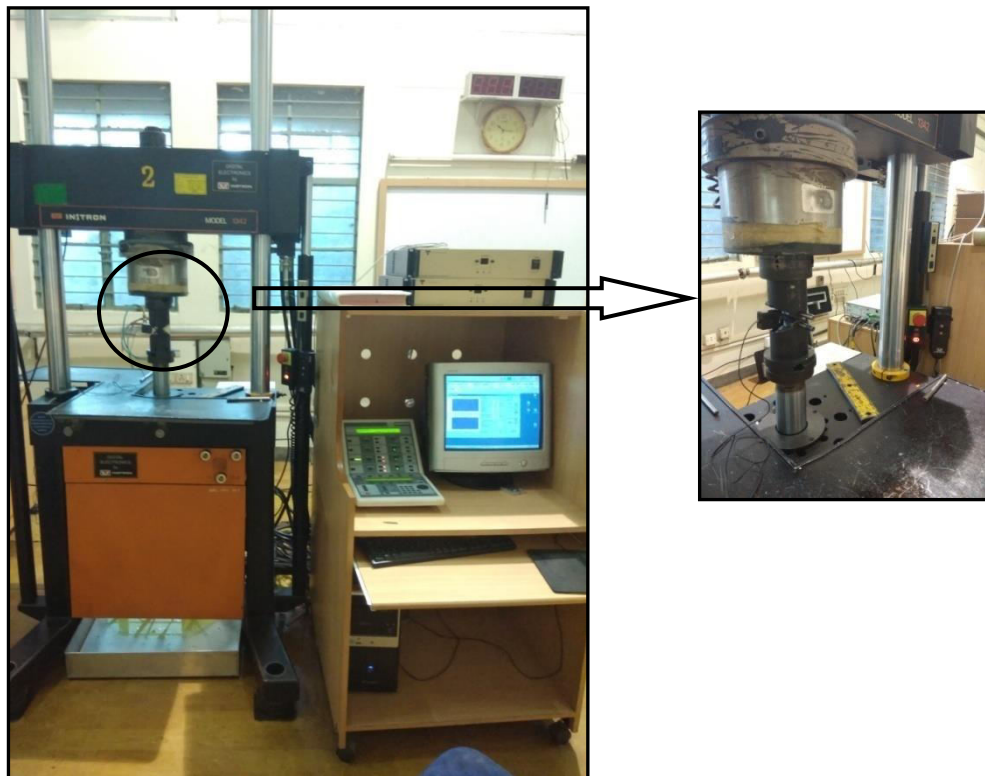
Fig. 3.9 Computer controlled servo-hydraulic fatigue test equipment (Instron make, model: 8801)

3.6.2 Fatigue crack growth tests under service simulating loads

Fatigue crack growth performance of the alloy under a standard load sequence was carried. A fighter aircraft loading standard, mini-FALSTAFF (Heuler and Klatschke 2005) as shown in Fig. 3.10 was considered for this investigation. The service spectrum load applied was a short version of the standard FALSTAFF load spectrum, which is a standardized variable amplitude test load sequence developed for the fatigue analysis of materials used for fighter aircraft. In Fig. 3.10, the normalized load is plotted against peak/trough points of load sequence. One block of this load sequence consists of 18,012 reversals at 32 different stress levels and represents the loading equivalent of 200 flights. The load sequence for our experiments was obtained by multiplying with a constant reference load value, P_{ref} =15 kN for all the peak/trough points in the entire block.
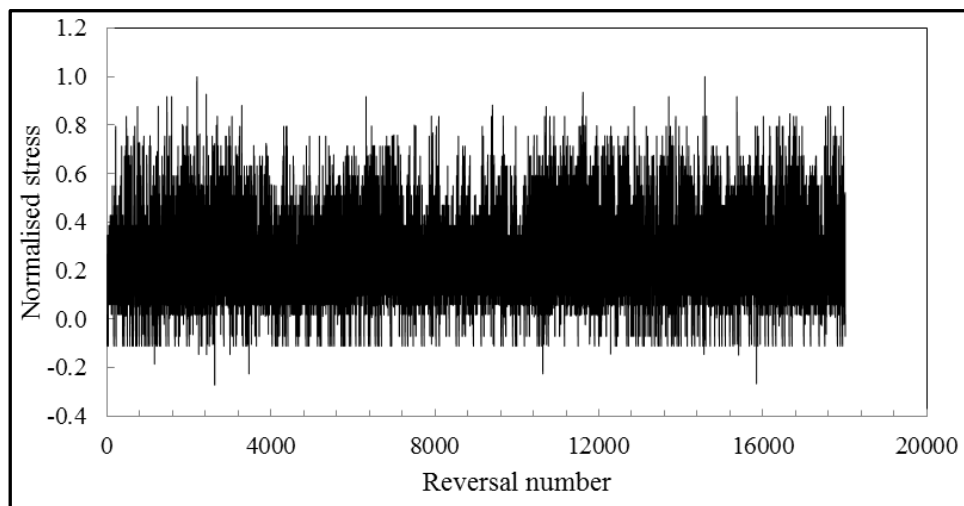
Fig. 3.10 Mini-FALSTAFF spectrum load sequence (Heuler and Klatschke 2005)

The tests were conducted in a computer controlled 100 kN servo-hydraulic test machine (Instron make, model:8801). Triangular waveform of load with an average frequency of 3 Hz (6 reversals per second) was employed in the tests. The crack length was measured by using a traveling microscope. The crack length on either side of the specimen was measured after every load block and the average crack length, corresponding load block number was noted. Initially, the specimen was pre-cracked under fatigue loads. Further, the specimen was subjected to FALSTAFF spectrum load block tests. The experiment was continued until failure of the specimen.

3.6.3 Spectrum fatigue crack growth prediction

The fatigue crack growth behavior and crack propagation life of 7010 aluminum alloy under the standard mini-FALSTAFF load sequence was predicted by adopting a two parameter crack growth law and a crack closure based model for both T6 and RRA treated alloys and the results were compared with the experimental results.

3.7 Electrochemical Corrosion Tests

3.7.1 Potentiodynamic polarization tests

Potentiodynamic polarization experiments were carried out with a scan rate of 1 mV/s using the Bio-logic instrument with three electrode flat cell configuration. The test set up with Pt as a counter electrode and saturated calomel as a reference electrode was used. The heat treated alloy samples for the corrosion tests were prepared by progressive polishing from 400 to 2000 grits of SiC emery papers. A sample of 1 cm^2 exposed area was immersed in a 3.5 % NaCl solution at 25 °C. Three trials were carried out for each heat treated condition. Tafel type fit was performed to estimate the corrosion current density (i_{corr}) with the aid of an EC lab tool. The corrosion test samples of different heat treated conditions were observed under the light microscope and scanning electron microscope to visualize morphology of corrosion pits and the corroded surface area.

3.7.2 Exfoliation corrosion (EXCO) tests

The standard EXCO tests were performed on the polished samples as per ASTM G34-01 (ASTM G 34-01 2001) test standards. The samples were cut and heat treated in a salt bath furnace. The heat treated specimens were then polished with emery paper of grit size 400-1200 grades. The polished alloy samples were then immersed in the test solution prepared with a mixture of 4 M sodium chloride, 0.5 M potassium nitrate and, 0.1 M nitric acid for 48 h, maintained at a laboratory air environment. The solution was prepared in such a way as to get 20 ml/cm^2 of solution to exposed surface area. The exfoliated surfaces were then cleaned with ethanol and observed under optical microscope and SEM to analyze the depth of exfoliation, severity of exfoliation damage etc.

Page left intentionally blank

CHAPTER 4

MICROSTRUCTURE AND MECHANICAL CHARACTERIZATION

4.1 Optical Microscopy

4.1.1 Aluminum 7010 alloy in different heat treated conditions

The aluminum alloy is received in over-aged condition (T7451) in rolled thick plate form. The microstructure of the alloy under optical microscope (OM) is shown in Fig. 4.1. The average grain size of the alloy in three different rolling directions are measured to be about 15 μm, 10 μm and 8 μm in the longitudinal, LT and ST directions respectively. The elongated morphology of grains is observed along the rolling direction as shown in Fig. 4.1 (a and b).
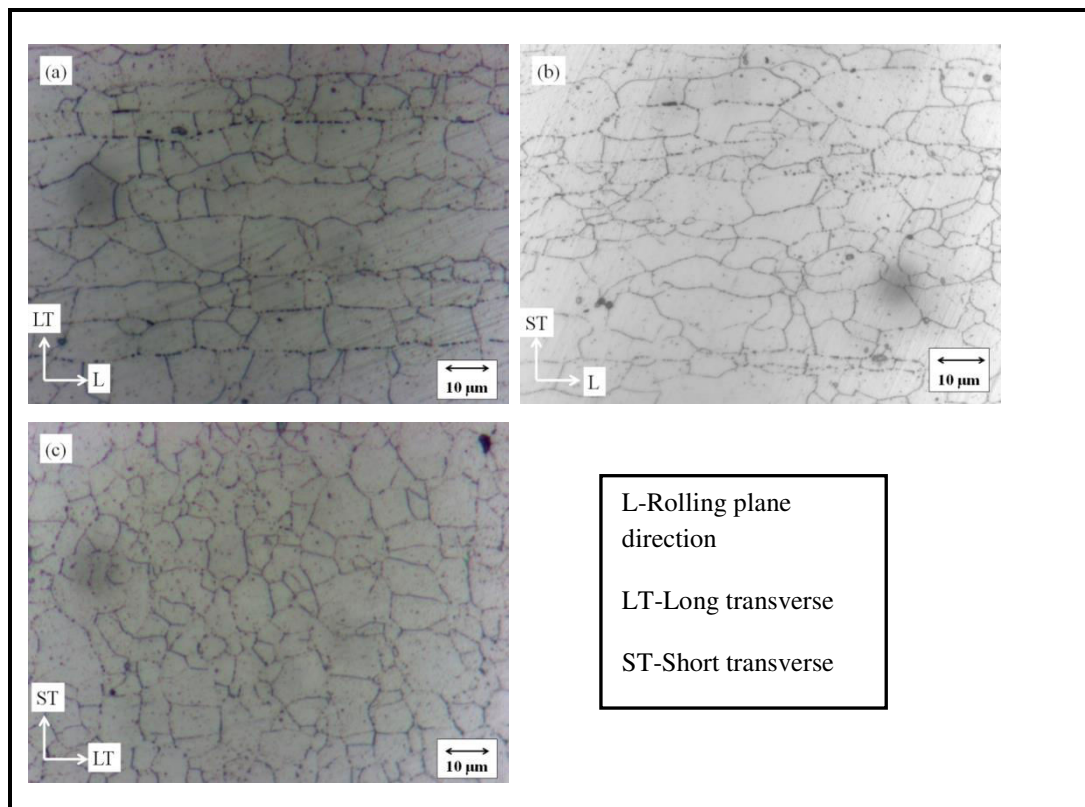
Fig. 4.1 Optical micrographs of the alloy in different rolling directions

The alloy microstructures (i.e., grain interior) after solution treatment are observed and shown in Fig. 4.2 (a-c). For T6 treated alloy the average grain size is measured to be about 165 μm, 178 μm and 70 μm in the longitudinal, LT and ST directions respectively. The variation in grain size in different heat treatment conditions is shown in Fig. 4.4. Very fine secondary phase precipitates that are evolved in matrix during heat treatment could be seen in the highly magnified image in Fig. 4.2 (d).
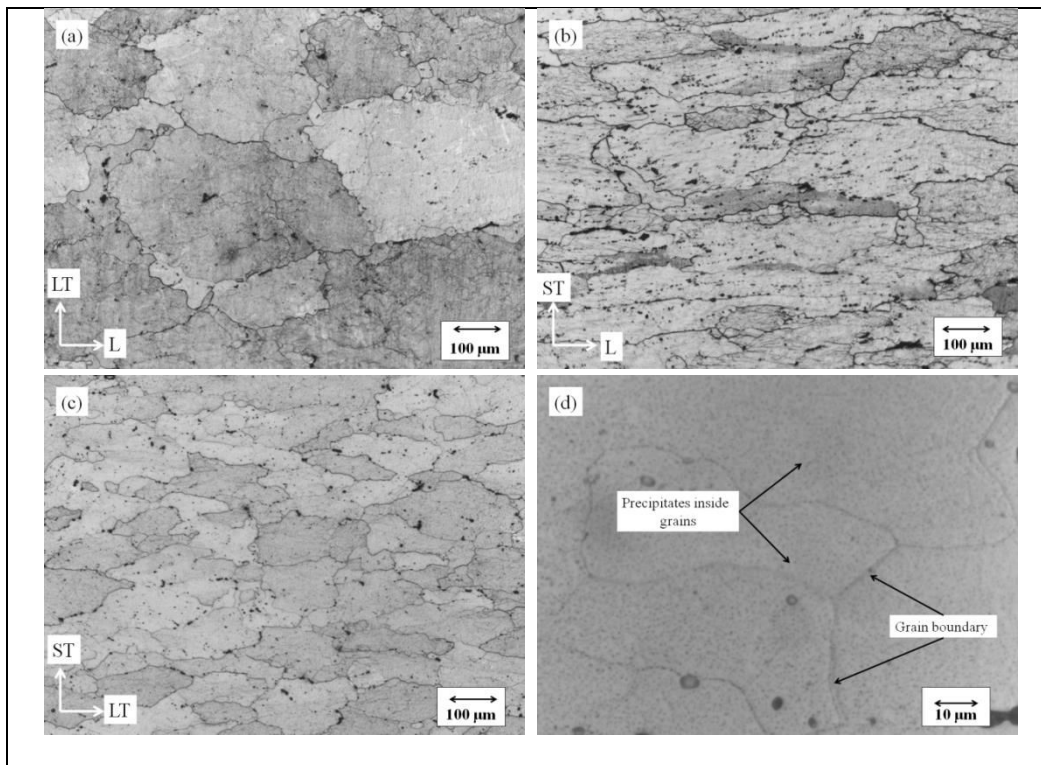
Fig. 4.2 Optical micrographs of the alloy in T6 condition observed along different rolling directions; a) Longitudinal, b) Short transverse, c) Long transverse, d) Magnified image of the alloy matrix

The OM micrographs in Fig. 4.3 shows the grain morphologies of alloy in the RRA treated condition. The average grain size after RRA temper is measured to be about 162 μm, 134 μm and 68 μm in the longitudinal, LT and ST directions respectively. The heat treated alloys, such as in T6 and RRA conditions show similar characteristics of grain growth and sub-grain formation which is evident from the OM micrographs shown in Fig. 4.5. The grain size variation in T6 and RRA (Fig. 4.4) is marginal and therefore the study is carried out neglecting the influence of grain size on hardness and tensile properties.
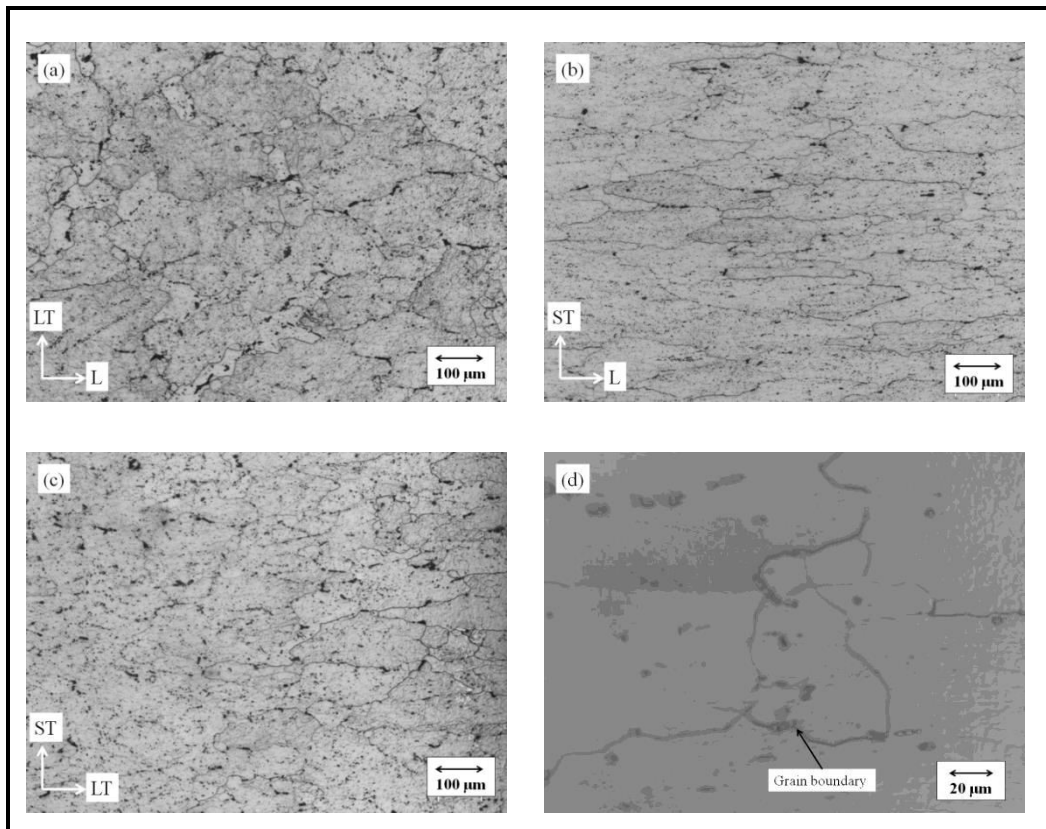
Fig. 4.3 Optical micrographs of the alloy in RRA condition observed along different rolling directions; a) Longitudinal, b) Short transverse, c) Long transverse, d) Magnified image of the alloy matrix
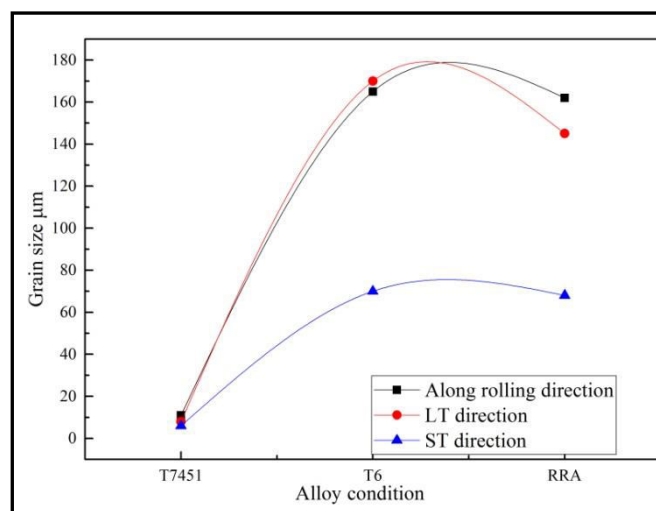
Fig. 4.4 Grain size variation with different tempering conditions
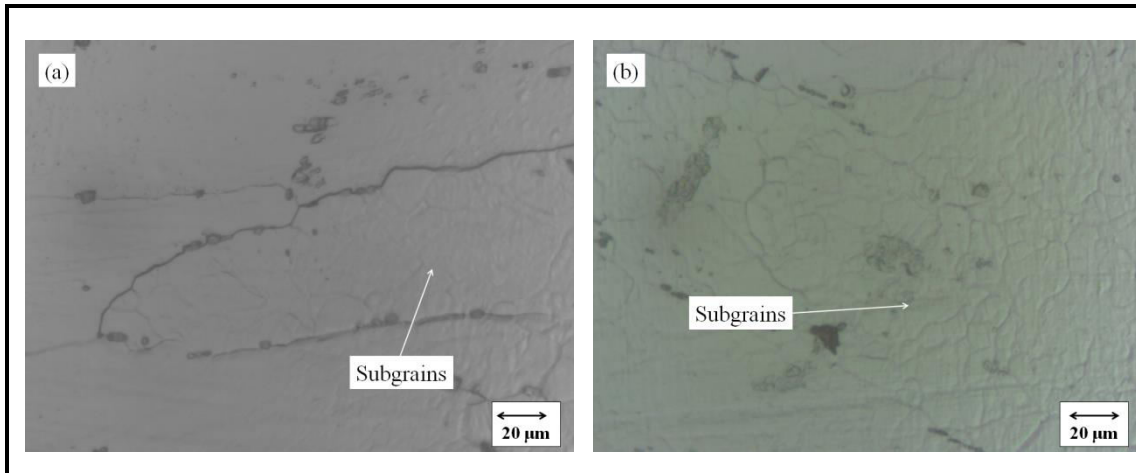
Fig. 4.5 Optical micrographs showing the sub-grain formation after heat treatment; a) T6, b) RRA

4.2 X-ray diffractometry

The typical XRD peaks from the scan performed on the rolling direction of alloys, in solutionized, T6, RRA, and T7451 conditions are presented in Fig. 4.6. The five major XRD peaks at (111), (200), (220), (311) and (222) (JCPDS Al-04-0787) confirm the aluminum alloy matrix. The presence of $MgZn_2$ precipitates is confirmed by the peaks corresponding to planes (110), (112), (212), (006) and (106) as per JCPDS 01-077-1177.
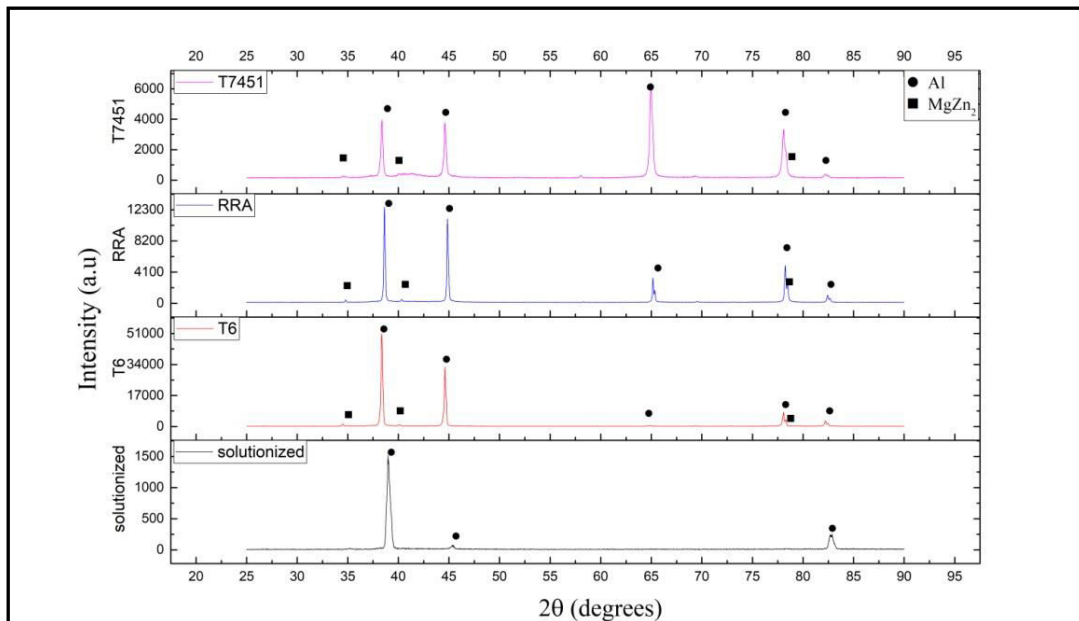
Fig. 4.6 XRD pattern of the alloy in different heat treatment conditions (scan performed on rolling plane in longitudinal direction)

4.3 Transmission Electron Microscopy Characterization

4.3.1 Microstructure of the alloy in as-received condition (T7451)

The transmission electron microscopy performed on the as-received aluminum alloy (i.e., T7451) is presented in Fig. 4.7. The alloy matrix is found to be occupied with widely spaced precipitates, having a precipitate size of 8-12 nm (Fig. 4.7 a). The alloy matrix predominantly consists of disc shaped coarse η precipitates with size ranging 20-45 nm. The η are the $MgZn_2$ precipitates as identified from SAED patterns in 4.7 (d), taken along $[122]_{Al}$ direction. The diffused ring corresponds to the presence of η ($MgZn_2$) precipitates. The average size of GBP's and PFZ are measured to be about 60 nm and 70 nm respectively and they are shown in Fig. 4.7 (c).
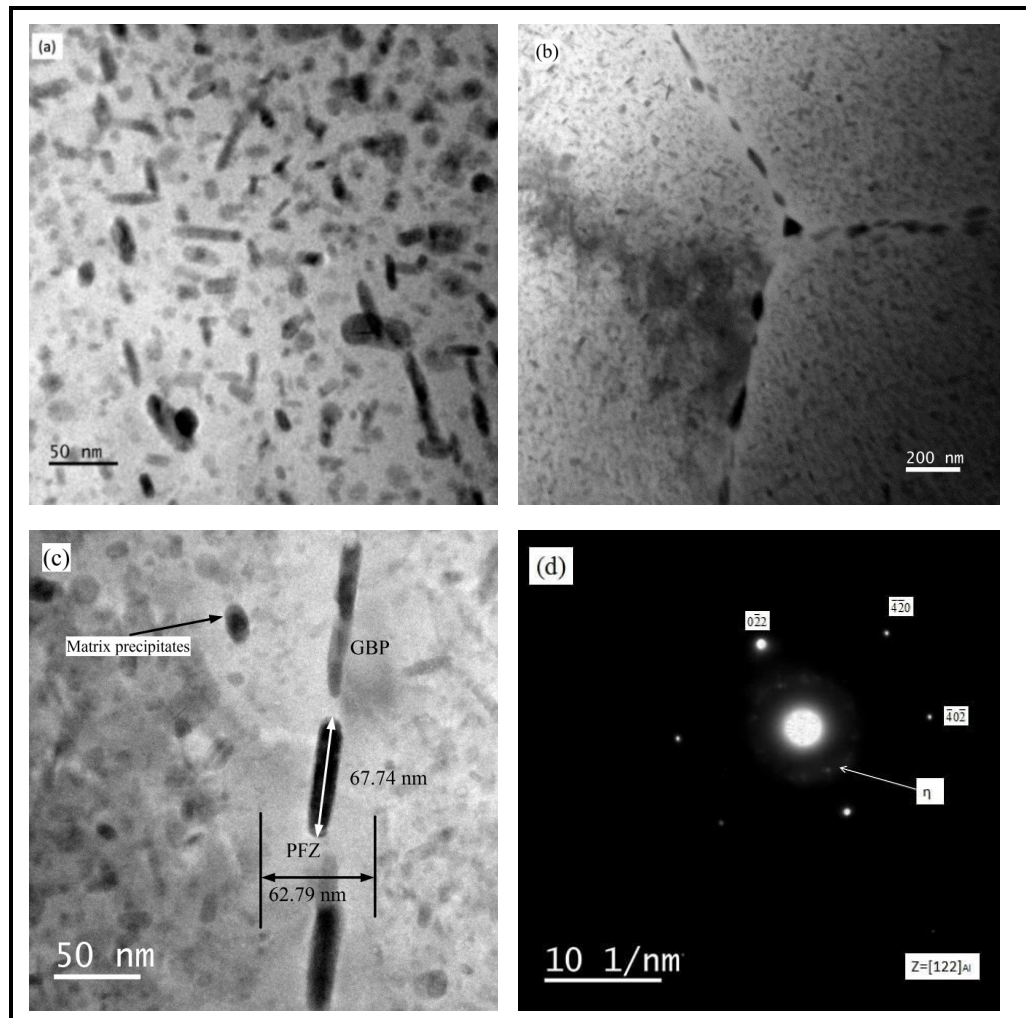
Fig. 4.7 Bright-field TEM micrographs of the alloy in T7451 condition a) Matrix, b) Grain boundary precipitates, c) High magnification micrographs of grain boundary, d) SAED pattern of the aluminum matrix with inner spots from η precipitate

4.3.2 Microstructure of the alloy in T6 condition

Figure 4.8 shows the bright-field TEM micrographs of the aluminum alloy heat treated in T6 condition. The matrix of the T6 treated alloy is dispersed with fine scale metastable precipitates, η' (MgZn$_2$) of size varying from 3-5 nm. This is similar to the observations in earlier reports (Buha et al. 2008; Marlaud et al. 2010a). The grain boundaries of T6 alloy samples are found to be occupied with the precipitates which are thin and continuous in form. The thickness of the continuous GBP's vary from 3-15 nm in size. The precipitate free zone (PFZ) around the GBP's is found to vary from 20–30 nm in size. The precipitates in the matrix are found to be of uniform size and are denser and closely packed to an extent as the distance of separation between each other is measured to be about 3-4 nm.
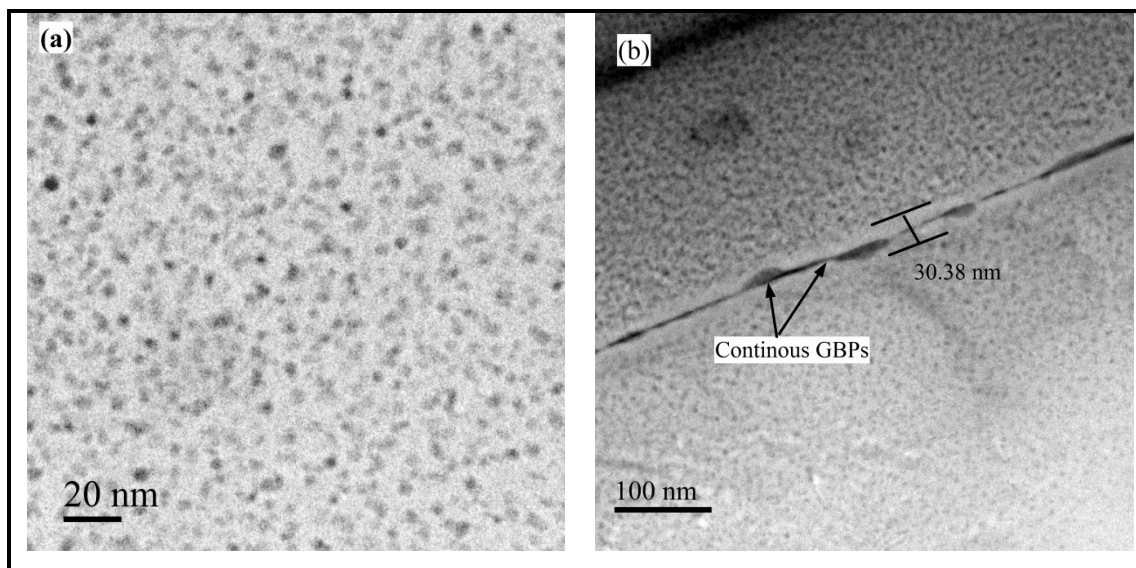
Fig. 4.8 Bright-field TEM micrographs of the alloy in T6 treated condition; a) Matrix, b) Grain boundary

4.3.3 Microstructure of retrogression/reversion treated alloy

The bright-field TEM micrographs of the alloy after performing the reversion treatment at 200 °C for 20 min are presented in Fig. 4.9. It is evident from the microstructure that the density of precipitates has been reduced after retrogression/reversion stage of heat treatment (Fig. 4.9 a). At this stage of heat treatment, there exist two kinds of matrix precipitates, such as the spherical shaped precipitates of an average size of 6 nm and an elongated disc shaped precipitates of an average size of 10-12 nm. During the retrogression stage, the GBP's get coarsened and become discontinuously arranged as shown in Fig. 4.9 (b). The average GBP's size is found to be about 25 nm having an average interspacing of 15 nm. The PFZ size is measured to be about 40 nm. The precipitate size distribution in the matrix after reversion treatment is presented in Fig .4.10. The majority of precipitates are found to be grown with a size range of 5-10 nm unlike the fine precipitates of 3-4 nm observed in the T6 treated sample.
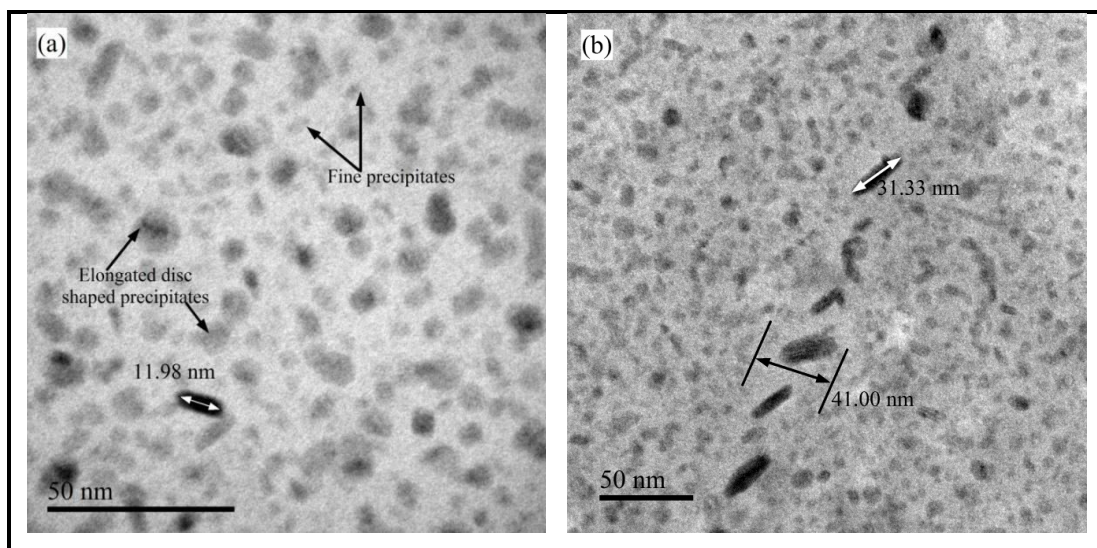
Fig. 4.9 Bright-field TEM micrographs of the alloy after reversion treatment at 200 ˚C for 20 min; a) Matrix, b) Grain boundary
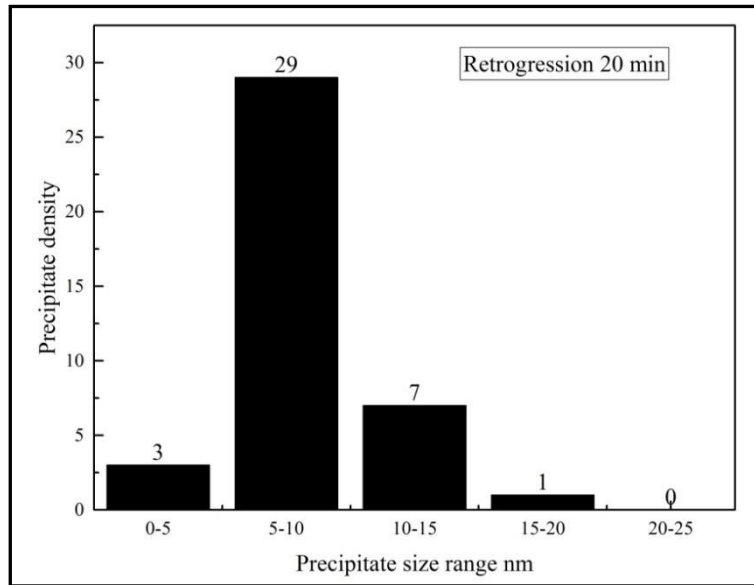
Fig. 4.10 Size distribution of the matrix precipitates after reversion treatment at 200 ˚C for 20 min

4.3.4 Effect of retrogression time on the microstructure of alloy

The microstructure of the RRA treated alloy with retrogression performed at 200 °C for different retrogression duration, varying from 10-60 min with the time increment of 10 min is presented in Fig. 4.11. The precipitate size distribution plot for RRA treated alloy for varied retrogression time is shown in Fig. 4.12. The precipitate size is measured on the TEM micrographs by selecting a reference area of about 120x120 nm^2 square area. When the retrogression time higher than 30 min, the pre existed smaller sized precipitates grow further to become larger in size of about 25-30 nm as evidenced from the distribution plot in Fig. 4.12.
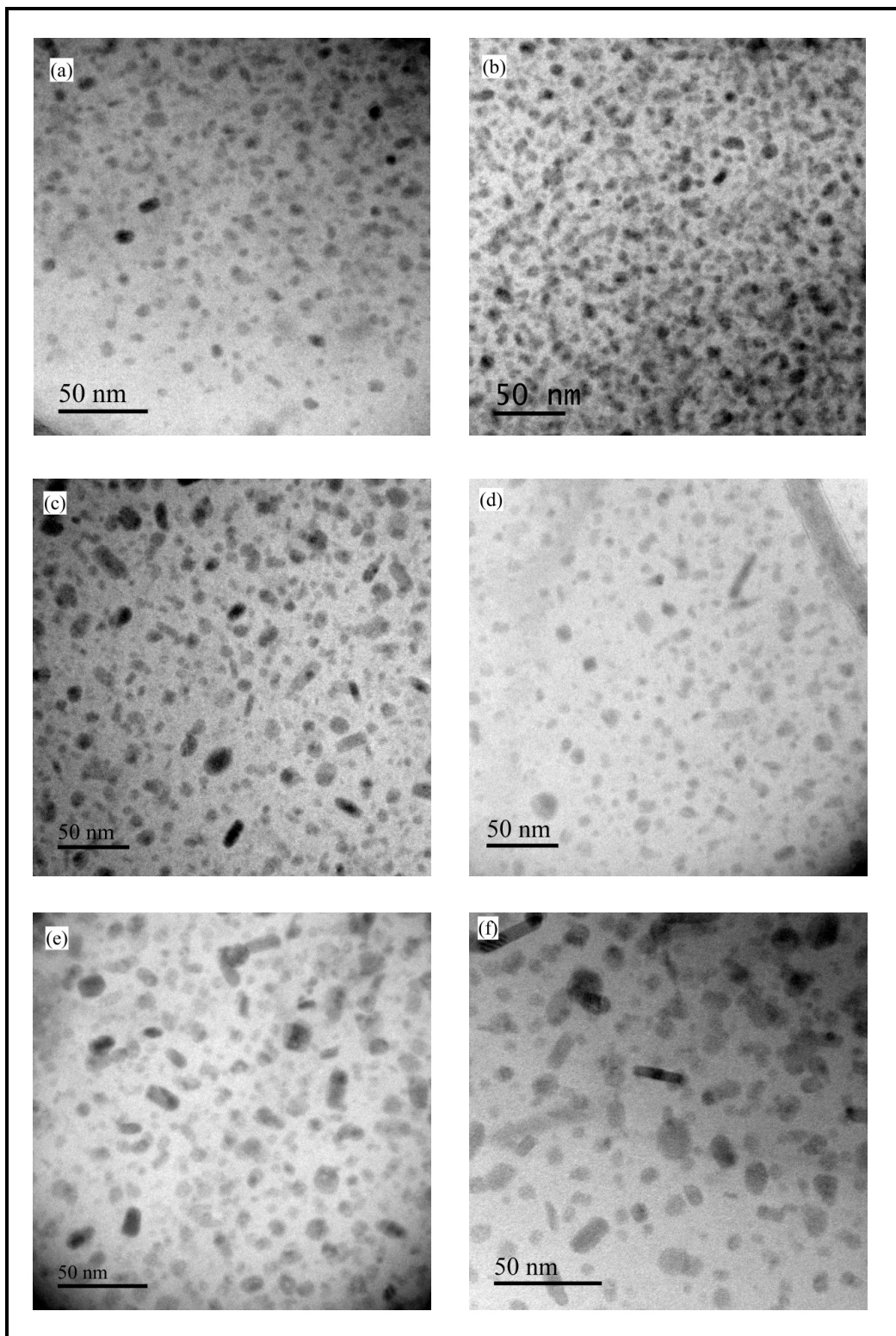
Fig. 4.11 Bright-field TEM micrographs of the RRA alloy; reversion at 200 ˚C for different time intervals a) 10, b) 20, c) 30, d) 40, e) 50, f) 60 minutes

51
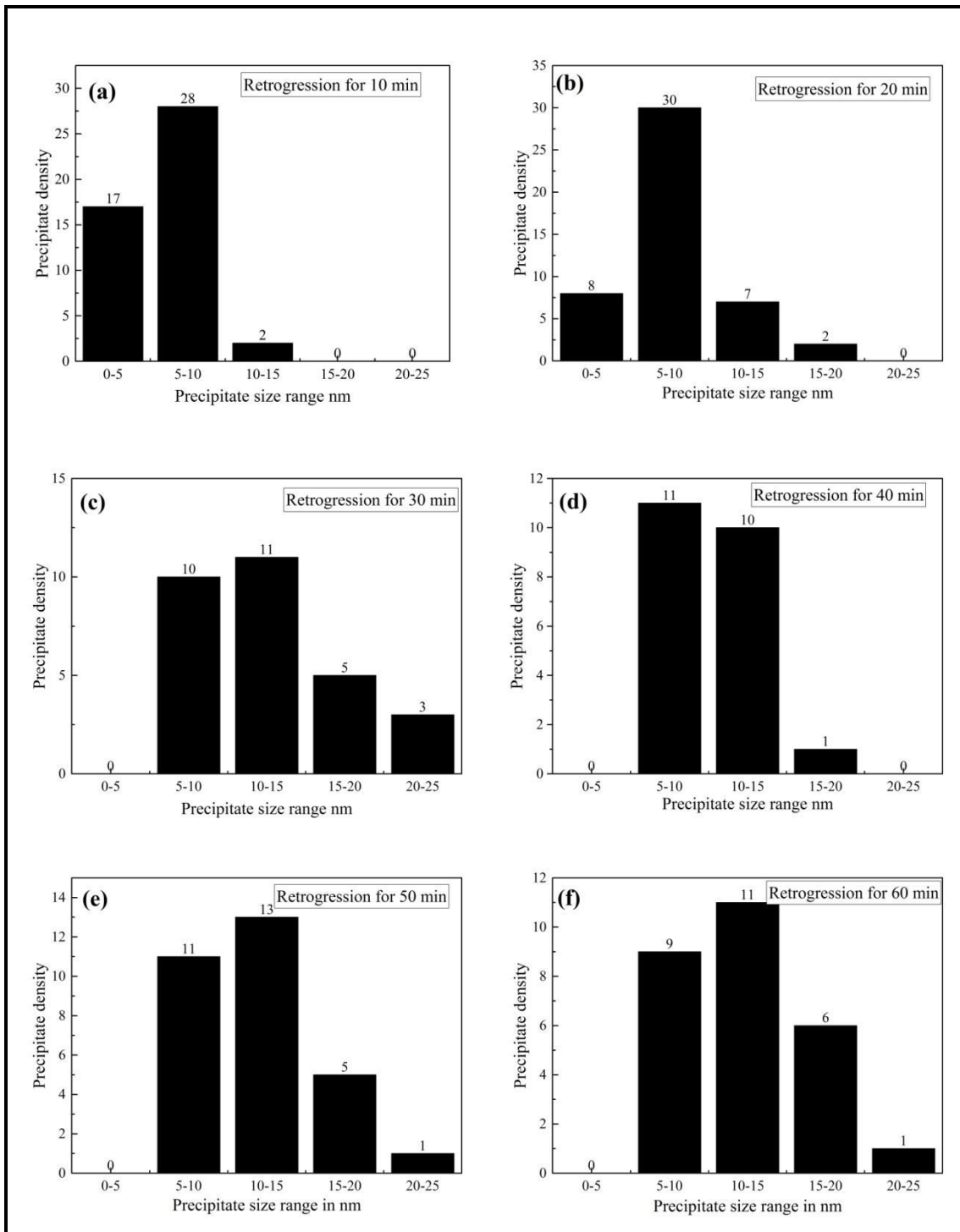
Fig. 4.12 Size distribution of the matrix precipitates in the RRA sample with varied retrogression time

4.3.5 Effect of retrogression and re-aging of the alloy

The retrogression treated alloy samples are re-aged to peak-aging condition by aging the reversion treated alloy sample to 120 °C for 24 hrs. The microstructure of the RRA treated samples are shown in Fig. 4.13. During the re-aging stage of RRA, the already dissolved solutes (during reversion) get re nucleated evolving fine precipitates of average size 5-8 nm. These precipitates are η' semi-coherent in nature, as identified by the diffused spots (Fig. 4.14) at 1/3 and 2/3 of 220_{Al} position in $[111]_{Al}$ of SAED from the matrix (Buha et al. 2008). The SAED spots corresponding to η' are in line with planes (202) of the aluminum matrix indicating the precipitates are coherent in nature. The second type of precipitates which are grown for about size 15-20 nm. The GBP's are more widely spaced forming an average interspace of about 24 nm. The width of the precipitate free zone (PFZ) is found to vary in the range of 35-38 nm which is slightly higher than that of the T6 treated sample. The size of the precipitates with different morphologies and PFZ size after different heat treatments are quantified and pictorially represented in Fig. 4.15. An increase in inter precipitate distance by about 6-15 nm was evident in the RRA tempered condition compared to T6 condition.
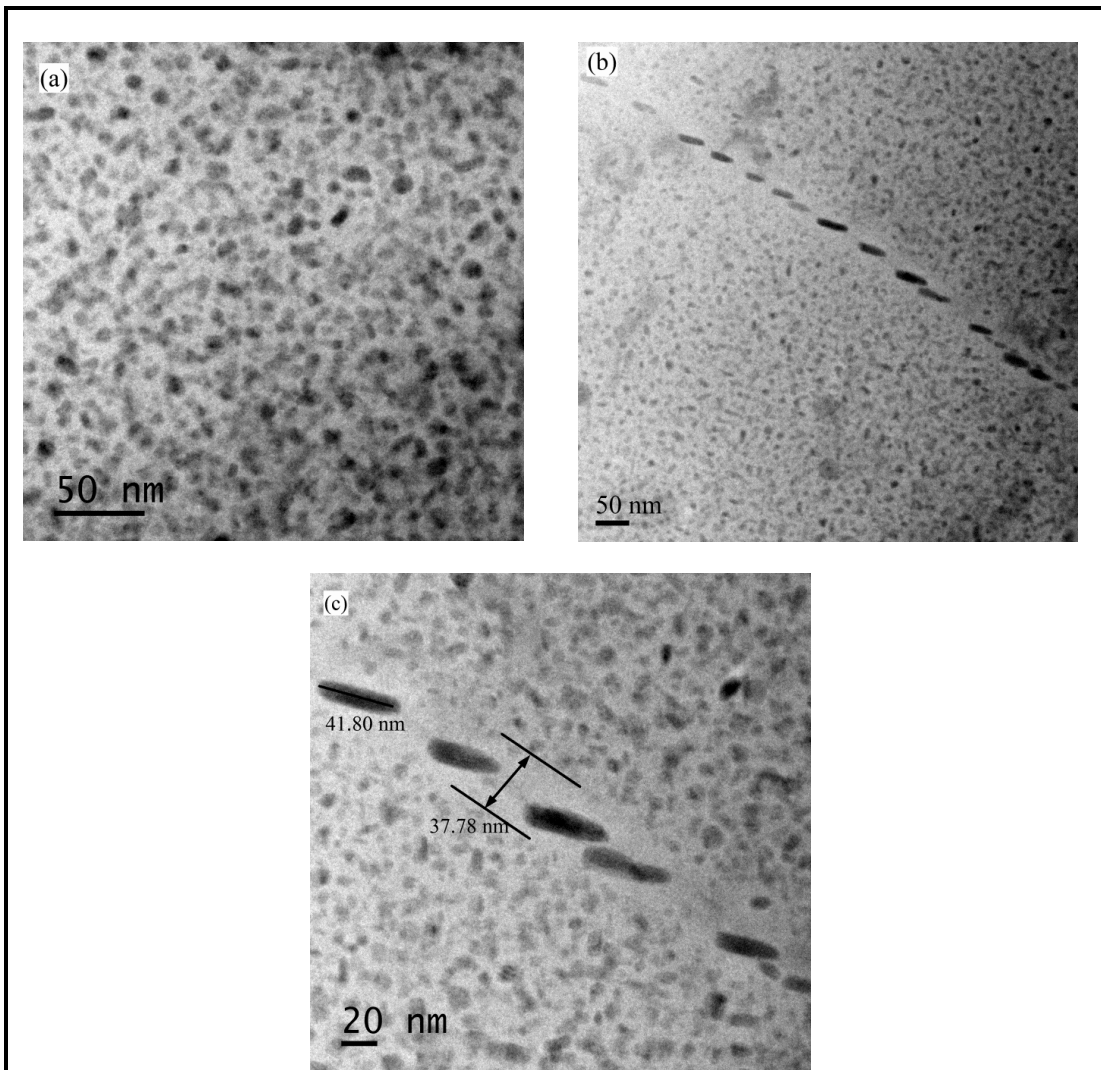
Fig. 4.13 Bright-field TEM micrographs of the RRA 200-20 min treated alloy; a) Matrix, b) Grain boundary, c) High magnification micrographs of grain boundary region
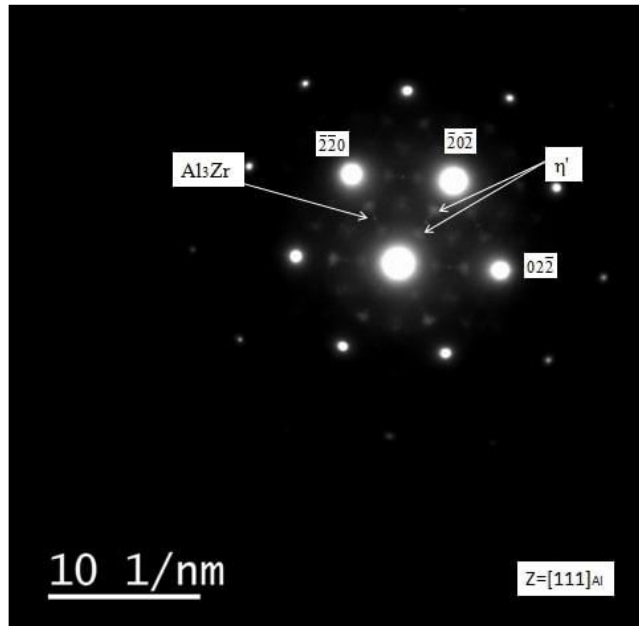
Fig. 4.14 SAED from the RRA alloy matrix taken on $[111]_{Al}$ zone axis

The sharp diffraction spots at 1/5 of 220_{Al} confirm the presence of dispersoids of Al_3Zr (Ge et al. 2001) (Fig. 4.14) which generally acts as pinning sites for the grain boundaries, thereby helps in suppressing the grain growth and re-crystallization during high temperature treatment (Buha et al. 2008).
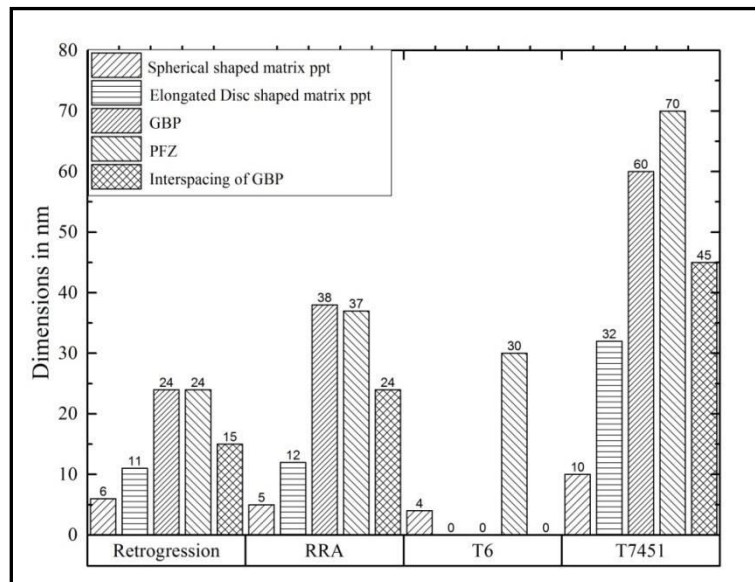
Fig. 4.15 Precipitate size distribution in different tempered alloys (data extracted from Figures 4.7, 4.8, 4.9 and 4.13)

4.3.6 Grain boundary microstructure of the RRA treated alloy

The precipitates on the grain boundaries get coarsened as the retrogression time is increased. The GBP's are coarsened with increase in reversion time as shown in Fig. 4.17. The average size of the GBP's vary in the range 36-59 nm for the retrogression performed for 10-60 min respectively (Fig. 4.16 a). The average size of PFZ in the RRA treated samples vary over the range 37-51 nm (Fig. 4.16 b) for retrogression duration of 10-60 min respectively.
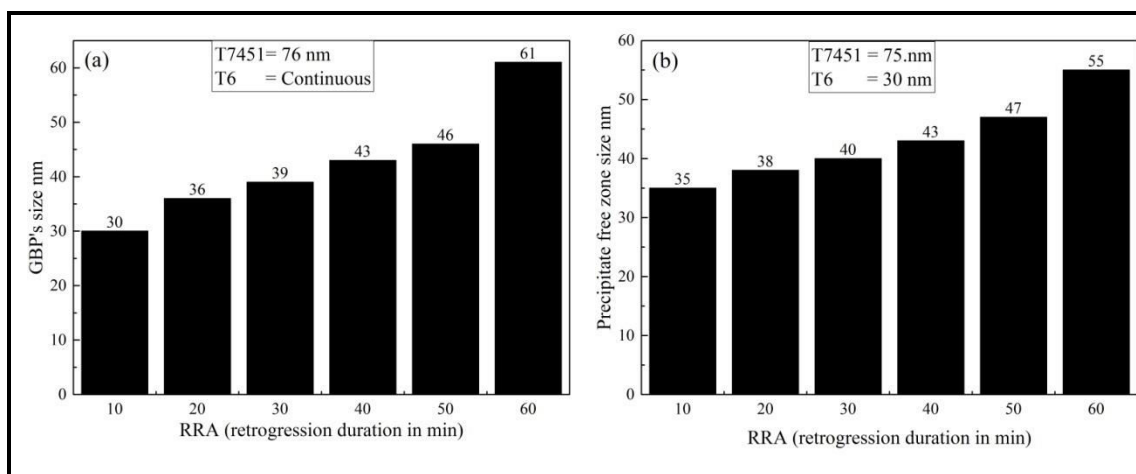
Fig. 4.16 Column plot indicating variation of the grain boundary characteristics with retrogression time; a) GBP's size, b) PFZ size (data extracted from Figure 4.17)
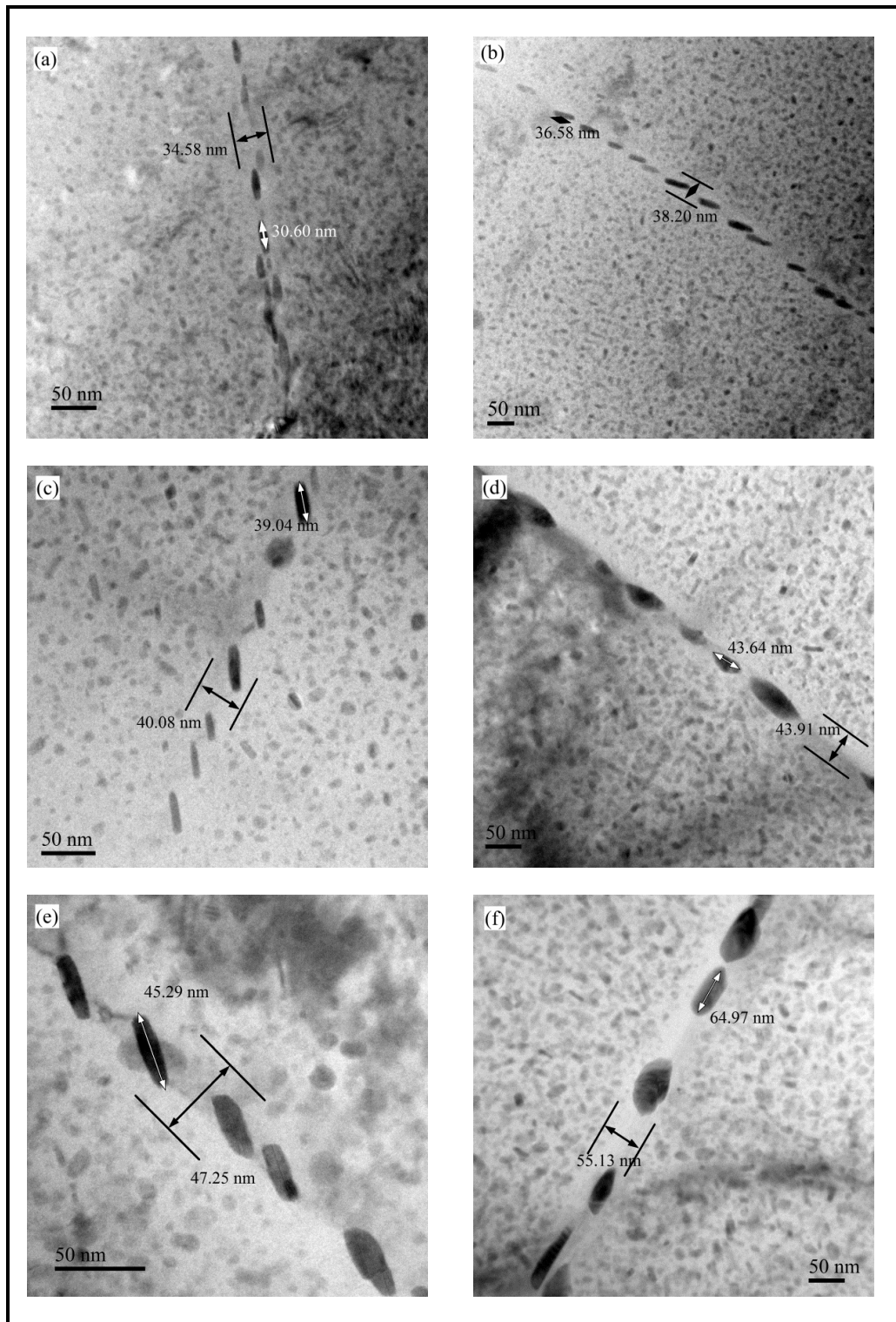
Fig. 4.17 Bright-field TEM micrographs of the alloy showing grain boundary region at different retrogression time duration; a) 10, b) 20, c) 30, d) 40, e) 50, f) 60 minutes

4.4 Differential Scanning Calorimetry

The differential scanning calorimetry is carried out on the different heat treated alloy samples and is presented in Fig. 4.18. For the RRA treated alloy samples in (Fig. 4.18 b) the precipitate evolution and dissolution temperatures could be clearly observed. The observed peak at 192.5 ˚C is an endothermic peak which corresponds to η' dissolution during high temperature reversion treatment (Xia et al. 2016; YANG et al. 2016). Further, the exothermic peak observed at 237.5 ˚C corresponds to the transformation of undissolved precipitates into stable η precipitates. The DSC scan performed on T6 and T7451 treated alloys are also presented in Fig. 4.18 (a, c).
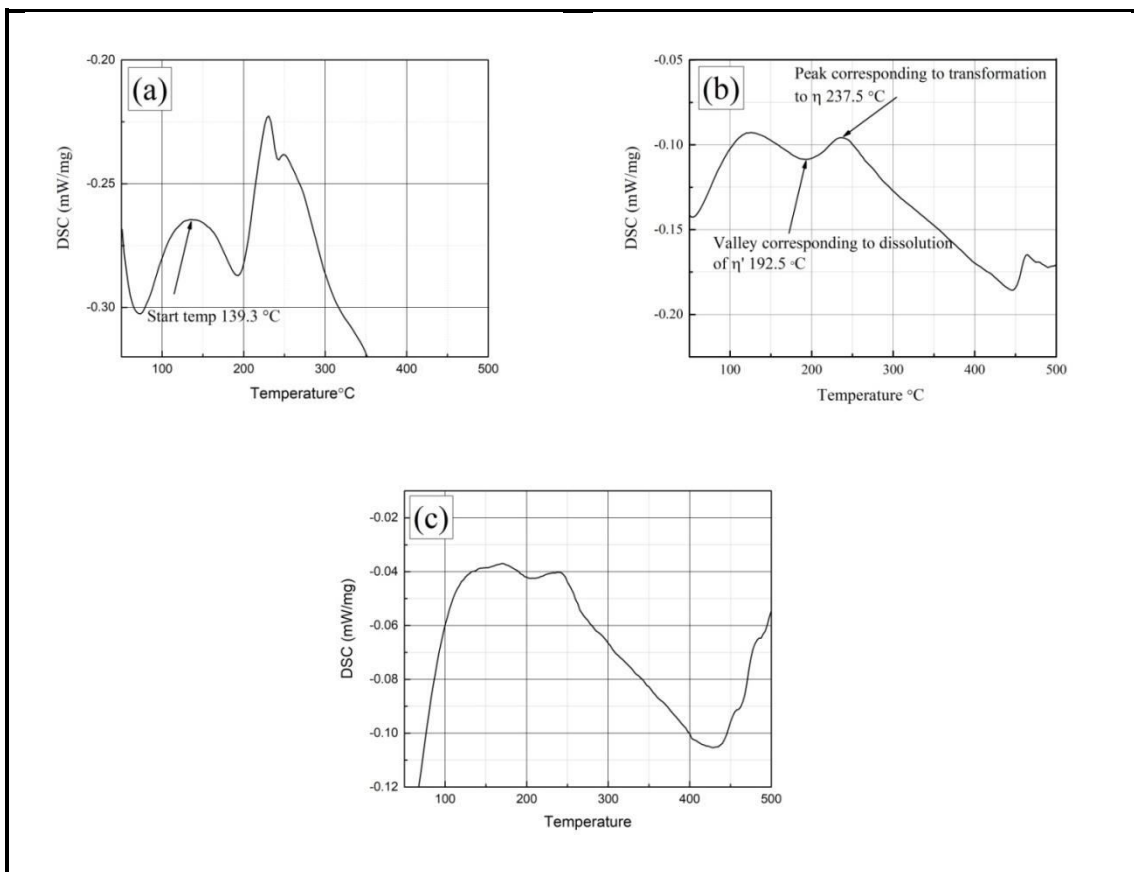
Fig. 4.18 Differential scanning calorimetric analysis of the alloys; a) T6, b) RRA, c) T7451

4.5 Effect of Heat Treatment on Hardness

4.5.1 Peak-aging

Figure 4.19 shows the age hardening behavior of 7010 alloy when solutionized and aged at 120 °C for duration of 0.5 h to 110 h. A single stage aging behavior is observed and the alloy reaches a maximum hardness of 203 HV at 24 h (peak-aging). With further aging above 24 h at the same temperature the hardness profile drops which is due to the coarsening of the precipitates upon prolonged aging. Therefore, for the current study, the heat treatment at 120 ˚C for 24 h is considered to be optimum peak-aging parameters for the alloy.
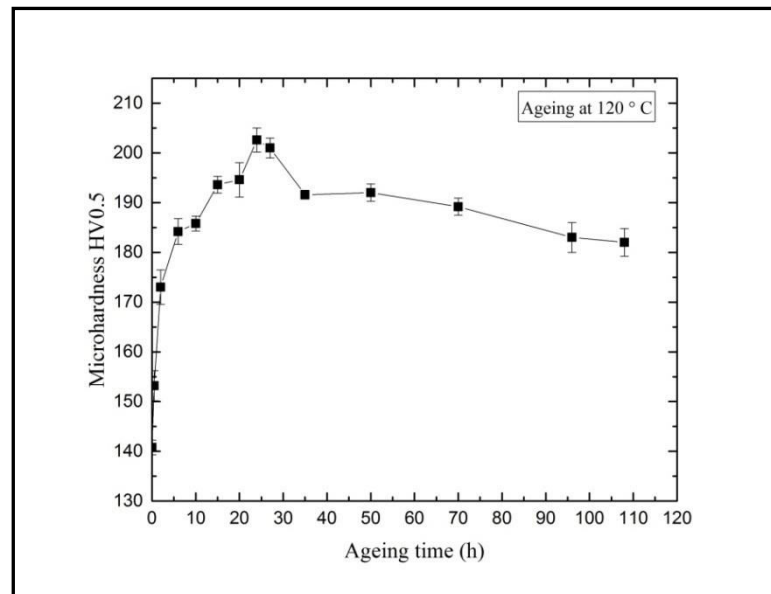
Fig. 4.19 Variation of the hardness with aging time for the alloy at peak-aging temperature

4.5.2 Influence of retrogression and re-aging on the hardness of alloy

Figure 4.20 presents the hardness variation of RRA treated alloy with varied retrogression temperature and duration. Reversion is performed at different temperatures ranging from 180 / 200 / 220 °C for varying retrogression time in the range of 10 to 50 min. The time and temperature of retrogression are optimized based on the results of hardness measured on the alloy samples after performing RRA treatment. The results reveal that by performing retrogression at the lower range of

temperature i.e., at 180 °C, the microstructure does not impart considerable hardness to the alloy even after re-aging to T6 condition. This is attributed to the insufficient dissolution of the matrix precipitates during the reversion stage and hence peak hardness is not achieved even after re-aging the alloy to T6 condition. Retrogression performed at a higher range of temperature at around 220 °C also did not yield peak hardness. This is attributed to the higher amount of dissolution in matrix precipitates during reversion heat treatment. From this plot, it is concluded that by performing a retrogression at an intermediate temperature, i.e., at 200 °C for 10–20 minutes would evolve required microstructure for retaining the strength equivalent to that of the peak-aged sample.
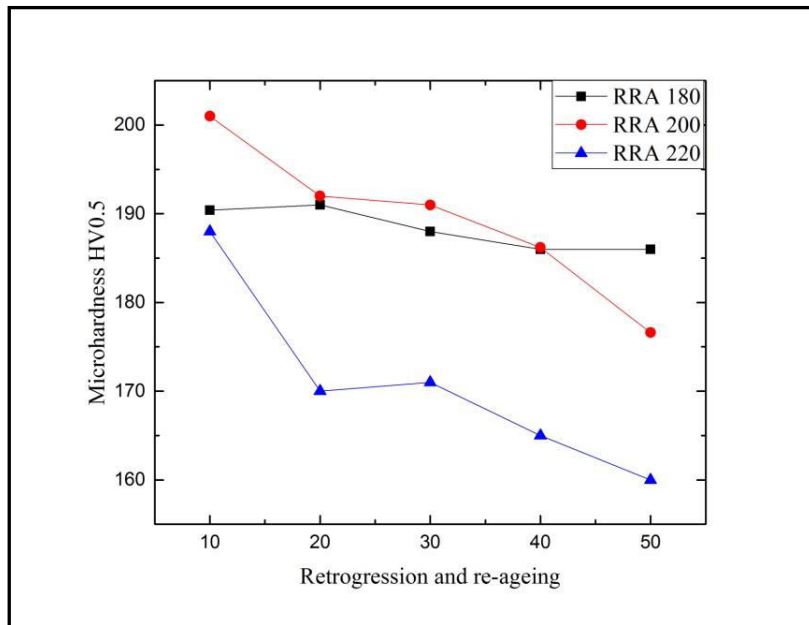
Fig. 4.20 Variation in hardness with change in the retrogression temperature and duration

4.5.3 Hardness of retrogression and re-aged alloy compared with the T6 alloy

Figure 4.21 compares the hardness of alloy treated in T6, retrogression (200 °C) and the RRA conditions. It infers that the RRA heat treated sample would result in better strength properties than that of the T6 treated sample when retrogression is carried for 20 min. There exists an initial drop in hardness value during the retrogression stage which corresponds to the dissolution of GP zones (Danh et al. 1983). This drop in hardness is recovered by the re-precipitation and growth of the η' precipitates during

the re-aging step. If retrogression is continued above 20 min, the re-aged alloy results with a further drop in hardness as a result of coarsening of the η' precipitates. The re-aging step after retrogression stage would enrich the matrix by nucleation and growth of newly formed fine scale precipitates that helps in regaining the strength of the alloy.
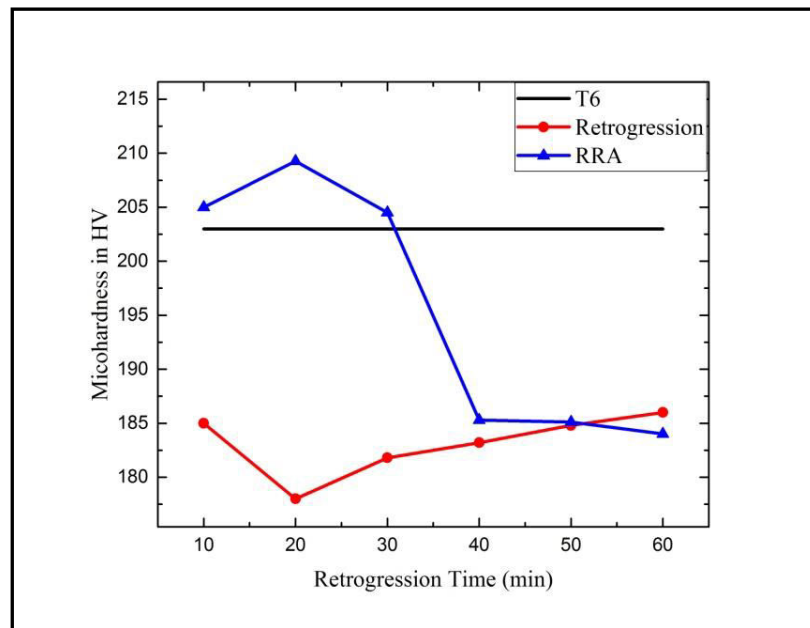
Fig. 4.21 Hardness of the alloy as a function of retrogression time at different tempers

4.6 Effect of Heat treatment on the Tensile Strength of the Alloy

Retrogression is performed at 200 ° C for different time intervals ranging 05-60 min. The tensile properties, such as yield strength, ultimate tensile strength and ductility of the alloy with retrogression carried for different duration, are shown in Fig. 4.22. The trend observed in the variation of the tensile strength of RRA treated alloy is similar to that of the hardness variation observed. By performing RRA treatment (retrogression for 5 min) a maximum tensile strength of 609 MPa is obtained which is higher than that of the typical T6 treated (581 MPa) sample. This behavior is similar to that reported in the literature (Reda et al. 2008). The retrogression time of 20 minutes at 200 °C, has resulted in a tensile strength of 586 MPa. The strength obtained by RRA (reversion for 20 min) is equivalent to that of the T6 treated alloy (581 MPa). Similar behavior is observed for the yield strength of the RRA treated

61

sample. The yield strength of the RRA treated sample stood at 514 MPa which is 5.4 % higher than that of the T6 treated alloy. The % elongation (plastic strain) to failure in T6, T7451 and RRA treated samples stood at 14.4, 11.4 and 11.3 respectively. Ductility of the RRA treated alloy remained close to that of the T7451 treated condition but is lower than the T6 alloy. This could be correlated to the presence of different morphologies of the precipitates in the matrix. There exist small scale spherical shaped precipitates and elongated disc shaped precipitates in the matrix which are shown in the microstructural analysis carried out with the help of TEM (section 4.3.5). Though the UTS and YS are observed to be highest for 5 min reversion time, it appears from the grain boundary microstructure (Fig. 4.17a) that the precipitates at the grain boundaries are still not completely disintegrated. Hence it is beneficial to have disintegrated grain boundaries to gain better SCC resistance. Therefore we considered 20 min of retrogression as optimized parameter that provided required microstructure without losing the T6 strength equivalent.
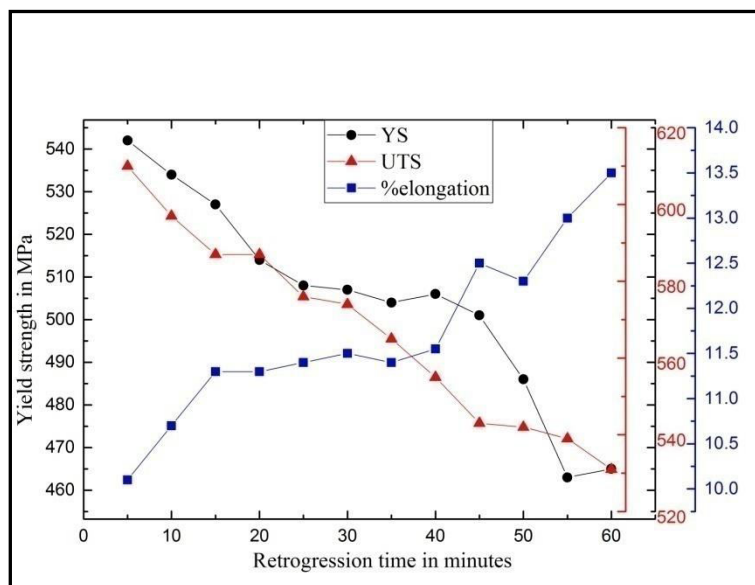
Fig. 4.22 Variation in yield strength, ultimate strength and elongation to failure of the RRA treated alloy with retrogression temperature

4.7 Stress-Strain Curve for the Alloy in Different Aging Conditions

The stress-strain curve of the as-quenched, T6, T7451 and RRA treated samples are presented in Fig. 4.23. Solutionized and as-quenched alloys exhibit higher ductility, of being more than 25 % strain (total elongation before failure). When compared with

the T6 treated condition, RRA treated sample exhibits lower ductility. T7451 treated condition exhibits better ductility than the RRA, but with the loss of strength. Figure 4.24 compares the yield strength, UTS and % elongation to failure exhibited by the alloy in different tempered conditions.
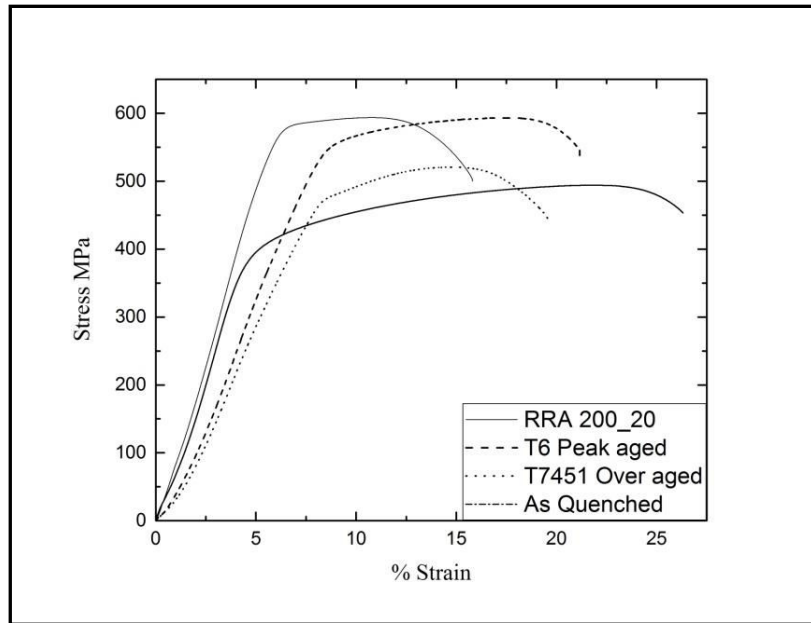
Fig. 4.23 Stress-Strain behavior in different alloy conditions
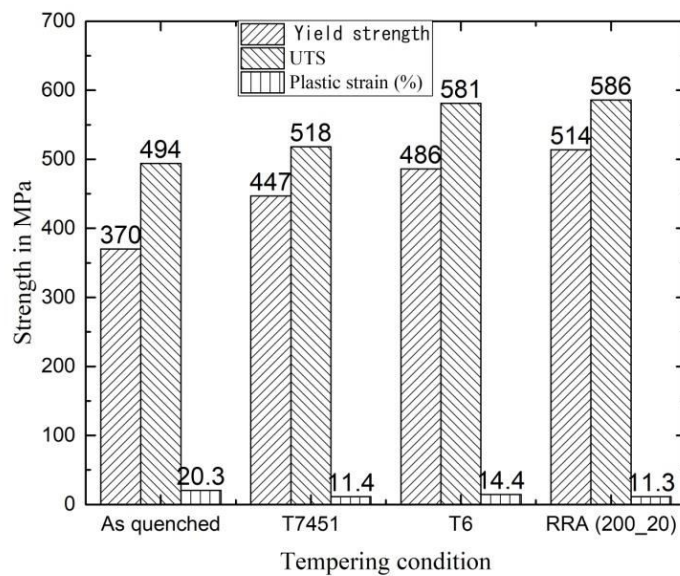
Fig. 4.24 Histogram representing YS, UTS, and plastic strain to fracture of the alloy at different tempers

4.8 Fracture Toughness of the Alloy

Figure 4.25 shows fracture toughness of the alloy in different tempered conditions. The RRA treated alloy exhibits fracture toughness of about 41 MPa√m which is very close and a unit value higher than T7451 treated alloy (40 MPa√m). The T6 treated alloy possesses a fracture toughness of 42 MPa√m. . For each condition 3 tests were performed and the average value was reported with standard deviation of 2, 1.5 and 2 MPa√m for T7451, RRA and T6 conditions respectively
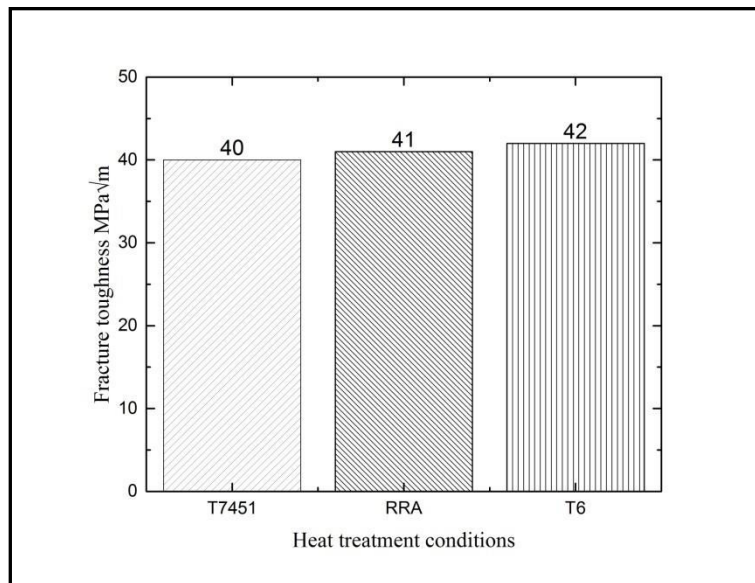
Fig. 4.25 Fracture toughness of the alloy under different aging conditions

4.9 Brief Summary of Microstructural and Mechanical characterization

This chapter highlighted the alloy's microstructure modifications after performing various heat treatments. The optical microscope characterized the grains and grain growth exhibited, TEM micrographs mainly identified the precipitates characteristics on grains and grain boundaries and also differentiated the nature of precipitates present in T6 and RRA conditions. Later the basic mechanical tests such as hardness, tensile and fracture toughness tests highlight the influence of various treatments on the bulk properties of the alloy.

CHAPTER 5

FATIGUE CRACK GROWTH BEHAVIOR

5.1 Fatigue Crack Growth Rate Tests Under Constant Amplitude Loading

5.1.1 Influence of heat treatment on fatigue crack growth behavior

The Fatigue crack growth rate behavior (i.e., da/dN-ΔK curve) for both T6 and RRA treated 7010 aluminum alloys are determined at various stress ratios (R = 0.1 to 0.7), and presented in Fig. 5.1(a, b). For the sake of clarity, the comparison plots of the FCGR curves for both T6 and RRA treated alloys at each specific stress ratio are separately depicted in Fig. 5.2 (a-d). In general, increasing the stress ratio is observed to increase the fatigue crack growth rate in both T6 and RRA treated alloys (Fig. 5.1 a, b). The crack growth rate is observed to be reduced for RRA treated alloy particularly in the near-threshold regime of the crack growth curve, also for the initial portion of Paris' regime (Fig. 5.2 a-d). However, further increase in ΔK, above the mid Paris' regime, the crack growth rate of RRA alloy becomes faster and the curve merges with that of the T6 treated alloy. Generally, this observation is seen for all the stress ratio tests investigated.
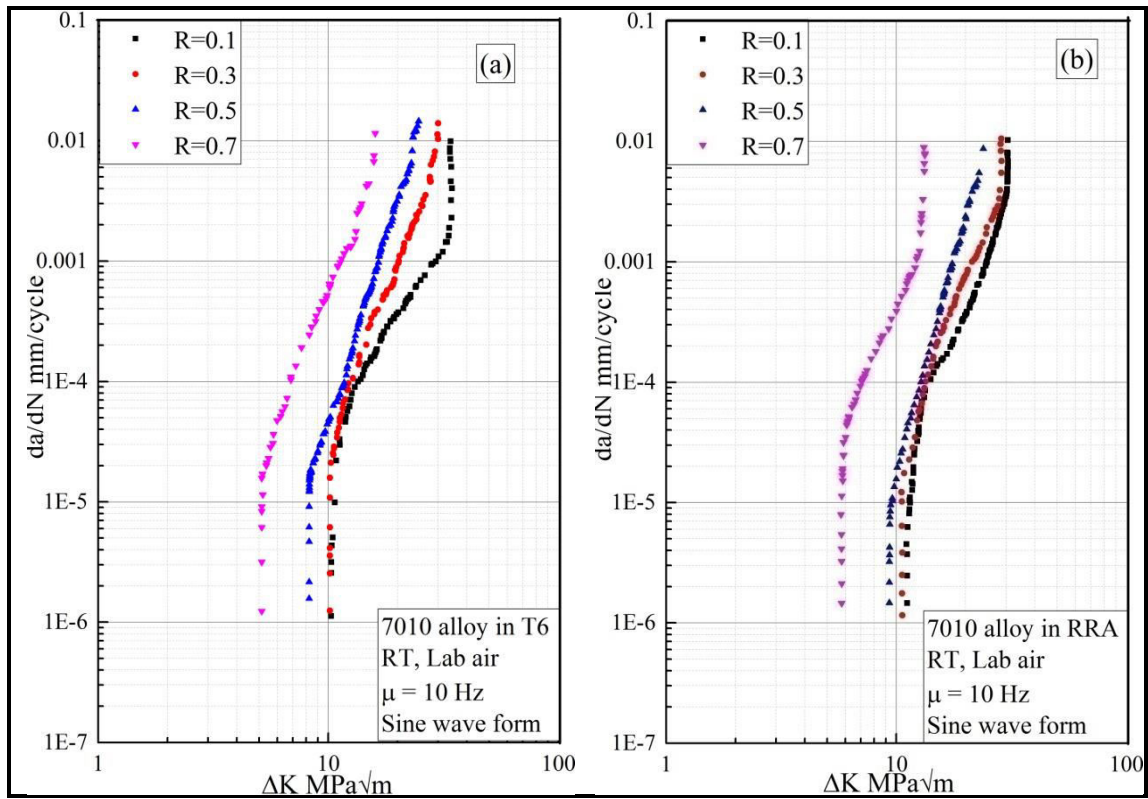
Fig. 5.1 FCGR curves determined at various stress ratios on different tempered aluminum alloys; a) T6, b) RRA
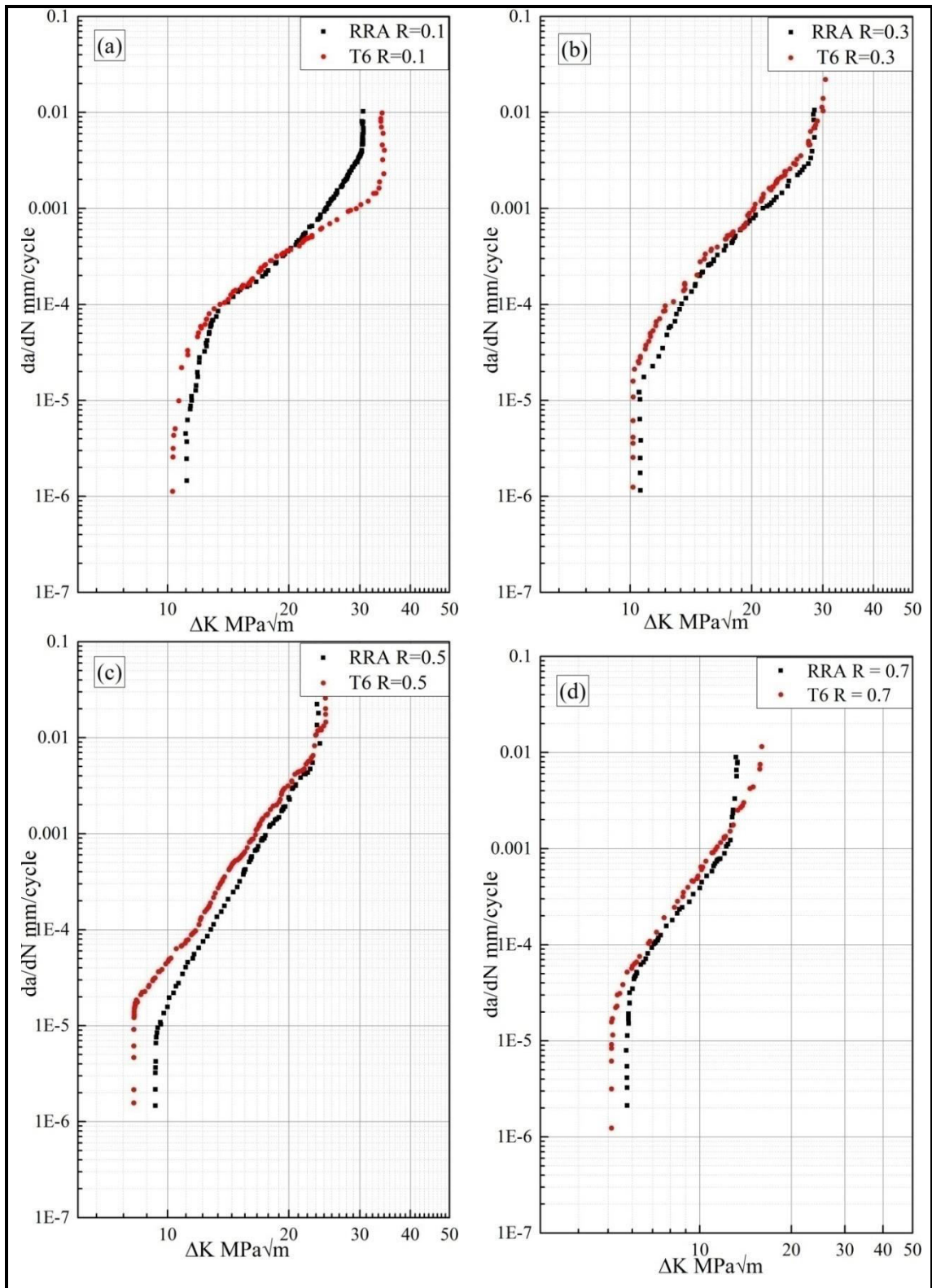
Fig. 5.2 Comparison of FCGR curves of the T6 and the RRA treated alloys at different stress ratios; a) R=0.1, b) R=0.3, c) R=0.5, d) R=0.7

The FCGR data in the Paris' regime is fitted to Paris' law (Al-Rubaie et al. 2005; Paris and Erdogan 1963) as per equation 1.

$$da/dN = C(\Delta K)^m \quad \text{----------- (1)}$$

Here, C and m are the material constants determined from FCGR curves. The values of these material constants are determined at all the stress ratio tests for materials subjected to T6 and RRA treatments. They are presented in Table 5.1. The fatigue crack growth rate, da/dN in the near-threshold regime corresponding to $\Delta K = 12$ MPa√m at different stress ratio tests, are listed in Table 5.1. The results of the FCGR tests indicate that the RRA treated alloy exhibits nearly 2-3 times reduction in the fatigue crack growth rate when compared to that of the T6 treated alloy, particularly in the near-threshold regime.

Table 5.1 Paris' constants C, m and FCGR at near-threshold regime for the T6 and RRA treated alloy

Stress ratio R	Alloy condition	C	m	$da/dN = C(\Delta K)^m$ mm/cycle
				$\Delta K = 12$ MPa√m
0.1	RRA	4.51×10^{-11}	5.36	2.78×10^{-5}
	T6	2.56×10^{-9}	4.0	5.90×10^{-5}
0.3	RRA	6.21×10^{-10}	4.71	3.48×10^{-5}
	T6	1.28×10^{-9}	4.56	8.48×10^{-5}
0.5	RRA	3.99×10^{-12}	6.7	6.45×10^{-5}
	T6	4.02×10^{-10}	5.05	1.26×10^{-4}
0.7	RRA	3.68×10^{-8}	4.05	8.91×10^{-4}
	T6	3.27×10^{-8}	4.22	1.2×10^{-3}

Since the difference in FCGR behavior between T6 and RRA treated alloys appear to be more pronounced in the near-threshold regime, the fatigue crack growth rates of aluminum alloy in T6 and RRA conditions in the near-threshold regime is separately depicted in Fig. 5.3. The data indicates that in both T6 and RRA treated aluminum alloys, increasing the stress ratio observed to increase the crack growth rate and decreases the threshold stress intensity factor ΔK_{th} (SIF). Further, for any given stress ratio, the crack growth rate is lower and ΔK_{th} is higher for the RRA treated alloy

when compared to the T6 treated alloy. This behavior is observed for the tests performed at all the stress ratio ranging from 0.1-0.7. The magnitude of increase in ΔK_{th} is by about 0.5-1.1 MPa√m at different stress ratio tests as shown in Table 5.2.
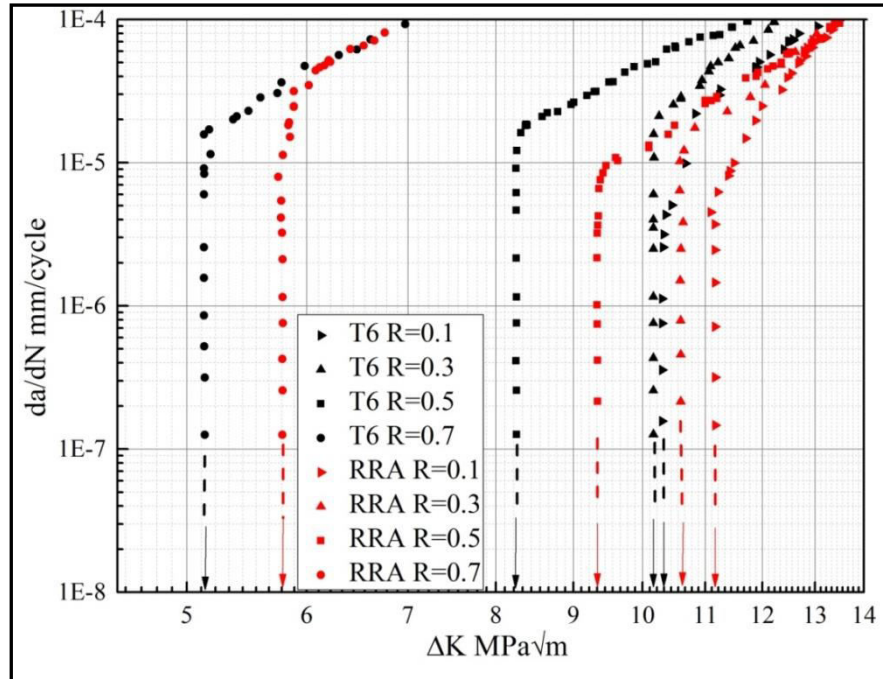
Fig. 5.3 FCGR curves at near-threshold regime for the T6 and the RRA treated alloys at various stress ratios

Table 5.2 Threshold stress intensity factor range (ΔK_{th}) determined at various stress ratio (R) for T6 and RRA treated alloys

Stress ratio R	Threshold stress intensity factor range ΔK_{th} (MPa√m)	
	T6	RRA
0.1	10.30	11.16
0.3	10.16	10.59
0.5	8.25	9.33
0.7	5.13	5.78

69

5.2 Crack Closure Levels from Compliance Curves

The load-CMOD (Crack Mouth Opening Displacement) data recorded during the FCGR tests are analyzed to determine the crack closure levels in alloy subjected to both heat treatments. Typical load-CMOD data is obtained at various stress ratios for both T6 and RRA treated aluminum alloys. They are shown in Fig. 5.4 (a-d). The crack closure load was obtained by percentage compliance offset method as per ASTM specifications. The unloading part of the load-CMOD data was used to determine 4% offset to estimate crack closure load. The crack closure level, γ is defined as

$$\gamma = (P_{cl} - P_{min}) / (P_{max} - P_{min}) \text{ ------------ (2)}$$

Here,

P_{cl} is the crack closure load (i.e., the location in the Load-CMOD curve where stiffness change occurs)

P_{min} is the minimum load in the fatigue cycle

P_{max} is the maximum load in the fatigue cycle

γ is the crack closure value

The crack closure value, γ determined for both the alloy materials at all the stress ratios is shown in Table 5.3. It could be seen from Fig. 5.4 and Table 5.3 that for each tempered condition, at low stress ratios, i.e., at R = 0.1 and 0.3, increasing the stress ratio decreases crack closure level. The crack closure was absent at high stress ratios, at R = 0.5 and 0.7 for both the alloy materials. It is also noted that at low stress ratios, at R = 0.1 and 0.3, the closure level is higher in the RRA treated alloy when compared to the T6 treated alloy. The respective crack closure load is measured at different ΔK levels and is listed in the table presented in the inset of Fig. 5.4 (a-d). The measured crack closure level indicates (Fig. 5.5) that with the increase in ΔK, the closure level γ decreases up to a stress ratio of 0.3. Thereafter for R=0.5, 0.7 crack closure level remains same for any ΔK.
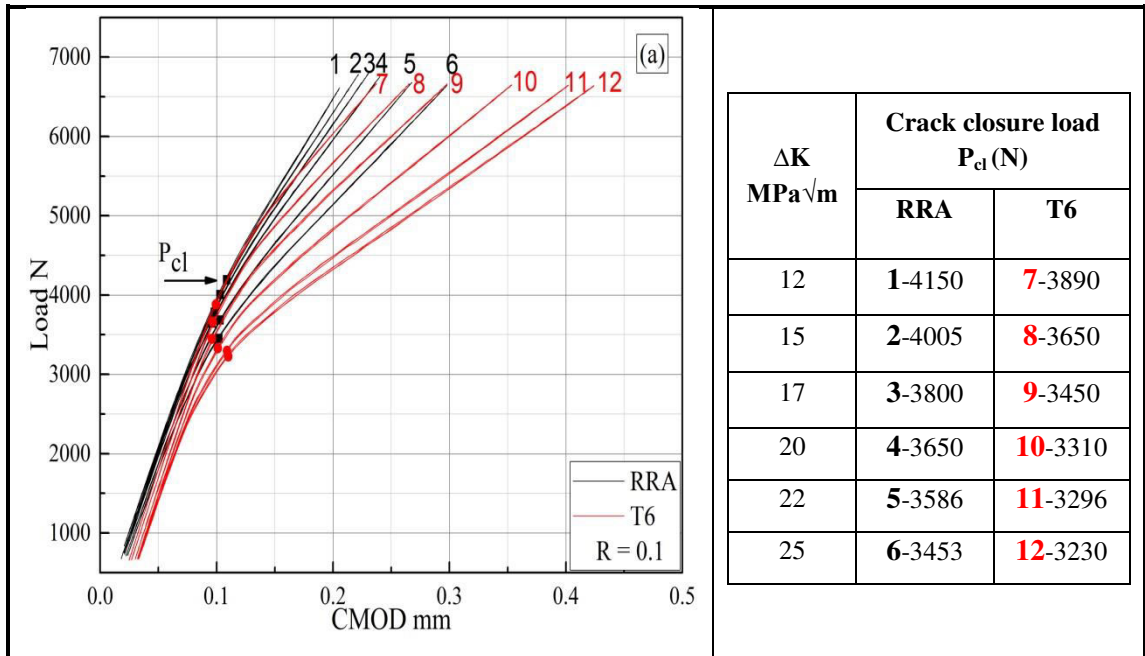
Fig. 5.4 Load-CMOD data and crack closure load determined for T6 and RRA alloys.
a) R=0.1
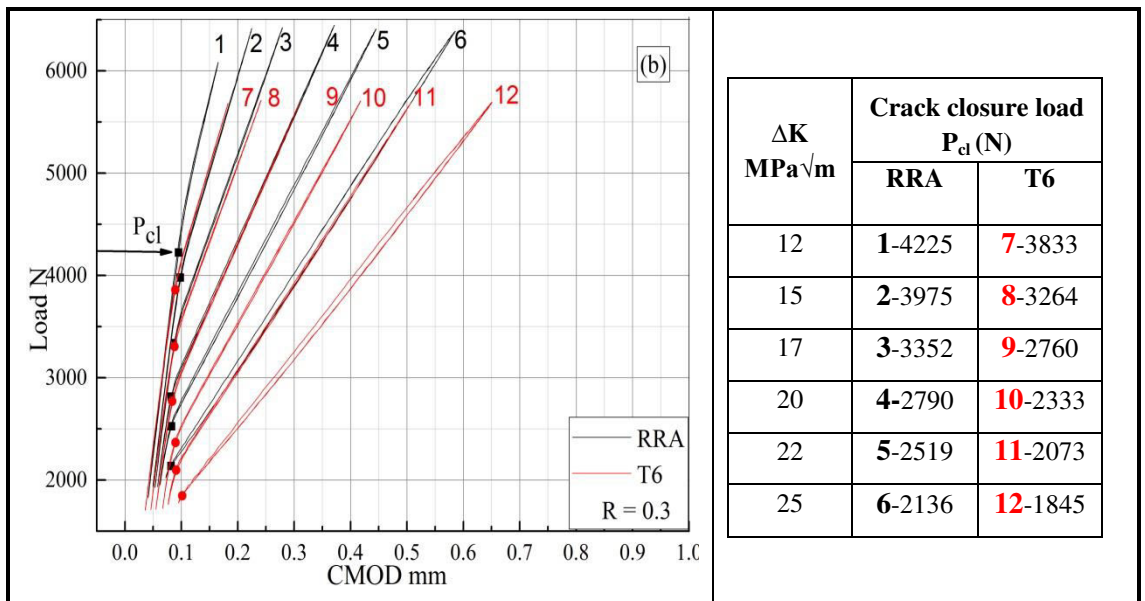
Fig. 5.4 Load-CMOD data and crack closure load determined for T6 and RRA alloys.
b) R=0.3
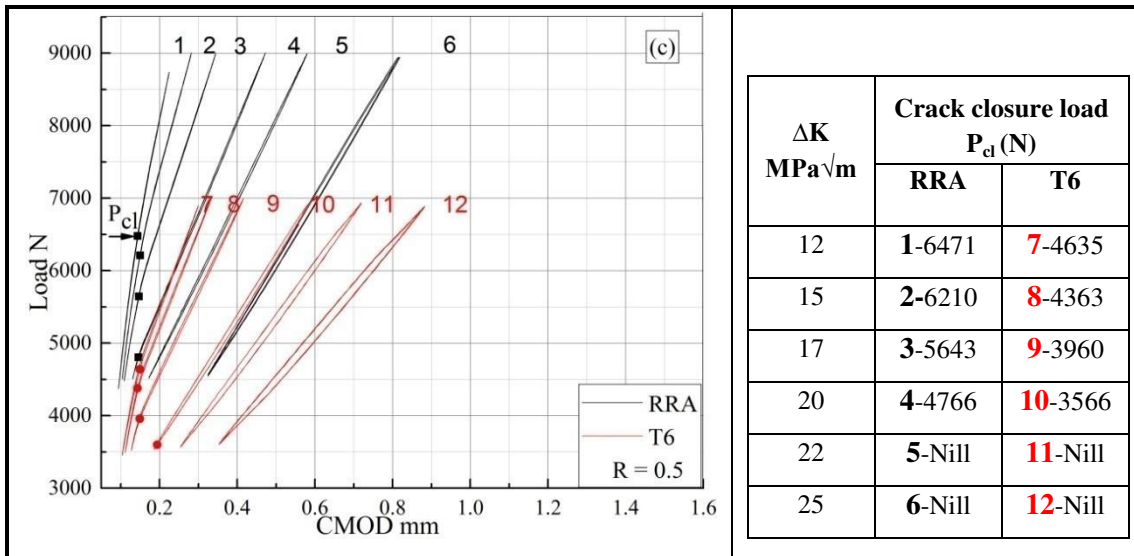
71

ΔK MPa√m	Crack closure load P_{cl} (N)	
	RRA	T6
12	**1**-6471	**7**-4635
15	**2**-6210	**8**-4363
17	**3**-5643	**9**-3960
20	**4**-4766	**10**-3566
22	**5**-Nill	**11**-Nill
25	**6**-Nill	**12**-Nill

Fig. 5.4 Load-CMOD data and crack closure load determined for T6 and RRA alloys. c) R=0.5

ΔK MPa√m	Crack closure load P_{cl} (N)	
	RRA	T6
10	**1**-Nill	**7**- Nill
12	**2**- Nill	**8**- Nill
15	**3**- Nill	**9**- Nill
17	**4**- Nill	**10**- Nill
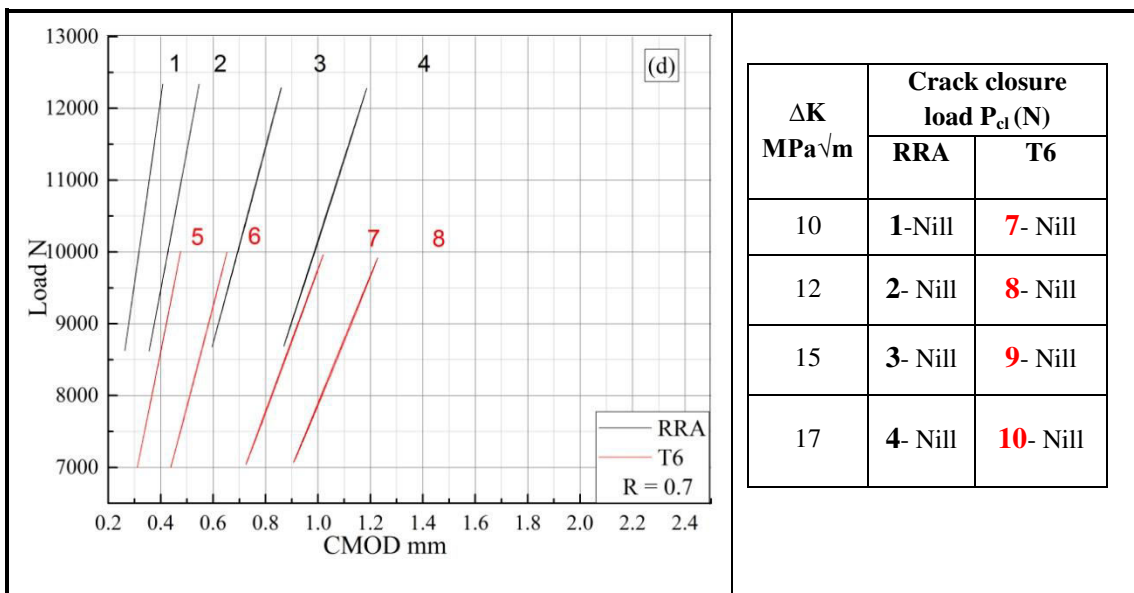
Fig. 5.4 Load-CMOD data and crack closure load determined for T6 and RRA alloys. d) R=0.7

Table 5.3 Crack closure levels determined experimentally for the aluminum alloys

Stress ratio	Crack closure level, γ	
R	T6	RRA
0.1	0.37	0.44
0.3	0.09	0.12
0.5	0.00	0.00
0.7	0.00	0.00
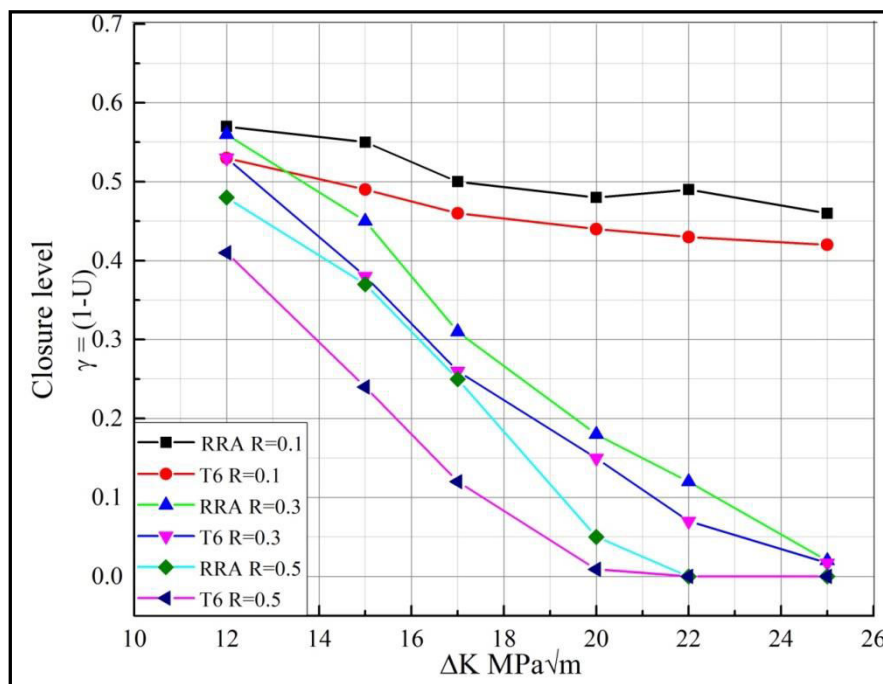
Fig. 5.5 Crack closure level variation with increase in ΔK for differently treated alloys

Figure 5.6 highlights the change in FCGR curve after accounting the crack closure loads at different stress ratios. The crack growth rate, da/dN is plotted against ΔK_{eff} by considering the crack closure level as measured in Table 5.3. A shift in the FCGR curves for both T6 and RRA alloys at stress ratio, 0.1 and 0.3 is evident. The curves corresponding to stress ratio 0.5 and 0.7 remains the same as there is no crack closure evident.
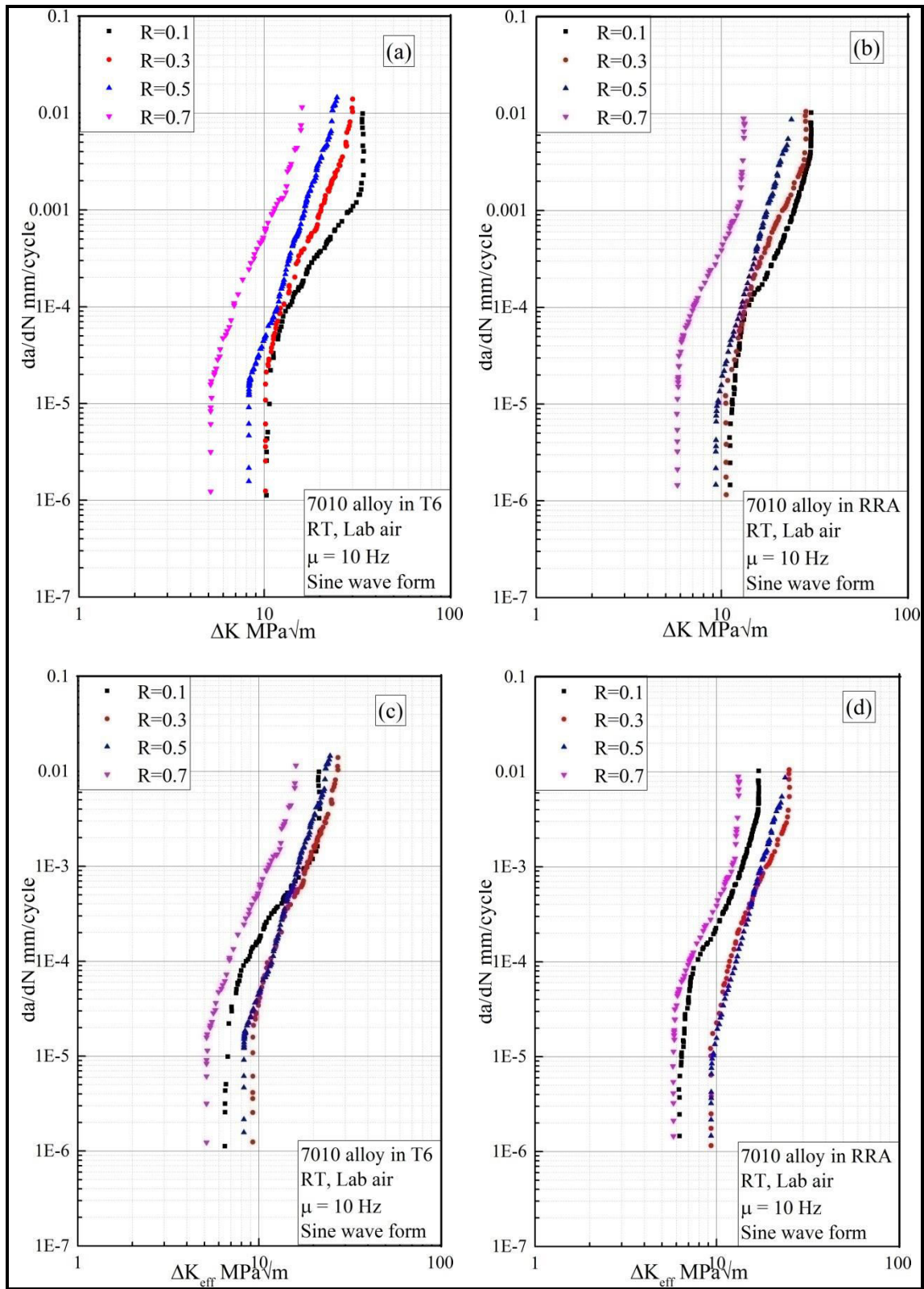
Fig. 5.6 FCGR curves compared by considering the crack closure effect; a, b) without crack closure, c, d) with crack closure

The FCGR tests performed on T7451 (as received), T6 and RRA treated alloys at R=0.1 are compared in Fig. 5.7 (a). The crack growth rate vs applied stress intensity range ΔK is plotted. Comparing the crack growth rate behavior of all three heat treated samples it could be seen that there is a shift in the value of the threshold stress intensity factor range (ΔK_{th}) (Fig. 5.7 b) for both RRA and T6 treated alloys. The ΔK_{th} observed for T7451, T6 and RRA are 5.77, 10.3 and 11.16 MPa√m respectively. The crack growth rate difference gets narrowed down and falls into a single band in the Paris' regime, for both T6 and RRA treated samples. The dynamic fracture toughness (K_{max}) observed at the failure is 29.7, 34 and 30.5 MPa√m, respectively for T7451, T6 and RRA treated samples.
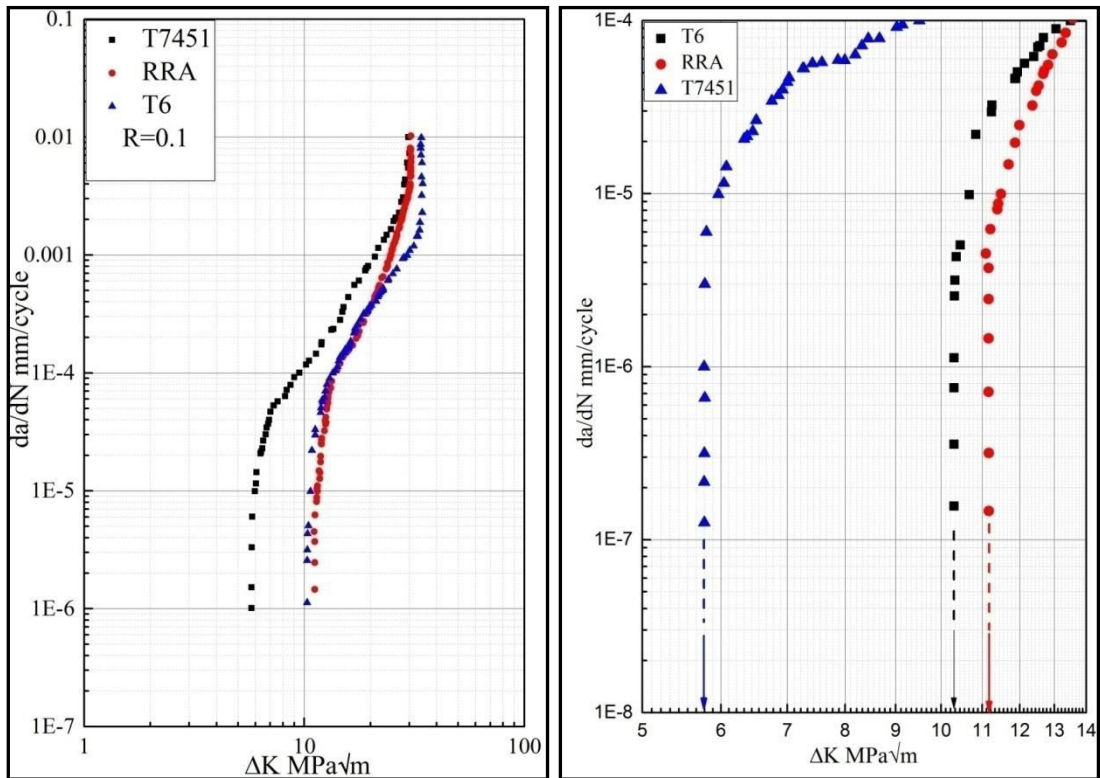
Fig. 5.7 a) FCGR curves of T7451, T6 and RRA treated alloys at stress ratio R=0.1, b) Near-threshold crack growth behavior of the alloy in T7451 condition compared with RRA and T6 alloy

5.3 Experimental Spectrum Fatigue Crack Growth Behavior

The experimentally determined fatigue crack growth behavior of the aluminum alloy subjected to T6 and RRA heat treated conditions, tested under standard mini-FALSTAFF

spectrum load sequence with reference load of 15 kN is shown in Fig 5.8. The crack growth rate is lower and the total fatigue crack propagation life is higher in RRA treated alloy than that observed in the T6 treated alloy. The total number of spectrum load blocks required to failure is about 59 blocks for the RRA treated alloy and it is about 48 blocks for the T6 alloy, as shown in Fig. 5.9. Thus the RRA heat treatment appears to impart about 22 % enhancement in crack propagation life under aircraft service simulating loads compared to the T6 treated alloy.
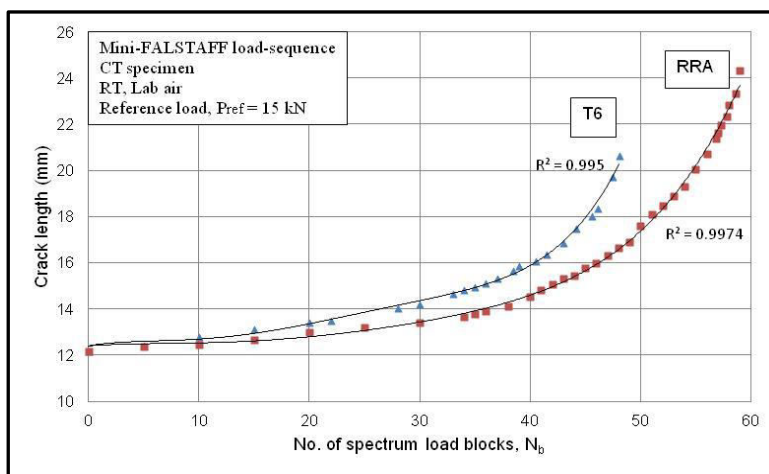
Fig. 5.8 Experimental fatigue crack growth behavior of the alloy under mini-FALSTAFF load sequence
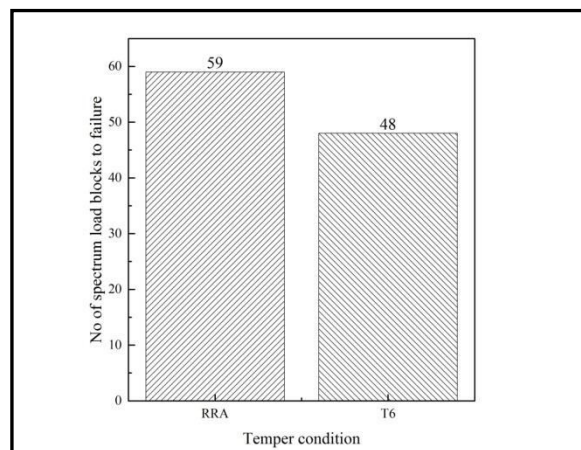
Fig. 5.9 Number of service load blocks required to failure in different tempered conditions

5.4 Prediction of Spectrum Fatigue Crack Growth Behavior

The fatigue crack growth behavior of T6 and RRA treated aluminum alloys under the mini-FALSTAFF load sequence is predicted following the procedure shown in Fig. 5.10.

```
┌─────────────────────────────────────────────────────────────────────────┐
│                                                                           │
│   ┌─────────────────────┐              ┌─────────────────────┐            │
│   │  Spectrum load       │              │  Constant amplitude  │            │
│   │  sequence            │              │  (CA) FCGR data at    │            │
│   │  (Mini-FALSTAFF)     │              │  various R ratios     │            │
│   └──────────┬──────────┘              └──────────┬──────────┘            │
│              │                                    │                       │
│   ┌──────────▼──────────┐              ┌──────────▼──────────┐            │
│   │  Rainflow cycle      │              │  Derive fatigue crack │            │
│   │  counting            │              │  growth law from the  │            │
│   │                      │              │  CA FCGR data         │            │
│   └──────────┬──────────┘              └──────────┬──────────┘            │
│   ┌──────────▼──────────┐                         │                       │
│   │      ΔP, R           │                         │                       │
│   └──────────┬──────────┘                         │                       │
│              └──────────────────┬─────────────────┘                       │
│   ┌──────────────────────────────▼──────────────────┐                     │
│   │            For each counted cycle                 │◄─────┐              │
│   └──────────────────────┬───────────────────────────┘      │              │
│   ┌──────────────────────▼──────────────────┐               │              │
│   │  Determine the crack driving force        │               │              │
│   │  from ΔP, R, a                            │               │              │
│   └──────────────────────┬──────────────────┘               │              │
│   ┌──────────────────────▼──────────────────┐               │              │
│   │  Alter the driving force by considering   │               │              │
│   │  load interaction effects if any          │               │              │
│   └──────────────────────┬──────────────────┘               │              │
│   ┌──────────────────────▼──────────────────┐               │              │
│   │  Determine crack extension per cycle      │               │              │
│   │  from crack growth law                    │               │              │
│   └──────────────────────┬──────────────────┘               │              │
│   ┌──────────────────────▼──────────────────┐               │              │
│   │            a = a + Δa                      │──────────────┘              │
│   └──────────────────────┬──────────────────┘                              │
│   ┌──────────────────────▼──────────────────┐                              │
│   │  Determine the crack extension            │                              │
│   │  per load block                           │                              │
│   └───────────────────────────────────────────┘                              │
│                                                                           │
└─────────────────────────────────────────────────────────────────────────┘
```

Fig. 5.10 Flow chart showing general methodology for prediction of fatigue crack growth behavior under a spectrum load sequence

The general methodology followed in the prediction of FCGR behavior under spectrum loads is: (i) the rain flow counting of the fatigue cycles in the spectrum load sequence (ASTM E1049-85 2011), (ii) the determination of crack growth law for the material from its constant amplitude fatigue crack growth data, (iii) consideration of load interaction effects, and finally (iv) the determination of crack extension for each of the load block. Since each of the rain flow counted load cycles will be of different load amplitude and mean stress, it is necessary to interpolate and determine crack extension (Δa) for all these load cycles using a crack growth model. For this purpose, the constant amplitude FCGR curves of these materials at different stress ratios are analyzed to obtain a fatigue crack growth law. It is well known from fracture mechanics concepts that the fatigue crack growth is driven by the stress field ahead of the crack tip (Suresh 1998). The FCGR (da/dN) is considered to be a function of the stress intensity factor range, ΔK. The power law equation known as Paris' equation is shown in equation 1.

The Paris' constants C and m are determined from the FCGR plots. The influence of the mean stress on the crack growth is expressed by the effect of load ratio, R which needs to be considered as well.

5.4.1 A two parameter crack growth law

The Paris' Eq. (1), however, can only be used to denote crack growth data for individual load ratio. Therefore, K^* driving force is used to express as a crack driving force which accounts for different stress ratio (Dinda and Kujawski 2004). The K^* model incorporates crack driving force due to K_{max} and ΔK in a fatigue load cycle. It is represented by following equation.

$$K^* = (K_{max})^{\alpha}(\Delta K^+)^{(1-\alpha)} \text{ ---------------- Eq. (3)}$$

Here K_{max} is the maximum stress intensity factor in a fatigue cycle; ΔK^+ is the positive part of the applied stress intensity factor range. Various empirical models have been proposed, A two parameter crack driving force model is proposed to correlate R ratio effects on FCGR in ten different materials (Kujawski 2001a; Sree and Kujawski 2014). This model incorporates the FCGR dependence on ΔK and K_{max} parameters. The FCGR curves for different R ratio are merged by correlating with K_{max} and ΔK driving force

parameters. This derives a unique model which incorporates the effect of both ΔK and K_{max} on FCGR behavior as defined in the following equation (Sree and Kujawski 2014).

$$\Delta K^* = \Delta K_{app} \left(1 - R_t / 1 - R \right)^{\gamma} \text{--- Eq. (4)}$$

Here, $\gamma = \alpha$ for $R > R_t$ and $\gamma = \beta$ for $R < R_t$.

From the constant amplitude FCGR data shown in Fig. 5.1(a, b), at a given constant crack growth rate, the corresponding ΔK and K_{max} are obtained as shown in Fig. 5.11(a, b). A plot of ΔK vs K_{max} is plotted to find the constants α, β and transition stress ratio R_t (Sree and Kujawski 2014). The intersection of slope lines is considered as a transition stress ratio as depicted in Fig. 5.11(c, d). From Fig. 5.11(c, d) two different slope values (p, q=1/p) were determined and α, β were evaluated to be 0.75 and 0.25 respectively for the alloy 7010. Although the procedure adopted in determining these constants are same (Sree and Kujawski 2014), we observed slight different values compared to earlier reported data. The transition stress ratio is found to be $R_t = 0.25$. The equation 4 is computed by adopting $\gamma = \alpha$ for $R > R_t$, $\gamma = \beta$ for $R < R_t$ to determine ΔK^*.

Using the above mentioned material constants and by using equation 5, the FCGR data in Fig. 5.11 (a, b) are now re plotted to represent as a function of ΔK^*. By this method, the FCGR curves corresponding to different stress ratios are merged into a single narrow band as shown in Fig. 5.12 (a, b).
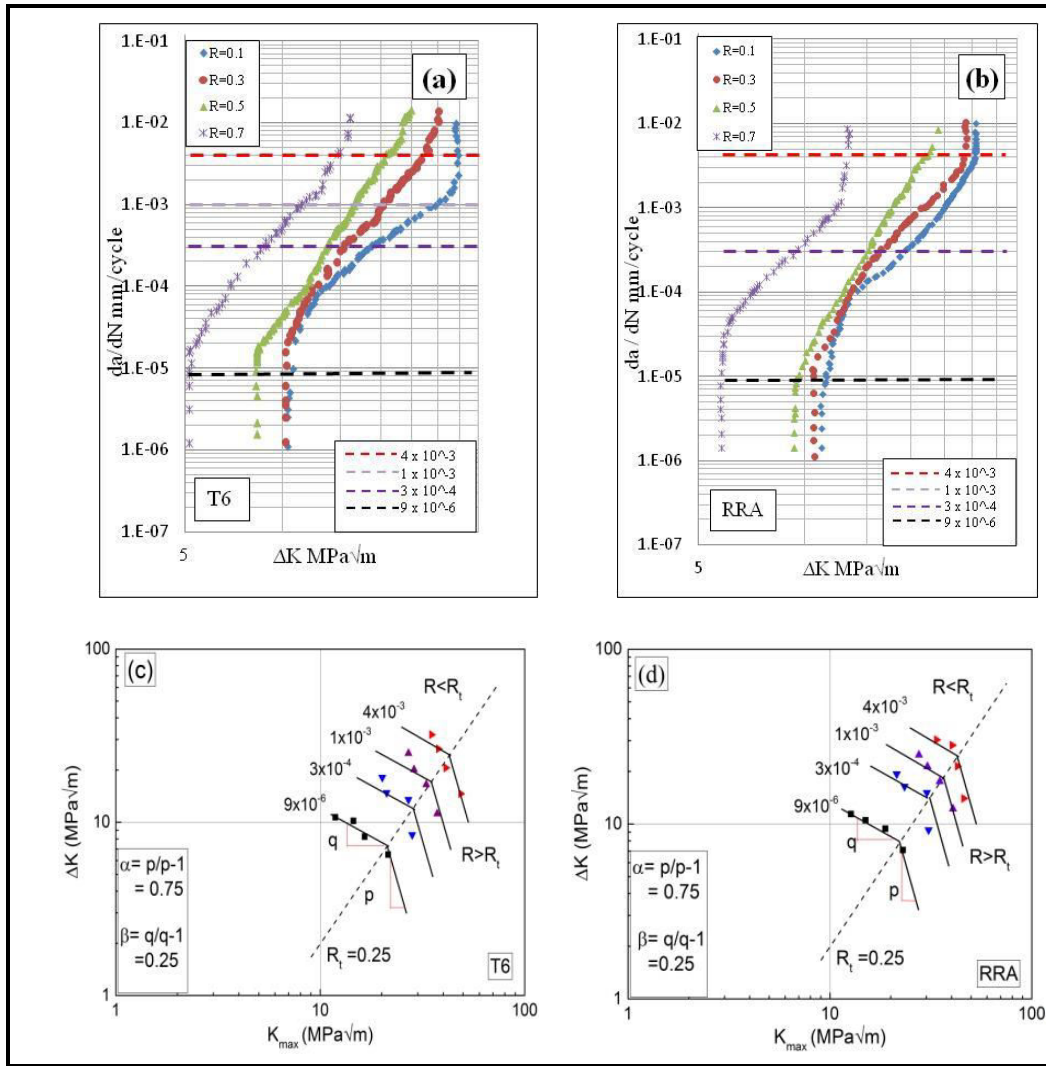
Fig. 5.11 Estimation of constants in equation 4; (a, c) T6 treated alloy (b, d) RRA treated alloy

From Fig. 5.12 (a, b) the material constants in equation 5 are derived as follows, $\Delta K_{th}^{*} = 11.6$ MPam$^{1/2}$ for RRA, 10.8 MPam$^{1/2}$ for T6, C_1=1.75 x 10^{-10} mm/cycle for RRA, 3.5 x 10^{-10} mm/cycle for T6, C_2= 2.45 for RRA, 2.3 for T6, C_3= 31.5 MPam$^{1/2}$ for RRA and 34 MPam$^{1/2}$ for T6 respectively. For fatigue crack growth prediction under service loads, an approximate sigmoidal shape of FCGR data is derived in the form similar to that proposed by Newman (1981). It is given below. The observed FCGR trend is similar to the earlier reports (Manjunatha 2008).

$$\frac{da}{dN} = C_1 (\Delta K^*)^{C_2} \frac{[1-(\Delta K_{th}^{*} / \Delta K^{*})^2]}{[1-(\Delta K^{*} / C_3)^2]} \quad \text{---------- Eq. (5)}$$

80
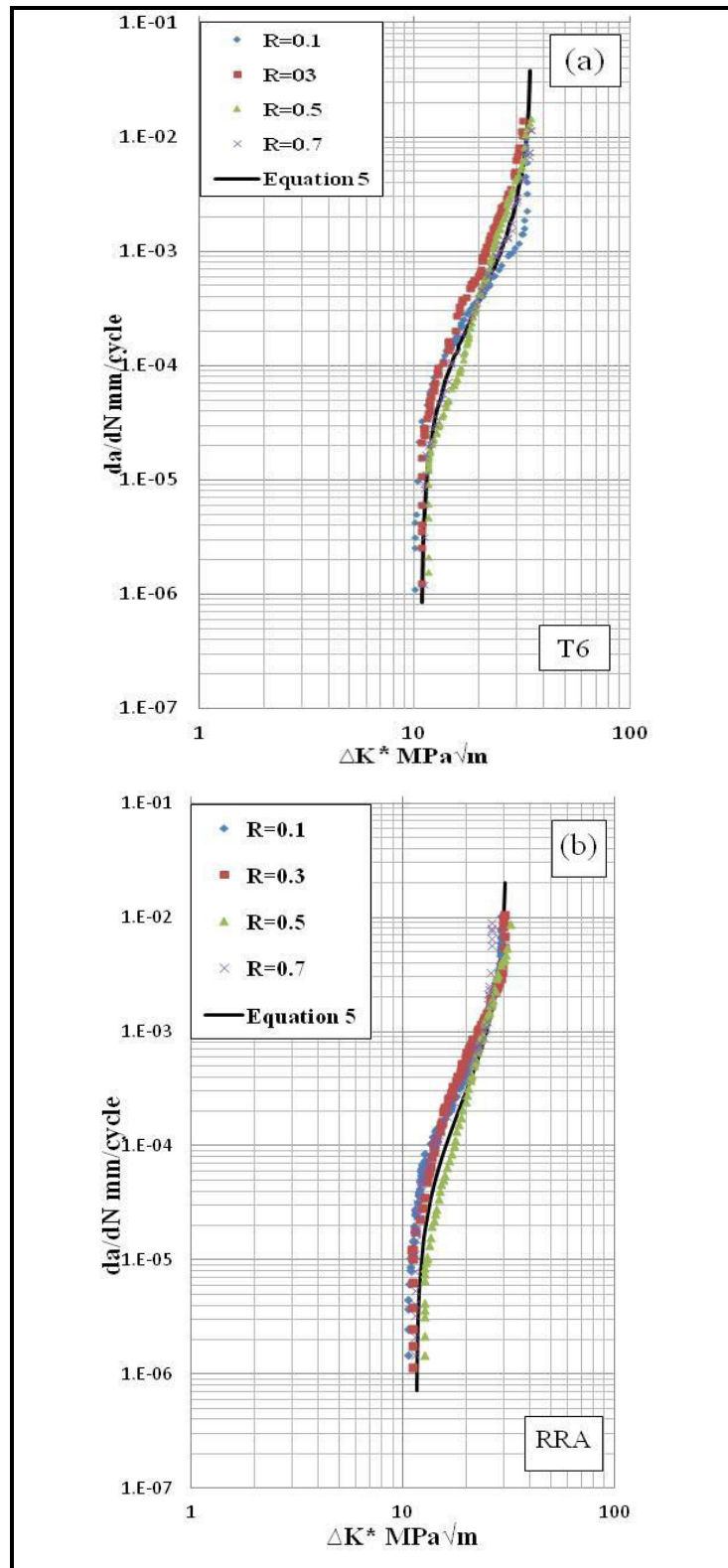
Fig. 5.12 Constant amplitude FCGR curves plotted using ΔK^* driving force; a) T6, b) RRA

5.4.2 Crack closure model

Conventional method for prediction of fatigue crack growth uses a crack closure based model. In this model the driving force for the crack growth is considered to be the effective stress intensity factor range ΔK_{eff}. Here ΔK_{eff} is defined as K_{max} - K_{op} in a fatigue load cycle. Here the K_{max} is the maximum stress intensity and K_{op} is the stress intensity at the crack opening load. The experimentally determined constant amplitude fatigue crack growth data at various stress ratio is merged into a narrow band using the crack closure model, i.e.,

$$\Delta K_{eff} = (1 - \gamma)\Delta K \text{ -------------Eq. (6)}$$

Here γ is the closure level determined at each load ratio level. The crack closure level decreases with increase in ΔK and it also decreases with increase in stress ratio R as shown in Fig. 5.5. No crack closure is observed for R ratio above 0.5 for this alloy. Hence by using a linear relation between the crack closure and ΔK, the resulted FCGR curves are shown in Fig. 5.13. From Fig. 5.13 (a, b) the material constants in equation 7 are derived as follows, ΔK_{th} = 5 MPam$^{1/2}$ for RRA, 4.2 MPam$^{1/2}$ for T6, C_1=2.65 x 10^{-5} mm/cycle for RRA, 6 x 10^{-7} mm/cycle for T6, C_2= 1.05 for RRA, 2.75 for T6, C_3= 19 MPam$^{1/2}$ for RRA and 25.5 MPam$^{1/2}$ for T6 respectively. For fatigue crack growth prediction under service loads, an approximate sigmoidal shape of FCGR data is derived using the equation given in Eq. 7.

$$da/dN = C_1(\Delta K_{eff})^{C_2} \frac{[1 - (\Delta K_{th} / \Delta K_{eff})^2]}{[1 - (\Delta K_{eff} / C_3)^2]} \text{ ---------- Eq. (7)}$$
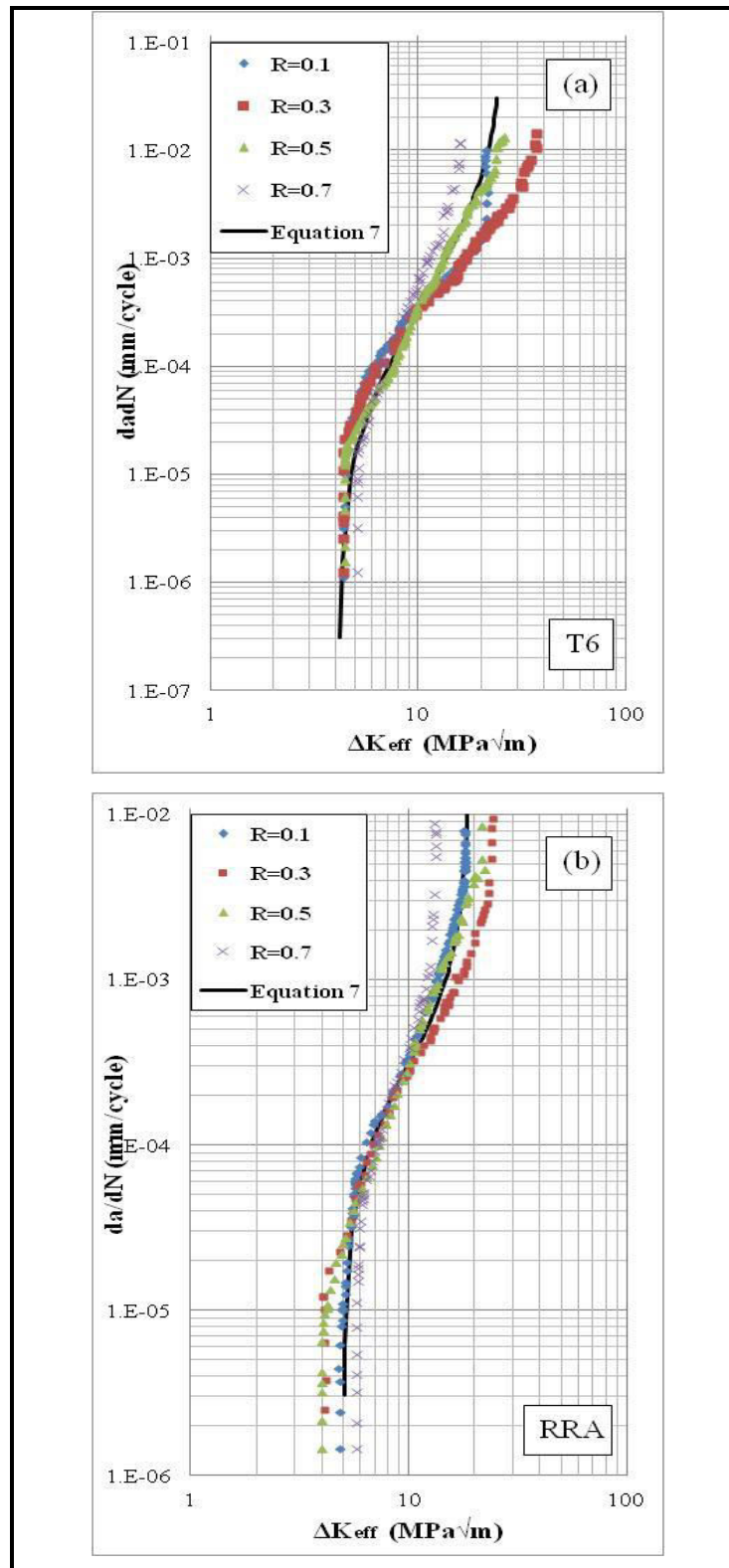
Fig. 5.13 Constant amplitude FCGR curves plotted using ΔK$_{eff}$ driving force; a) T6, b) RRA

The crack extension for each of the counted load cycles is determined and cumulative fatigue crack extension at the end of each load block is predicted using the above mentioned two models for both RRA and T6 treated alloys, is presented in Fig. 5.14. The experimentally determined fatigue crack growth life (N_{exp}) is 59 blocks for RRA treated alloy. The T6 treated alloy lasted for 48 blocks of the load cycle. Comparing the experimental results with that of the prediction, it is concluded that FCG prediction using ΔK^* by considering two parameter model results with a better correlation to the experimental results. The predicted results are in close agreement with that of the experimental results up to 25 number of spectrum load blocks in both RRA and T6 treated alloy samples. Even though the load interaction effects are not considered for the prediction of the fatigue crack growth behavior, the results are in close agreement with that of the experimental observations (Fig. 5.14). The fatigue life ratio, N_{pred} / N_{exp} is found to be 0.9 for both RRA and T6 treated alloys.
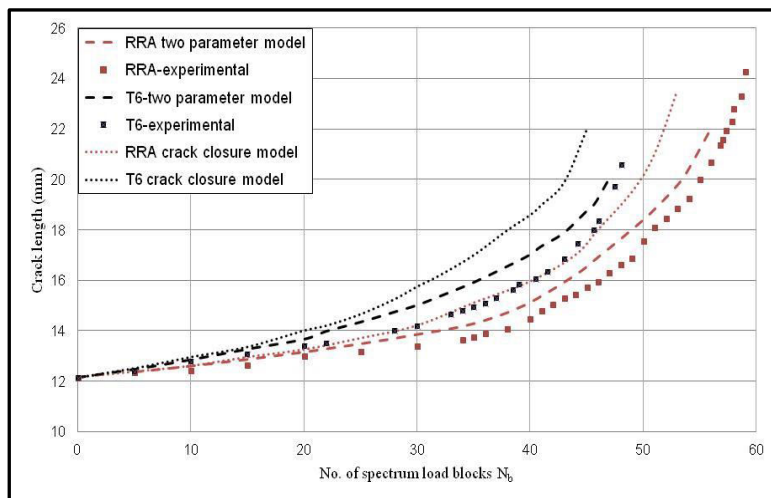
Fig. 5.14 Comparison plot for experimental and predicted FCG behavior for RRA and T6 treated alloys

5.5 Brief Summary of Fatigue Crack Growth Characterization

The chapter highlights the FCGR characteristics of alloy in mainly T6 and RRA conditions. The FCGR tests were performed at different stress ratios and compared, further the FCGR under service simulating loading condition (FALSTAFF) was carried to highlight the benefit of RRA treatment in enhancing the service life of the component made of RRA treated alloy. Further FCGR data was used for predicting the crack growth using a two parameter crack growth law and compared the results with experimental results. Results indicated better performance by RRA treated alloy.

Page left intentionally blank

CHAPTER 6

ELECTROCHEMICAL AND EXFOLIATION CORROSION BEHAVIOR OF ALLOY

6.1 Electrochemical Corrosion Tests

The electrochemical corrosion tests are carried out on the heat treated alloy samples. The derived polarization plots are shown in Fig. 6.1. The corrosion kinetic parameters such as corrosion potential (E_{corr}), corrosion current density (i_{corr}) and corrosion rate are derived from the Tafel plot which is listed in Table 6.1. The results infer that corrosion current density (i_{corr}) values vary significantly with the aging conditions. The i_{cor} values stood at 0.6, 1.2, and 0.4 $\mu A/cm^2$ for T6, T7451 and RRA treated samples respectively. The E_{corr} values for the RRA treated samples shifted towards noble direction i.e., towards positive potential, indicating higher resistance against the corrosion when compared to other aging conditions. There exists a reduction in corrosion current density by about 50 % for RRA alloy when compared to the standard T6 treated alloy. This is also evident from the corroded surfaces as visualized in an optical microscope which is shown in Fig. 6.2.
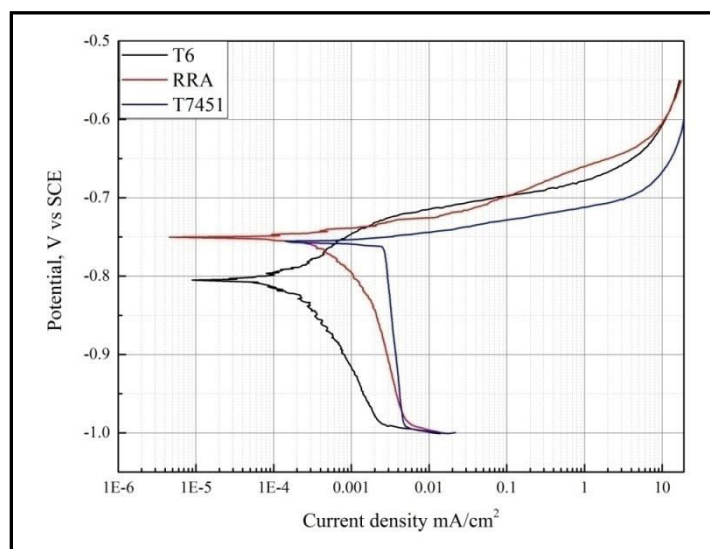
Fig. 6.1 Electrochemical corrosion behavior of the alloy subjected to different aging conditions
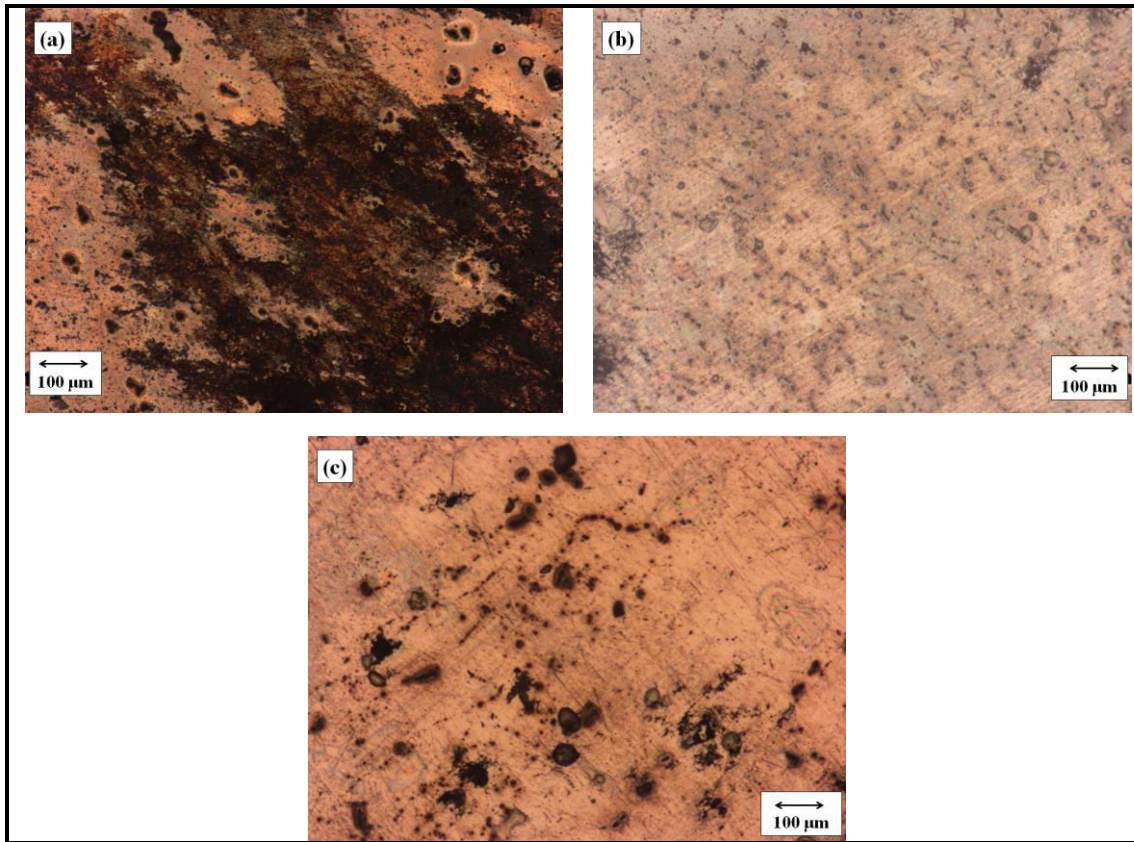
Fig. 6.2 Optical micrographs showing the corroded surfaces of the alloy in different aging conditions; a) T6, b) RRA, c) T7451

The electrochemical impedance spectroscopy is performed; the derived EIS parameters such as solution resistance (R_s), passive film resistance (R_f) and charge transfer resistance (R_{ct}) are calculated from the fitted resistance curves as shown in Fig. 6.3. The total passive film resistance (R_p) is measured to be 22000 Ω cm^2 for RRA treated alloy which is about 22 % higher than the T6 tempered alloy and 15 % higher than the T7451 tempered alloy. The corroded surfaces of the T6 treated sample exhibited more amount of pit formation as compared to the T7451 and RRA alloy surfaces. Also the pits are observed on the entire surface of the T6 treated alloy, where in the RRA exhibited trivial corrosion.
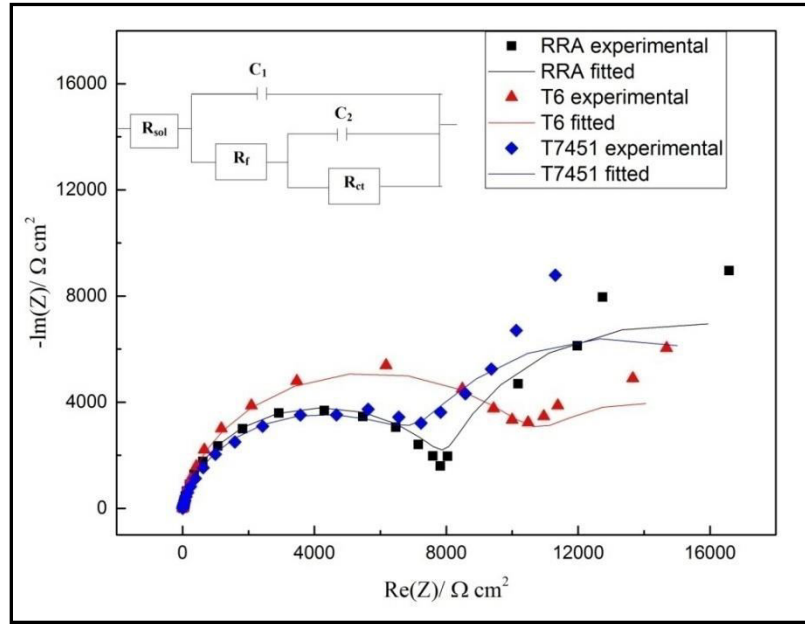
Fig. 6.3 Nyquist plot for the alloy in different tempers

Table 6.1 Electrochemical test data for the alloy under different tempered conditions in 3.5 % NaCl

Temper conditions	E_{corr} mV	I_{corr} μA	βa mV/dec	-βc mV/dec	Corrosion rate mm/y	R_{sol} Ω cm^2	R_f Ω cm^2	R_{ct} Ω cm^2
T6	-806	0.6	59	121	0.00954	8.1	11050	7469
RRA	-741	0.4	20	315	0.00142	8.2	8463	14225
T7451	-756	1.2	12	941	0.014	6.5	8201	11100

6.2 Exfoliation Corrosion Tests

The exfoliation corrosion test results are presented in Fig. 6.4. From the visual observation on the corrosion surfaces, it could be qualitatively concluded that T6 is severely corroded in comparison to the T7451 and the RRA alloys. The exfoliation depth in different treated alloys infers its influence on the corrosion attack. Figure 6.5 shows the exfoliated surfaces i.e., cross sectional view perpendicular to the exposed area. This demonstrates that the RRA alloy being less severe to exfoliation in comparison to the T6 alloy. The depth of attack is measured to be 70-90 μm in RRA alloy compared to 256 μm in T6 and 140 μm in the T7451 condition.
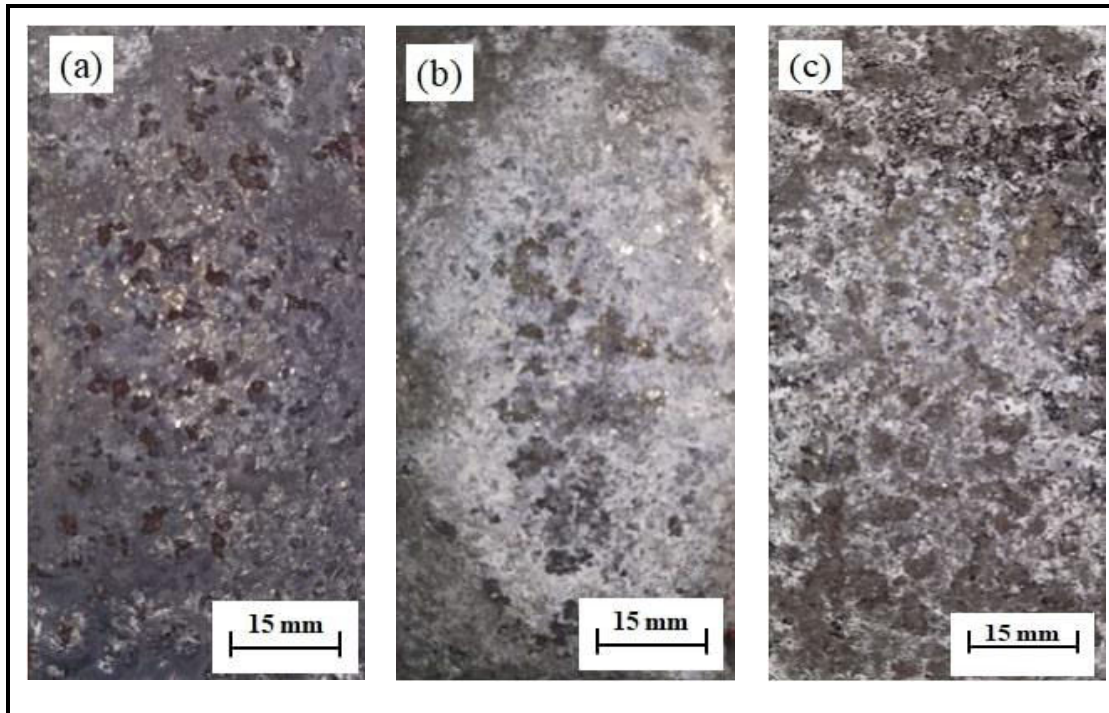
Fig. 6.4 Exfoliated surfaces of the aluminum alloy; a) T6 (EC), b) RRA 20 (EA), c) T7451 (EB)
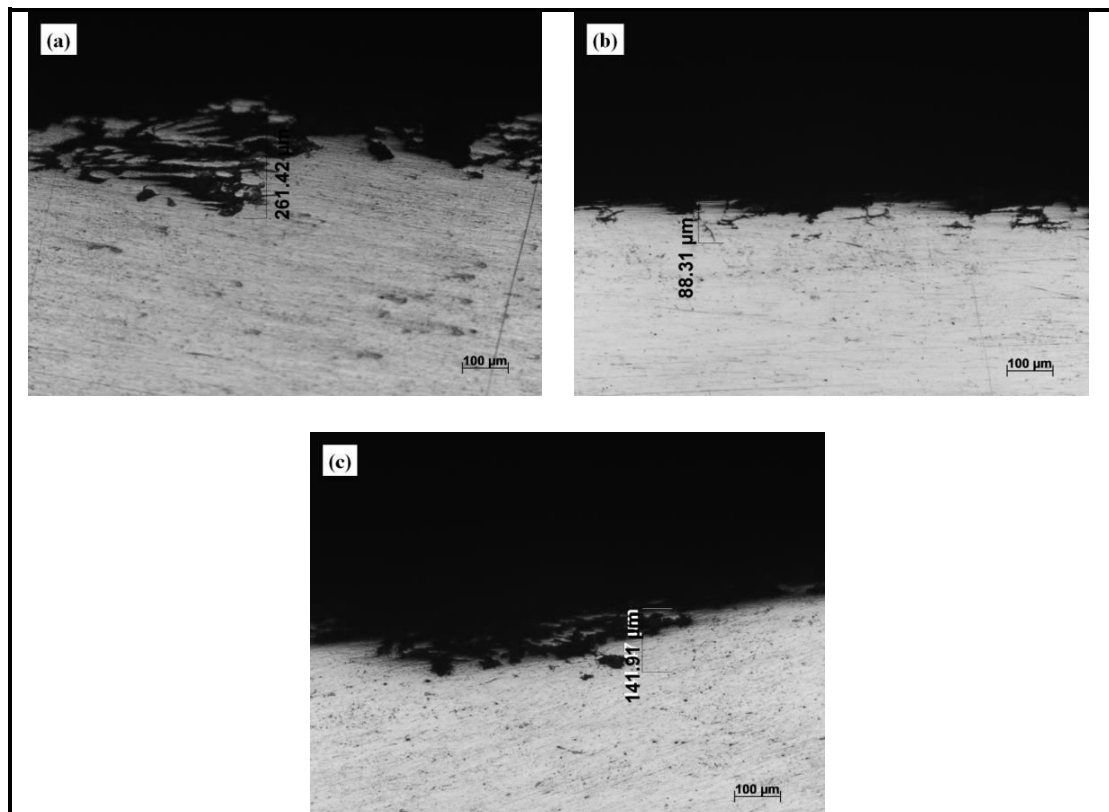
Fig. 6.5 Optical micrographs showing exfoliated surfaces of alloy in different aged conditions; a) T6, b) RRA-20 min, c) T7451

The closer observation on the exfoliation could be visualized from the SEM micrographs shown in Fig. 6.6. The corrosion attack on the grain boundary is the predominant mode of exfoliation in all three different tempered alloys as shown in Fig. 6.6. The crack is more tending to extend along the grain boundaries leading to exfoliation of the rolled alloy. The depth of attack from the top surface in RRA treated alloy is much lesser as compared to T6 treated alloy (shown in Fig. 6.5 a-c).
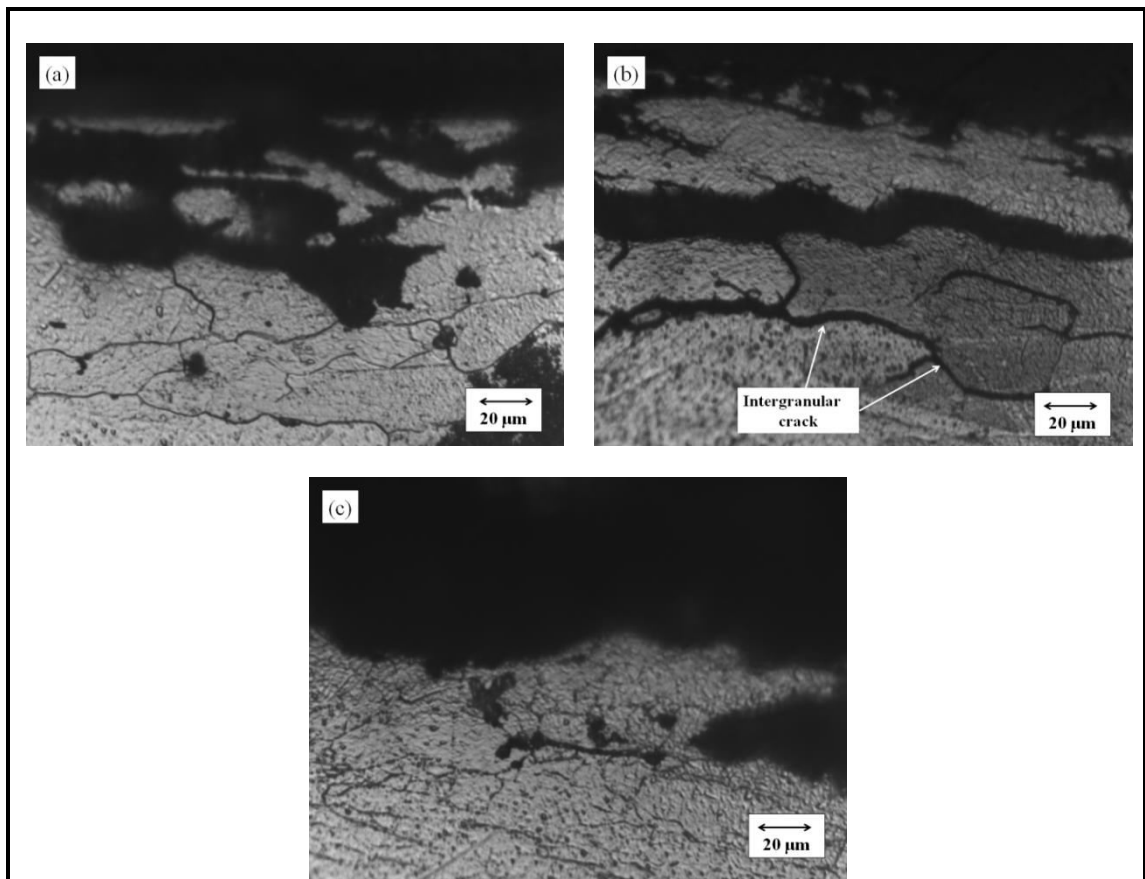
Fig. 6.6 Optical micrographs showing high magnified micrographs of exfoliation and crack propagation along grain boundaries; a) T6, b) RRA, c) T7451

6.3 Summary of Corrosion Test Results

Chapter highlights the behavior of alloy under electrochemical corrosion tests and also under exfoliation tests. The RRA sample exhibits highest Ecorr and highest resistance to corrosion attack which was evident from the type of pits formed after the test. The exfoliation test which is a qualitative study also shows better resistance to exfoliation of the alloy under RRA treatment.

Page intentionally left blank

CHAPTER 7

DISCUSSION

7.1 Peak-Aging Behavior

The sequence of precipitation in a precipitation hardenable 7xxx aluminum alloy is (Wang et al. 2007):

SSSS (super saturated solid solution) $\longrightarrow$ GP zones $\longrightarrow$ η' $\longrightarrow$ η (MgZn$_2$)

The Guinier-Preston zones which are group of solute atoms (~ 500 atoms) that are the one dimensional ordered form, that are first evolved during the aging process. In the Al-Zn-Mg-Cu system, MgZn$_2$ precipitates are evolved which form a hexagonal close packed crystal structure with its basal planes being coherent with the aluminum matrix (Ma et al. 2014). The orientation relationship of these MgZn$_2$ precipitates with aluminum lattice is given as (111)Al || (0001)η' and (011)Al || [1010]η' (Srivatsan et al. 1997). It was reported that η' precipitates exhibit lattice parameters with a= 0.5078 nm and c=1.395 nm. These precipitates are generally of disc shaped with size being 2 nm x 20 nm. The η precipitates are the stable state precipitates of MgZn$_2$ which are incoherent with the matrix, they exhibit lattice parameters with a= 0.521 nm and c=0.860 nm (Löffler et al. 1983). The quaternary phase diagram shown in Fig. 7.1 confirms the dissolution of secondary phase particles for this particular alloy system (Lim et al. 2003) at temperature 490 °C.
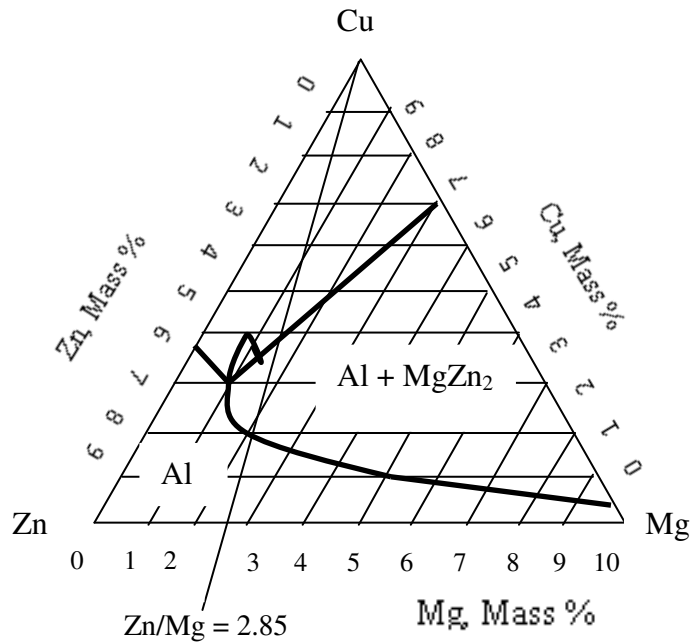
Fig. 7.1 Quaternary phase diagram of 90% Al 6.3%Zn 2.2%Mg 1.5%Cu system at 763 K (Redrawn from (Lim et al. 2003)

The heat treatments performed at different temperature levels create different types of the strengthening precipitates. They create different types of interfaces between the precipitates and the matrix. The coherent and semi-coherent precipitates are formed by aging at low temperatures. They create a misfit strain with the aluminum lattice thereby requiring more energy for the dislocation to cut and move through them (Andersen et al. 2018). Hence coherency strengthening mechanism plays a role in enhancing the strength of these alloys. The coherency strengthening mechanism is given by Kovács et al. (1980).

$$\tau_c = \beta G \varepsilon^{3/2} f_v^{1/2} (R/b)^{1/2}$$ -------------- Eq. (8)

Here τ_c is the strengthening stress, G is the shear modulus, b is the Burgers vector, ε is the coherency strain, β is a constant which is 1 for edge dislocation and 3 for screw dislocation, f_v and R are the volume fraction and radius of the precipitates, respectively. It is evident from the above relation that an increase in number density and radius of the precipitates cause an increase in yield strength of alloy. As the precipitates are aged for prolonged time the number density of precipitates are reduced due to the coarsening stage of precipitation. The reduction in interface energy is the driving force for the growth of precipitates. Certainly the strength will increase

94

until a critical size is reached. Further increase in size of the precipitates by coarsening leads to Orowan looping mechanism. At this stage of precipitation, the precipitates are no more coherent with the matrix, inter-precipitate distance is increased and thereby dislocation bows around the precipitates, the precipitate density is reduced thereby reduction in strength (Li et al. 2016).

7.2 Effect of Retrogression and Re-aging on the Microstructure of the Alloy

The peak-aged alloy when reheated to a high temperature of about 200 °C (i.e., during reversion stage), the partial dissolution of the fine precipitates take place in the matrix. At this stage of heat treatment the previously existed precipitates that are unstable in nature are dissolved completely, the metastable precipitates such as η' dissolve partially (Meng et al. 1997). Therefore density of fine precipitates in the matrix is reduced as observed in the TEM micrographs in Fig .4.9 a. The stable precipitates grow further to become larger in size.

The microstructure reveals that for varied reversion treatment time i.e., 10-60 min, when this is followed by re-aging, until the retrogression time of 30 min is reached, the matrix is majorly consisting of fine scale precipitates of size 2-5 nm. These precipitates account for the strengthening of the alloy as observed in hardness profile shown in Fig. 4.21. As the retrogression time is further increased i.e., above 30 min, the dense fine scale precipitates of 2-5 nm that are present earlier, either get dissolved (when extremely small) or grow in size to about 5-10 nm. These precipitates become the majority in numbers after RRA treatment.

7.3 Tensile Strength and Hardness of the RRA Treated Alloy

The RRA treated alloy consists of two kinds of precipitates in the matrix, one being finer in size (5-10 nm) and other being grown to a larger size (12-20 nm). Though the precipitates are grown in size they are considered to be still in an intermediate state of growth thereby exhibiting dislocation shearing mechanism as shown in Fig. 7.2. Since the reversion treatment time is very short which is about 20 min, the precipitates are still exhibiting intermediate state and are semi-coherent in nature (Fig. 4.14). These precipitates in RRA condition are the primary cause for the strength characteristics

being similar to the T6 alloy. The η' precipitates that are partially dissolved during retrogression, further become elongated discs of size 12-20 nm. During this stage of re-aging, the grain boundary precipitates η, which grow further to become coarsened forming a size of about 25-50 nm.

The evolution of precipitates has a direct influence on the hardness and tensile strength. The majority of precipitates being semi-coherent in nature, which makes the alloy, attain the ultimate tensile strength as equal to that of the standard peak-aged alloy. The continuous drop in yield strength while reversion is continued for longer than 20 min could be due to two reasons; one being the change in precipitate size distribution (Marlaud et al. 2010a) and another factor could be due to the growth and transformation of the precipitates as retrogression time is increased (Fig. 4.11 a-f). From Fig 7.3 it could be seen that few of the matrix precipitates are in similar nature to that of the GBP's as observed from dark-field TEM micrographs.
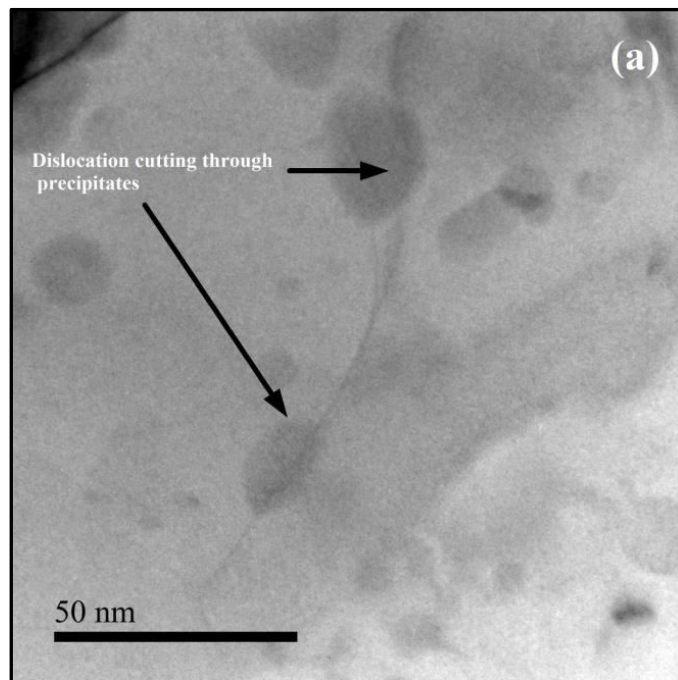
Fig. 7.2 Bright-field TEM micrographs showing dislocation shearing through the precipitates in a tensile tested RRA treated alloy
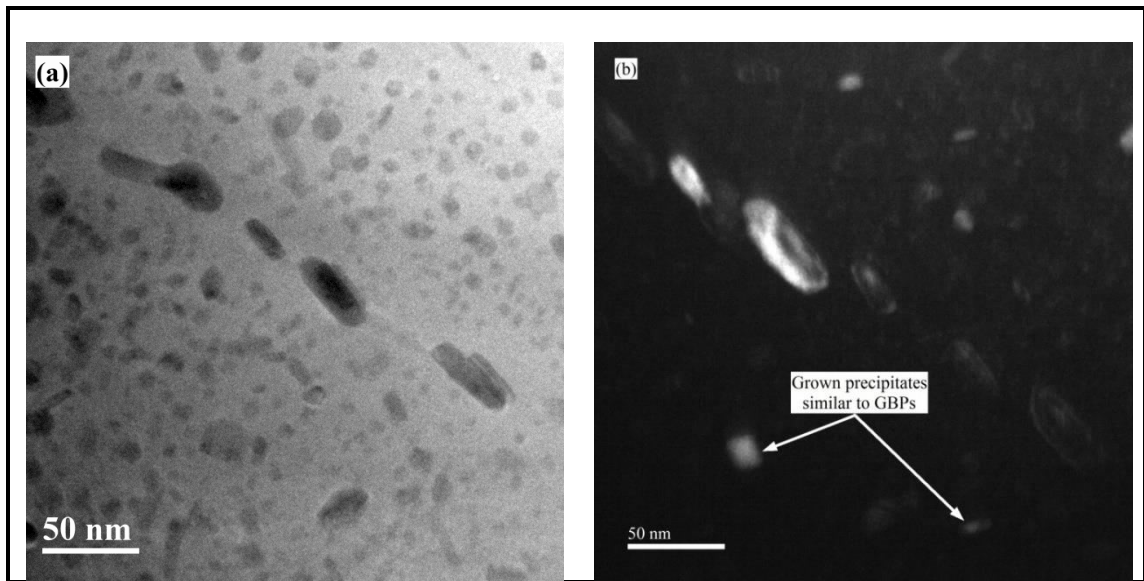
Fig. 7.3 TEM micrographs of the RRA treated alloy along $[111]_{Al}$; a) Bright-field micrographs, b) Dark-field micrographs highlighting the coarsened matrix precipitates

7.4 Effect of Retrogression Time on the Grain Boundary Microstructure

The grain boundaries are the high energy region, where the precipitates ($MgZn_2$) get formed in a discontinuous fashion during reversion treatment (Fig. 4.17 a-f). The region around the GBP's is depleted with precipitates which forms a precipitate free zone (PFZ). This may be either due to the vacancy sink to the grain boundaries during quenching, after high temperature reversion treatment. The precipitate free zone size which is 25-30 nm as observed in the T6 alloy increases to 35-37 nm in the RRA alloy. The coarsening of grain boundary precipitates could be the reason for reduced ductility observed under tensile test of the RRA treated samples (Angappan et al. 2011).

7.5 Effect of RRA on Fracture Toughness of the Alloy

The fracture toughness of the aluminum alloy depends on many factors, such as coarse impurity particles, grain size, shape, intermetallic particles, precipitates and precipitate free zone size (Deshpande et al. 1998; Dorward and Beerntsen 1995; Kamp et al. 2002). The grain size and sub grain formation is observed in both T6 and RRA treated alloys during solution treatment. The change in fracture toughness is co-related to the size of the grain boundary precipitates and nature of the PFZ. The area

fraction of the grain boundary precipitates is more in the T6 treated condition, which can act as stress risers during loading. The cohesive strength between the GBP's and the matrix gets diminished. This leads to the formation of fine cracks leading to the intergranular fracture (Han et al. 2011). In the case of T7451 and RRA samples, the GBP's are discontinuous, which reduce the area fraction of GBP's. The size of the matrix precipitates is slightly higher, which brings down the strength difference with the grain boundary region. The PFZ width is larger and helps in relieving the stress concentration (Marlaud et al. 2010b). The PFZ width is intermediate between that of the T6 and T7451, and this could be the reason for RRA sample to exhibit higher fracture toughness than the T7451.

7.6 Constant Amplitude Fatigue Crack Growth Life

Typical FCGR curves shown in Fig 5.1 demonstrate a reduction in the near-threshold crack growth rate in 7010 alloy subjected to RRA treatment. The SEM fractographs taken from the near-threshold regime for both the RRA and T6 treated alloys is shown in Fig. 7.4. The fractography indicates fatigue crack growth with the formation of larger faceted morphology in the RRA treated sample when compared to the smaller facets formed in the T6 treated alloy. The larger facets formed on the RRA treated alloy in the near-threshold regime is an indication of more room for the dislocation movement during cyclic loading. The magnified micrographs (Fig. 7.4 c, d) highlight the formation of slip steps on the facets formed. These facets formed in RRA sample are consisting of persistent slip bands, which increases the fatigue crack growth resistance. The persistent slip bands are not observed in the case of T6 sample. It is reported (Chen et al. 2012) that having persistent slip bands promote roughness induced crack closure mechanism leading to higher fatigue crack growth resistance. This indicates that the increase in the spacing of precipitates within the matrix of RRA has resulted in larger facets thereby cyclic slip reversibility is promoted. This is similar to the observations reported earlier (Chen et al. 2012; Wang et al. 2014). A typical fatigue fracture surface appearance with formation of striations in the Paris' regime is shown in Fig. 7.5. A similar nature of transgranular crack propagation through different grains is observed for both the RRA and T6 treated alloys as depicted in Fig. 7.5 (a, b). The magnified micrographs of Fig. 7.5 (a, b) with striation

spacing is shown in Fig. 7.5 (c, d). However the spacing of fatigue striations formed are measured corresponding to ΔK = 12 MPa√m indicates a higher crack growth rate (striation spacing of 0.6 μm) in the T6 treated alloy compared to the striation spacing of 0.35 μm in RRA treated alloy. This result matches quite well with the FCGR data. The fatigue rupture in the high ΔK regime is shown in Fig. 7.6, and it indicates ductile, dimple type of failure in both RRA and T6 treated alloys. Hence the final fracture at high ΔK regime is showing not much difference in the fractographs. This correlates fairly well with the final fracture regime. For both T6 and RRA treated alloy's the FCGR curves merge into single band at any stress ratio (0.1-0.7) as shown in Fig. 5.2 (a-c).
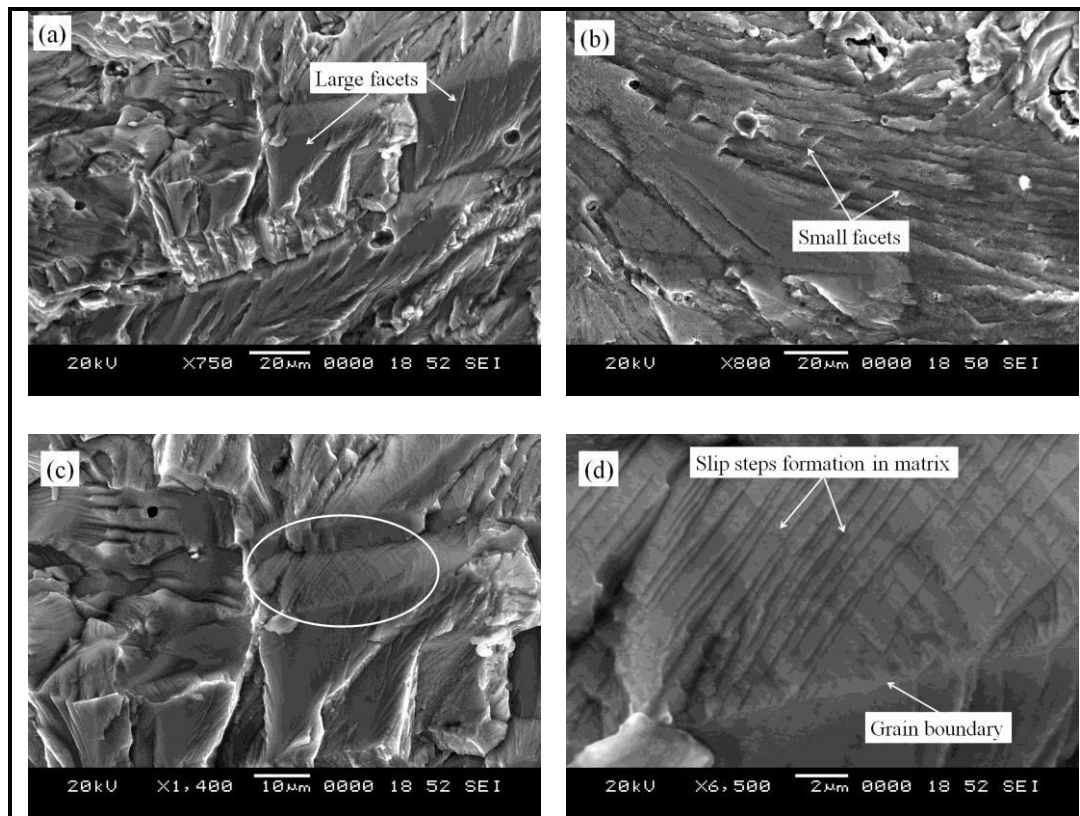
Fig. 7.4 SEM fractographs in the near-threshold fatigue crack growth regime. (a) RRA treated alloy, (b) T6 treated alloy, (c, d) High magnification micrographs of Figure a showing slip steps formed
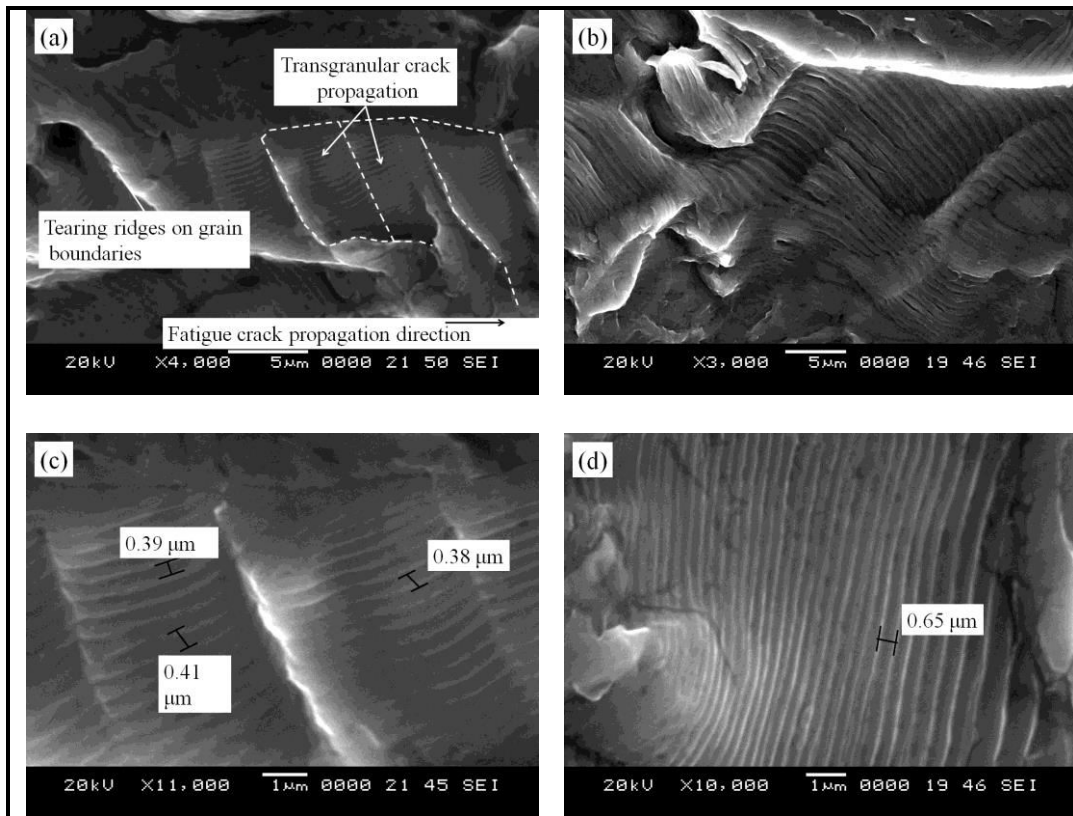
Fig. 7.5 SEM fractographs in the Paris' regime; a) RRA alloy b) T6 alloy ($\Delta K \sim 12$ MPa$\sqrt{m}$, R=0.5) c) and d) are magnified micrographs of a) and b) respectively
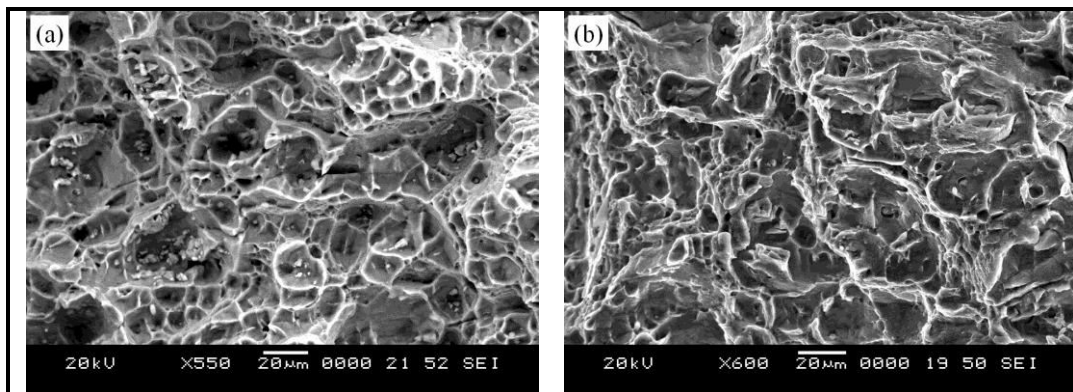
Fig. 7.6 SEM fractographs in the high ΔK regime; a) RRA treated alloy b) T6 treated

7.7 Fatigue Crack Closure in 7010 Alloy

From the results obtained in this investigation, it confirms that the RRA heat treatment modifies the microstructure of the alloy and exhibits improved fatigue crack growth resistance in the material. Fatigue crack closure mechanisms have been shown to influence the FCGR behavior in various materials (Pokorny et al. 2017; Vasudeven et al. 1994). Plasticity induced (Costa and Ja 2017; Elber W 1970), oxide induced (Chemin et al. 2015) and fracture surface roughness induced (Ritchie 1988) crack closure mechanisms have been mainly used to explain the observed FCGR behavior. In the present investigation, from the load-CMOD curves it could be seen that the crack closure is dominant in the lower stress ratio range (R=0.1-0.3). At higher stress ratios, such as, R ≥ 0.5, crack mouth being open completely even at a minimum load of the fatigue load cycle, the effect of the crack closure are expected to be almost negligible. The crack surface roughness which is measured at near-threshold regime, using the confocal microscope is shown in Fig. 7.7.
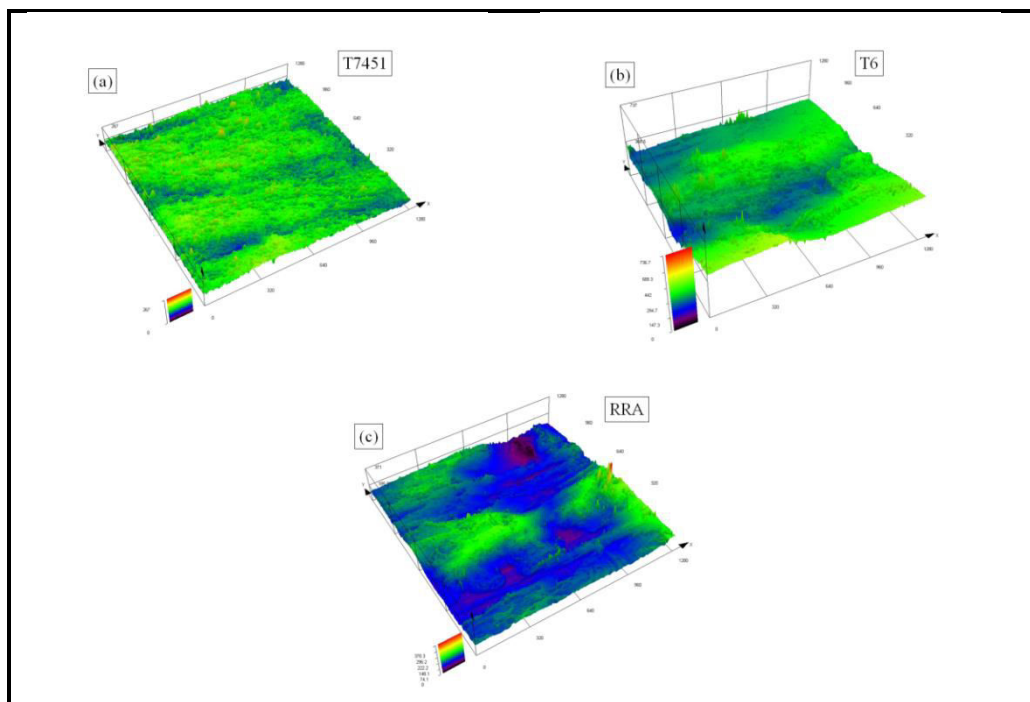
Fig. 7.7 Fatigue crack surface roughness profile in the near-threshold regime; a) T7451, b) T6, c) RRA

101

Table 7.1 Fracture surface roughness measured on FCGR tested samples

Trials	Roughness (avg) S$_a$ (µm)						Roughness (peak) S$_p$ (µm)					
	T7451		T6		RRA		T7451		T6		RRA	
	S$_a$	Avg	S$_a$		S$_a$	Avg			S$_p$	Avg	S$_p$	Avg
1	14.3		26.1		27.4		100.2		150.6		152.2	
2	21.5	18.7	25.1	24.7	35.4	31.7	112.9	128	114.6	132	195.5	163
3	20.4		22.9		32.2		171		131.2		141.3	

The surface roughness measured (peak value and average value) is listed in Table 7.1. The average roughness is measured to be 31.7 µm, 24.7 µm, 18.7 µm in RRA, T6 and T7451 conditions respectively. A higher level of roughness is observed in the RRA treated alloy which confirms the roughness induced crack closure contributing to crack growth resistance in the near-threshold regime.
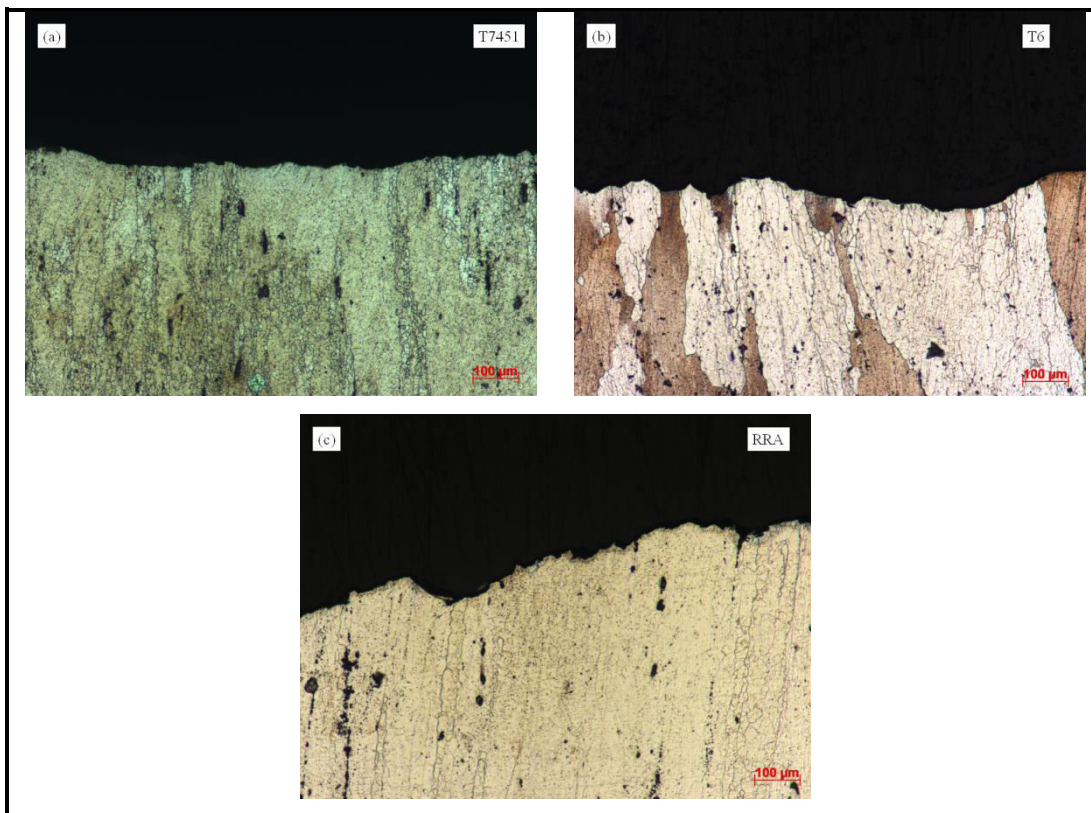
Fig. 7.8 Optical micrographs of the fatigue crack profile in near-threshold regime; a) T7451, b) T6, c) RRA

The cut section of the CT specimen close to the near-threshold regime is observed under light microscope (Fig. 7.8). The view perpendicular to the crack plane, is observed. This infers that the RRA treated alloy exhibits a torturous crack path when compared to the T6 and T7451 conditions of the alloy. The observed surface roughness and tortuous nature of crack propagation in the RRA treated alloy justifies the occurrence of partial crack closure measured in the RRA treated alloy. During a fatigue load cycle the crack surfaces touch each other before the minimum load is reached. The cyclic load acting on the specimen is as represented in schematic diagram in Fig. 7.9 showing the effective SIF ΔK_{eff}.

The fatigue crack closure mechanism has been observed to be operative at low stress ratio up to R=0.3. Thus, the enhanced crack closure levels observed in the RRA treated alloy would result in reduced effective stress intensity range as:

$$\Delta K = K_{max} - K_{min} \quad \text{-----------Eq. (9)}$$

$$\Delta K_{eff} = K_{max} - K_{cl} \quad \text{-----------Eq. (10)}$$

Thus, the FCGR in the RRA treated alloy is lower than that of the T6 treated alloy due to the reduced effective stress intensity range, as observed in the present study. However, at higher stress ratios R $\geq$ 0.5, crack closure is absent in both materials (Fig. 5.4 c, d) however, still crack growth rates in the RRA alloy are lower than the T6 alloy which cannot be attributed to crack closure contribution. Hence, the intrinsic mechanism of the crack growth itself is expected to cause a reduction in the fatigue crack growth rates in the RRA treated aluminum alloy.
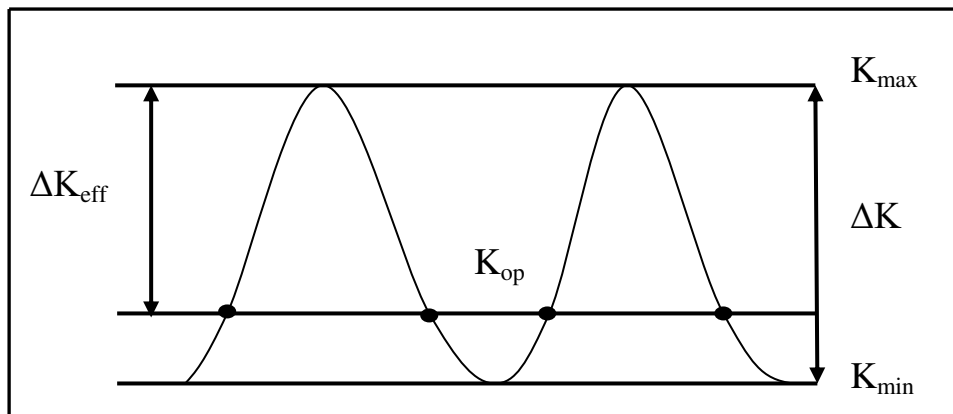
Fig. 7.9 Schematic illustration of effective ΔK during a fatigue cycle under crack closure effect domain

It has been shown that various microstructural features such as grain size, precipitates, and PFZ influence the FCGR behavior (Chen et al. 2013a; Desmukh et al. 2006). The grain size measured in the T7451 alloy is about 10-15 μm. After solution treatment at high temperature (490 °C for 6h) the grains are grown to larger size, along with the formation of sub-grains in the T6 and RRA treated alloys as shown in Fig. 7.10. The presence of Al_3Zr dispersoids as shown in SAED pattern in Fig. 4.14 which generally act as pinning sites for grain boundaries (Rometsch et al. 2014) and expected to prevent grain growth and re-crystallization. However in this case after heat treatment such as T6 and RRA the microstructure of the alloy exhibit the occurrence of grain growth and sub-grain formation as shown in Fig. 4.2,4.3 and Fig. 4.5. The sub-grains are formed mainly during the stage of solution treatment which is carried at 490 °C for 6 hrs. Hence the torturous crack path could be due to the grain growth and sub-grains formed (Fig. 7.10) during high temperature solution treatment process.
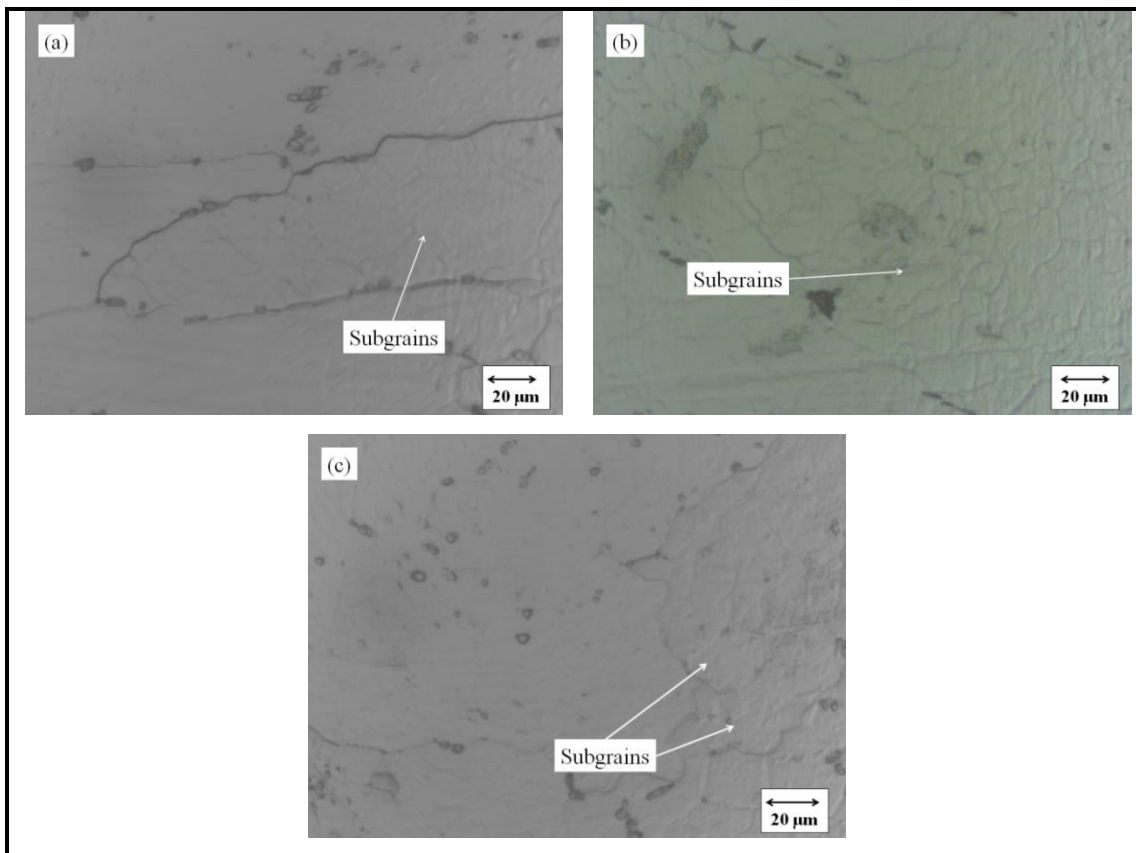
Fig. 7.10 Optical micrographs showing sub-grains formed in the 7010 alloy; a) T6, b) Reversion, c) RRA

It has been shown in literature that the nature of the PFZ adversely affects the fatigue crack growth behavior in aluminum alloys (Ogura et al. 2006, 2011). The GBP's PFZ surrounded by weaker PFZ lead to the void formation during loading, which further coalesces and promote intergranular cracking that results in higher fatigue crack growth rates (Chen et al. 2012). In the present study, the RRA treatment resulted in a marginal increment in width of the PFZ compared to the T6 treated alloy (Fig. 4.16 b). The fatigue fracture surfaces also show no major difference in the nature of crack propagation. Both RRA and T6 treated alloys exhibits transgranular crack propagation. Therefore, the influence of PFZ on the reduced crack growth rate could be negligible.

The TEM microstructure in the RRA treated alloy reveals, the grain interior (Fig. 7.11 a) being partially occupied with η' precipitates which are shearable in nature. A significant amount of η' precipitates (15-20 nm) that are grown in size are evident in the RRA treated alloy. Though the precipitates are grown, they still act as shearable in nature, as observed in Fig. 7.11 (a ,b). The aluminum lattice being coherent with the shearable precipitates present in the grain interior, during cyclic loading the planar slipping of dislocation is promoted, leading to the extensive crack deflections that cause roughness induced crack closure (Borrego et al. 2004; Wang et al. 2014).
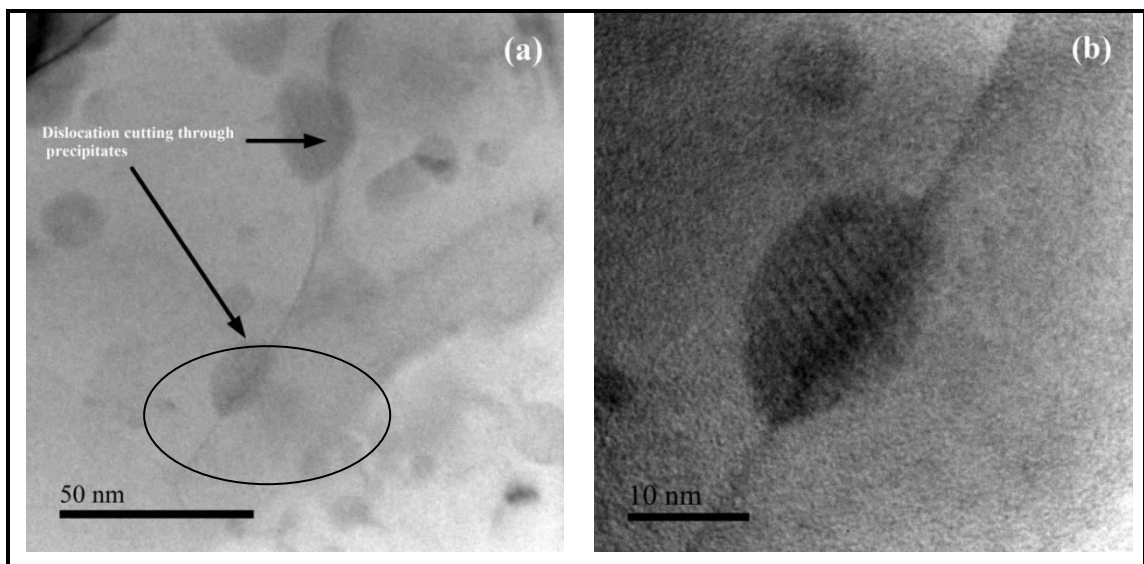
Fig. 7.11 a) Bright-field TEM micrographs from RRA treated tensile test sample showing dislocation through precipitate b) Magnified micrographs of the dislocation shearing through the precipitate

At the near-threshold regime of the FCGR, the plastic zone size at the crack tip is generally small, indicating average slipping distance of dislocation to be small (Xia et al. 2016). The FCGR behavior in the aluminum alloys, especially in near-threshold regime is observed to be influenced by the shearable nature of the precipitates. Both T6 and RRA treated alloys exhibit homogenous distribution of the shearable precipitates, but RRA microstructure with increased inter-particle spacing (10-12 nm) of the shearable precipitates, promote increase in cyclic slip reversibility of the dislocations (Xia et al. 2016), leading to reduced damage accumulation and hence reduced FCGR compared to the T6 treated alloy. Fig. 7.12 schematically illustrates the dislocations moving between the precipitates having more room for cyclic slip before interacting with next precipitate in the RRA sample compared to the T6 sample. Though, the crack closure effect (Fig. 5.4 a, b) exists at near-threshold regime, the dominance of reversible cyclic slip in enhancing the resistance to crack propagation is evident by the absence of the closure effect (Fig. 5.4 c, d) at high-stress ratios (R = 0.5, 0.7).
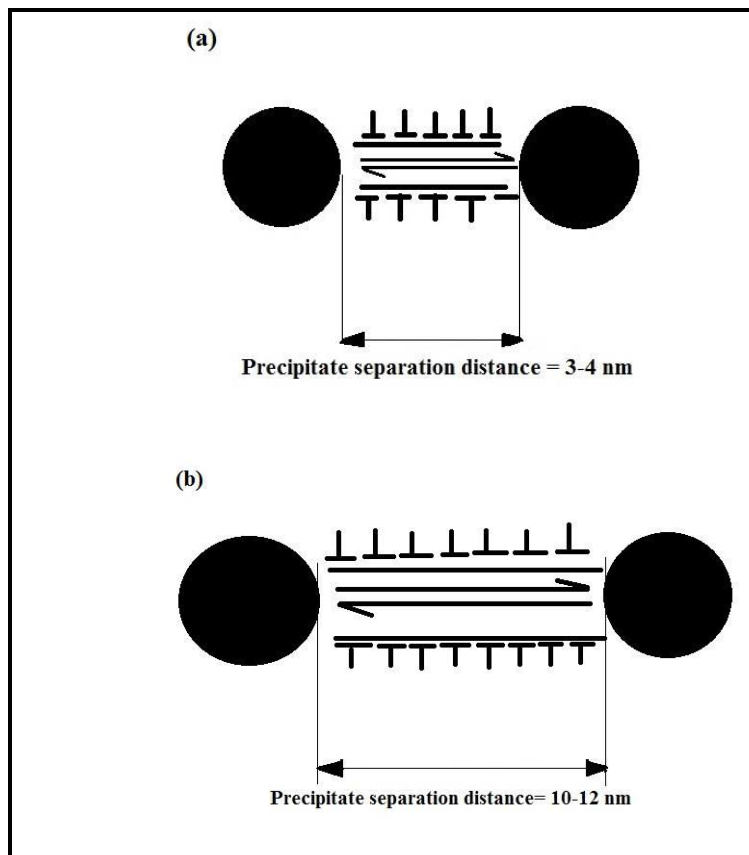
Fig. 7.12 Interparticle spacing of the matrix precipitates and their interaction with dislocations; a) T6, b) RRA

At high ΔK regime of FCGR, the stress levels are high, plastic zone size becomes large as shown in Fig. 7.13. The average free slipping distance of dislocations is also large. At high ΔK regime, the fatigue crack dependence on the microstructure is diminished and loading dominates the crack growth behavior (Xia et al. 2016). Hence the advantage of cyclic slip reversibility is reduced as the ΔK reaches above the Paris' regime of the crack growth curve. The difference in the crack growth rate narrows down (Fig. 5.2 a-d) and coincides with that of the T6 treated alloy.
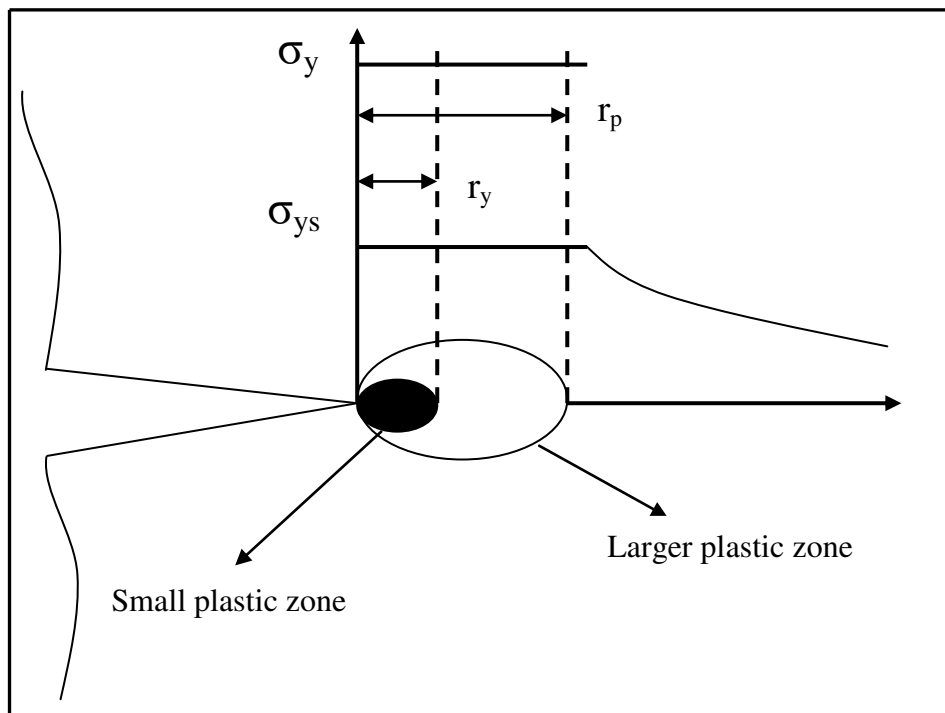
Fig. 7.13 Schematic illustration of the plastic zone formation during the fatigue cycle (redrawn from (Ricardo and Miranda 2016)

7.8 Experimental FCG Test under Spectrum Loading

The observed improvement in the fatigue crack growth life to failure in the RRA treated alloy under service loads is very much advantageous for its application in the aircraft structures. The improvement in fatigue crack growth life by about 22 %, is hence due to the inherent high resistance of the material against fatigue crack growth. This resistance appears to have resulted in increasing the damage tolerance capability of the 7010 alloy with RRA treatment. During spectrum loading, the accumulated damage per block is considerably reduced and hence increases the fatigue life of the alloy in RRA condition. The fracture surface of CT specimens tested under spectrum load is shown in Fig. 7.14.

The fractographs shown in Fig. 7.14 (a, b) also show the reduction in total fatigue crack length in the T6 alloy when compared to the RRA alloy before the final failure. The fracture surface of the RRA treated alloy consists of total fatigue crack length of about 31 mm (Fig. 7.14 a) before final failure, compared to 26 mm (Fig. 7.14 b) measured on the T6 treated alloy. The presence of faceted morphology of crack growth is also evident along with the fatigue striations in the RRA alloy (Fig. 7.14 c, d). The increase in the spacing between the matrix precipitates of about 10-12 nm observed in the RRA treated alloy (Fig. 7.2 a) has lead to promote enhancement in the reversibility of dislocation movement during fatigue loading (Xia et al. 2016). Hence damage accumulation per cycle is reduced.
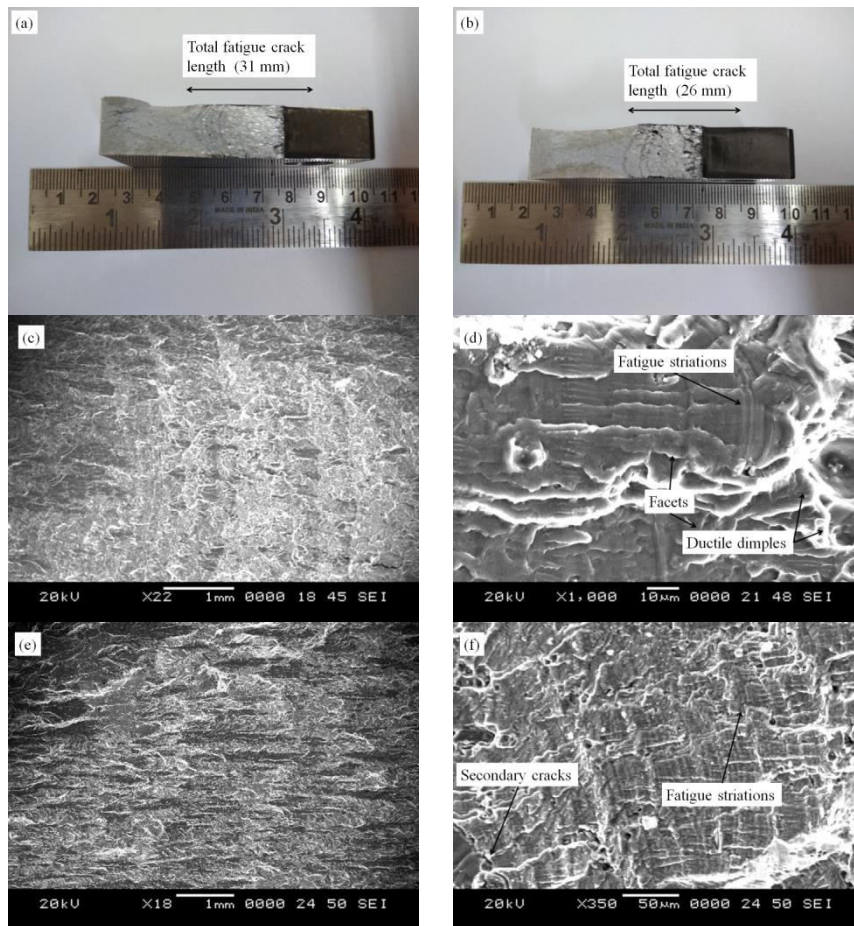
Fig. 7.14 Fatigue fracture surfaces of the alloy under FALSTAFF loading; (a,c,e) RRA, (b,d,f) T6

7.9 Prediction of FCG under FALSTAFF Loading

Several studies have been made to incorporate the effect of the load ratio R on the fatigue crack growth rates in the crack growth equation. Walker (Walker 1970) denoted Eq. (11) as:

$$\frac{da}{dN} = C[(1-R)^m K_{max}]^n = C[(1-R)^{m-1} \Delta K]^n ---\text{Eq. (11)}$$

Where C, m, n are the material constants. However, these equations appear to suit only for the Paris' regime of the entire fatigue crack growth curve. The crack closure concept introduced by Elber (Elber W 1970) has been used in the past for decades which make use of the effective stress intensity factor range ΔK_{eff} to account for crack closure as:

$$\frac{da}{dN} = C(\Delta K_{eff})^n = C(\gamma \cdot \Delta K)^n ---------- \text{Eq. (12)}$$

where γ is the crack closure parameter (Li et al. 2012) which is defined as:

$$\gamma = \frac{S_{max} - S_{op}}{S_{max} - S_{min}} = \frac{K_{max} - K_{op}}{K_{max} - K_{min}} = \frac{1 - K_{op}/K_{max}}{1-R} ----------- \text{Eq. (13)}$$

Here,

da/dN - Crack growth rate in mm/cycle

ΔK_{eff} - Effective stress intensity range

S_{max} - Stress at maximum load in a fatigue cycle

S_{min} - Stress at minimum load in a fatigue cycle

S_{op} - Stress at crack opening load

K_{max} - Stress intensity corresponding to the maximum load

K_{min} - Stress intensity corresponding to minimum load

K_{op} - Stress intensity corresponding to crack opening load

R - Stress ratio

γ - Crack closure level

The problem associated with the crack closure concept is the difficulty in determining the crack closure load P_{cl} (Vasudeven et al. 1994). These difficulties associated with the accuracy of measuring the crack closure load has lead to explore empirical methods to model and predict the crack growth under service loads. The crack closure level γ generally varies with three distinct regions of the crack growth rate data. It was reported that in the near-threshold regime of the crack growth, the crack closure level increases with a decrease in the stress intensity range. Whereas the crack closure is independent of the stress intensity range in the Paris' regime, and finally, in the high ΔK regime, the closure level decreases with an increase in ΔK (McClung 1991).

There also exists a debate over the use of crack closure concept, wherein a few researchers have opined that the closure has limited influence on the crack growth, since it is the role of the crack surface behind the crack tip which is nowhere related to the damage occurring ahead of the crack tip (Vasudevan et al. 2016). It is also reported, a closure based model that uses a crack closure concept based on only compliance change is unreliable (Vasudeven et al. 1994). Hence, there exist a lot of challenges and inaccuracies in measuring the exact closure level using compliance based technique (Hertzberg et al. 1988). This was later overcome by adopting a new concept called partial crack closure mechanism, which considers the formation of significant fatigue damage at the crack tip for the load levels well below the crack opening load measured (S_{op}) by compliance method (Kujawski 2001b). Further from their study Sadananda and Vasudevan (Vasudevan and Sadananda 1995; Vasudeven et al. 1994) have suggested that closure has limited influence on the damage reduction, as the crack extension is mainly influenced by the damage process ahead of the crack tip.

They suggested considering two independent parameters ΔK and K_{max} to completely define the FCG behavior. Therefore R ratio effects on FCGR have been correlated by the use of various models, such as K^* crack driving force model (Dinda and Kujawski 2004). This model takes care of both ductile and brittle materials. It was proposed that for a ductile material the FCGR is driven by ΔK, whereas for brittle material, it is driven by K_{max} experienced by the crack tip during the fatigue cycle. The ΔK^* based prediction model has resulted and correlated fairly well with the experimental data

and hence it could be used for designing as well as during the periodic maintenance of the aircraft structures to estimate the remaining life of components. In this investigation, the crack growth prediction using a two parameter crack growth life estimation has resulted with more closer agreement to experimental results. Hence it could be adopted for aluminum alloy 7010 in predicting the fatigue crack growth life.

7.10 Electrochemical Corrosion Behavior

The 7xxx alloys are prone to SCC and integranular corrosion when exposed to environment (Zhao et al. 2019). Hence it is necessary to characterize the behavior of these alloys under corrosion environment. The corrosion potential (E_{corr}) and corrosion current density (i_{cor}) are evaluated from the polarization curves and are reported in Table 6.1. From Fig. 6.1 it is noticed that a shift in the E_{corr} for RRA treated alloy towards the positive potential compared to the T6 alloy. These corrosion potentials measured are in close agreement with the earlier reports for these type of alloys (Rout et al. 2015b). The corrosion potential was highest for the T6 treated alloy and lowest for the RRA treated alloy and for T7451 being the intermediate level. The TEM-EDS is analyzed on the alloy matrix, which also indicates that the RRA matrix is enriched with Cu after reversion treatment (Fig. 7.18.) is also one of the reason for the observed reduction in corrosion potential of the RRA alloy (Marlaud et al. 2010a).

The increase in the total passive film resistance, R_p and shift in the corrosion potential of RRA tempered alloy towards more noble direction indicates high resistance to corrosion in the RRA treated alloy. This is evident when the corrosion surface is analyzed under an optical microscope. The amount of corrosion pits are formed are increased on the T6 alloy. In RRA alloy it is found with trivial pitting. The T6 microstructure consists of densely populated fine precipitates in the matrix, while in the corrosion medium they tend to form anodic dissolution around the precipitates forming more amounts of corrosion pits (Fig. 7.15 a). Unlike T6, the RRA alloy exhibits fewer corrosion pits (Fig. 7.15 b).
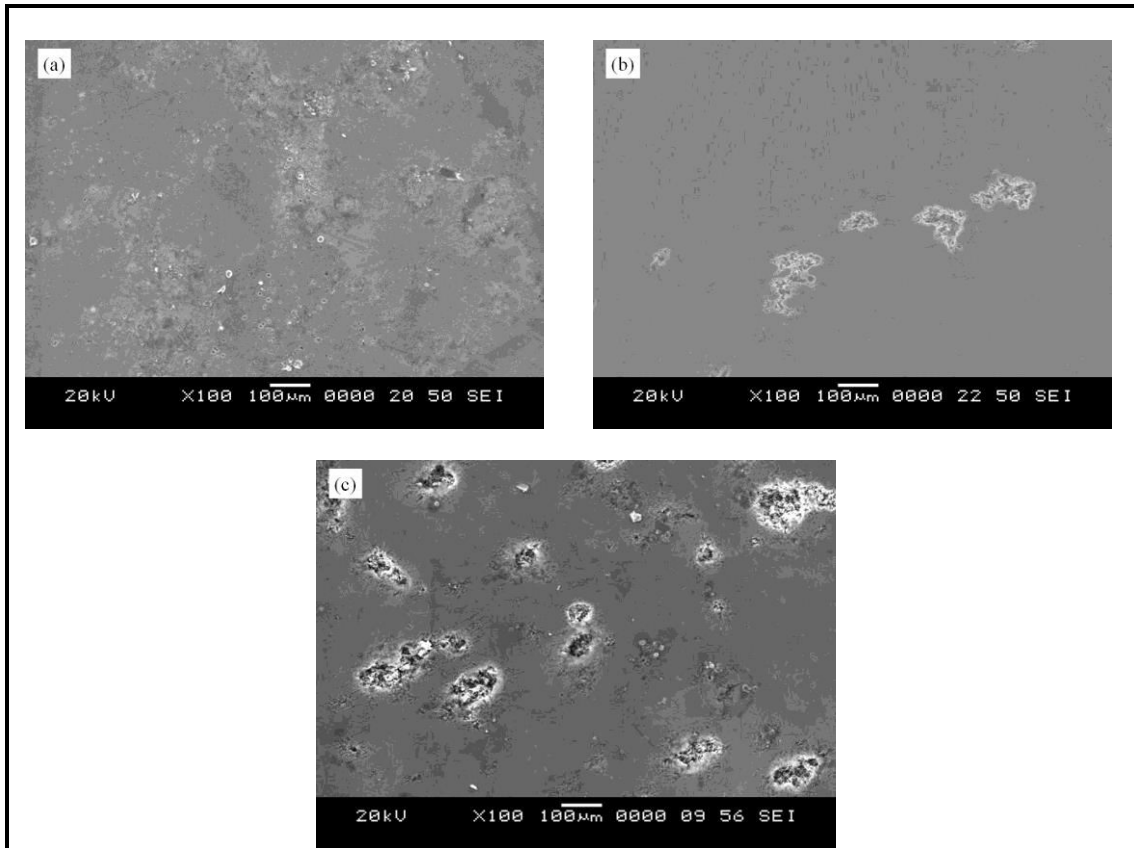
Fig. 7.15 SEM micrographs showing the corrosion pit formation in 7010 alloy in different heat treated conditions; a) T6, b) RRA, c) T7451

The corrosion pit morphology observed under SEM also infer that the RRA and T7451 treated alloys exhibit similar morphology of pits (flakes inside pits) (Fig. 7.16 b, c) compared to bubble type of morphology observed in T6 treated alloy (Fig. 7.16 a). The SEM-EDS analysis is carried on these corrosion products, which also indicates that the corrosion products in RRA alloy contain more amount of Cu compared to that of T6 as analyzed from EDS (Fig. 4.17). This is an indication that the T6 alloy matrix is having less amount of copper distribution in the matrix when compared to the distribution of Cu in RRA and T7451 as inferred from Fig. 7.17 (a-c).
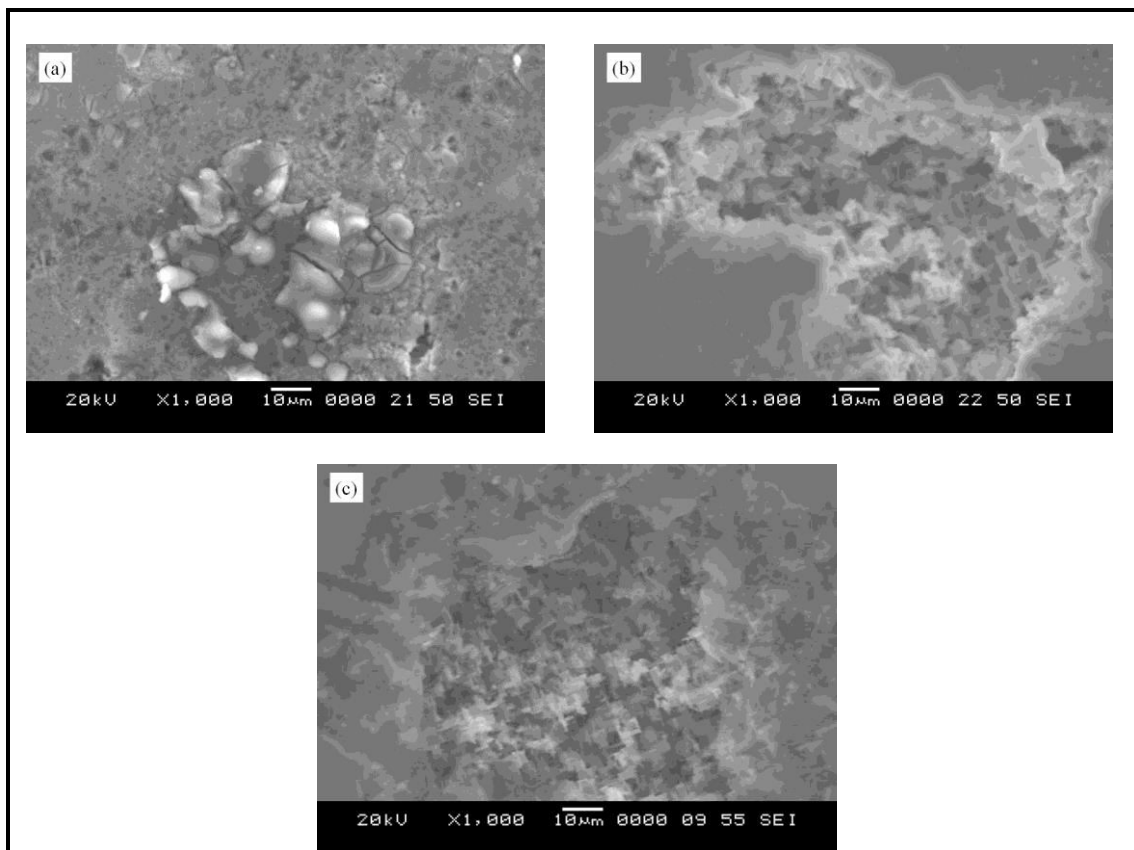
Fig. 7.16 High magnification SEM micrographs of the corrosion pits formed after electrochemical test; a) T6, b) RRA, c) T7451
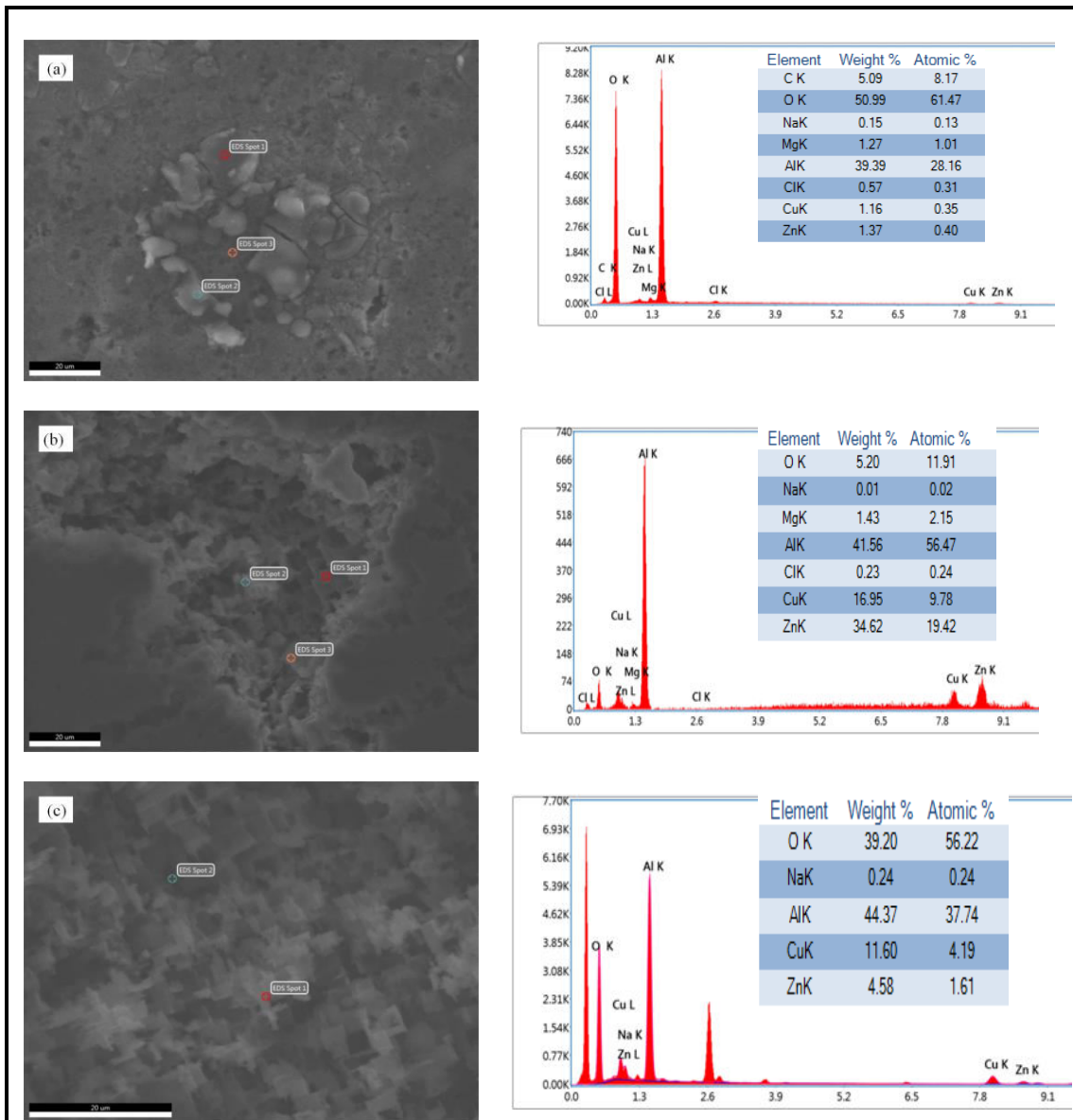
Fig. 7.17 SEM-EDS analysis performed on the corrosion products formed on different heat treated alloy samples; a) T6, b) RRA, c) T7451

The copper concentration on the matrix and on the grain boundary precipitates are analyzed by TEM-EDS and are reported in Fig. 7.18. It also shows an increase in the copper content in the matrix by about 52 % in RRA tempered alloy. This is attributed for observed resistance to corrosion attack. Hence the passive film formed on the RRA tempered alloy is more resistant to the pit formation and lesser anodic dissolution around the precipitates. Moreover the high temperature reversion is caused to have a redistribution of Cu in the matrix of RRA alloy. Whereas, in the T7451 condition alloy, though the average Cu content in the matrix is higher than that of the

T6, on the grain boundaries the Cu content is not uniform and hence higher standard deviation from the mean value is observed (Fig. 7.18).
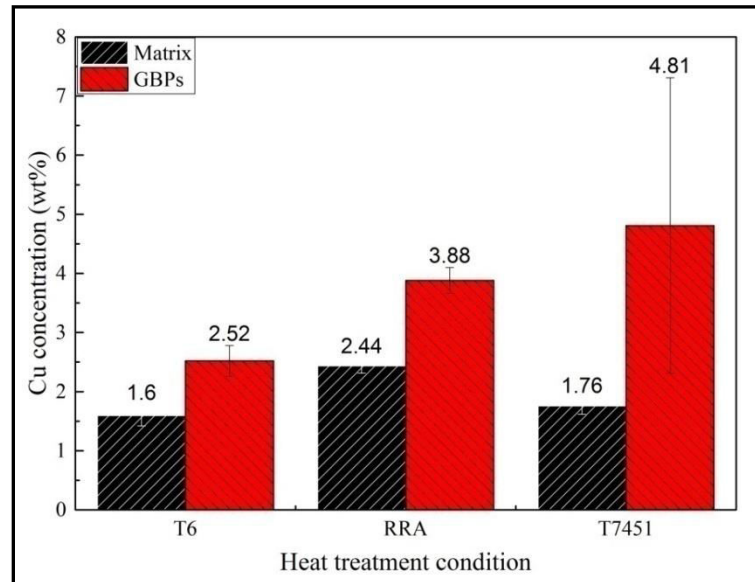
Fig. 7.18 TEM-EDS analysis carried on alloy samples with different tempers (evaluated from Fig. 7.20)

7.11 Exfoliation Corrosion Behavior

The exfoliated surfaces of the different tempered alloys after the EXCO test are observed as shown in Fig. 6.4. The morphologies of EXCO test samples were analyzed and rated from EA to EC according to ASTM G34 (ASTM G 34-01 2001). EA being the lowest exfoliated and EC being worst exfoliated with EA<EB<EC in the order of severity of exfoliation. The corrosion pit morphology of the T6 alloy indicates that it is being worst exfoliated compared to the RRA and the T7451 tempered alloys.
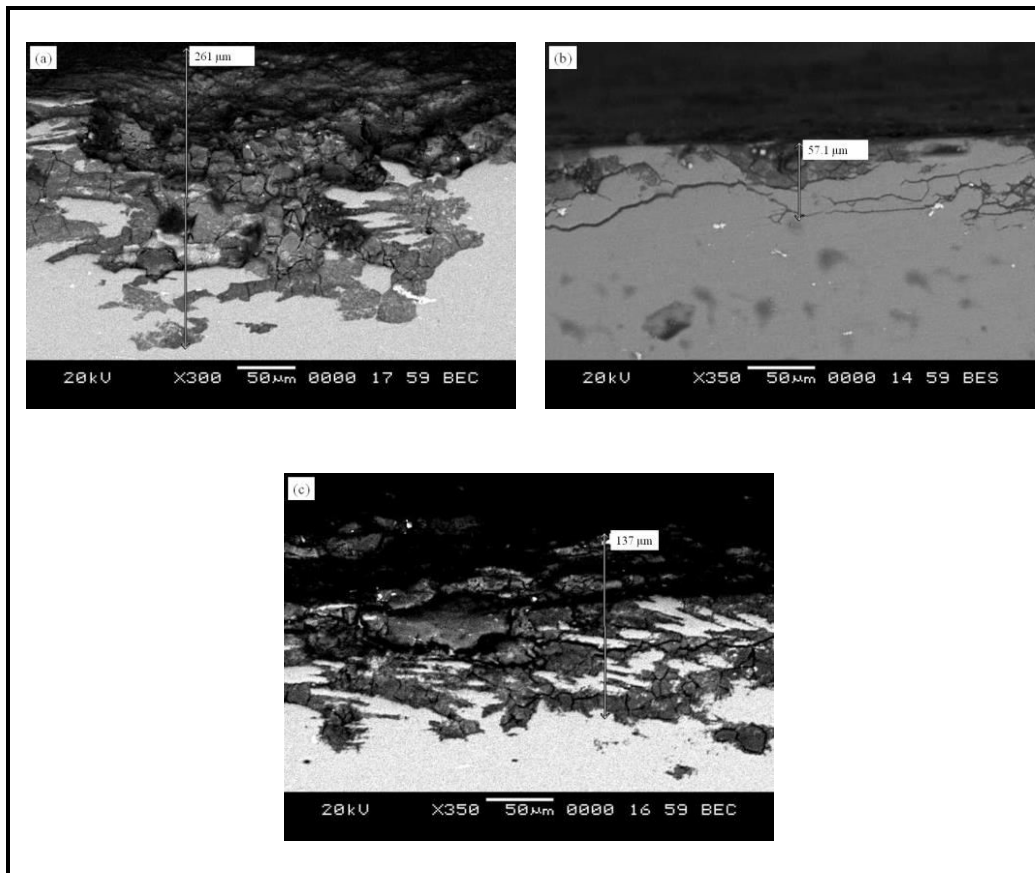
Fig. 7.19 SEM micrographs of the exfoliated surfaces of the alloy; a) T6, b) T7451, c) RRA

The cut section of the EXCO test samples is further observed under SEM to visualize the depth of penetration of corrosion attack. It is seen and justified in Fig. 7.19 that the T6 tempered alloy exhibited farthest corrosion attack measured up to a depth of around 250 μm from the EXCO test sample surface. The RRA treated alloy with 20 min of retrogression exhibits an exfoliation depth of 70-90 μm and T7451 treated alloy being 140 μm. The TEM-EDS analysis (Fig. 7.18, 7.20) also confirms that the average copper concentration on the GBP's increases from 2.52 wt% in T6 alloy to 3.88 wt% in the RRA tempered alloy. The increased concentration of copper on GBPs makes it less anodic with respect to the alloy matrix and hence contributes to the delay in anodic dissolution of the GBP's (Park and Ardell 1991). Though the Cu content is highest in T7451 condition the deviation from the average measured value is large and distribution is not consistent. It is also confirmed from SEM line EDS shown in Fig. 7.21 that the Cu content variation across the grain boundaries is

116

uniform in T6 tempered condition, which is found to vary after reversion treatment with a sharp spike in Cu content as measured in Fig. 7.21 b. This gives an additional evidence of higher copper concentration across the RRA GBP's.
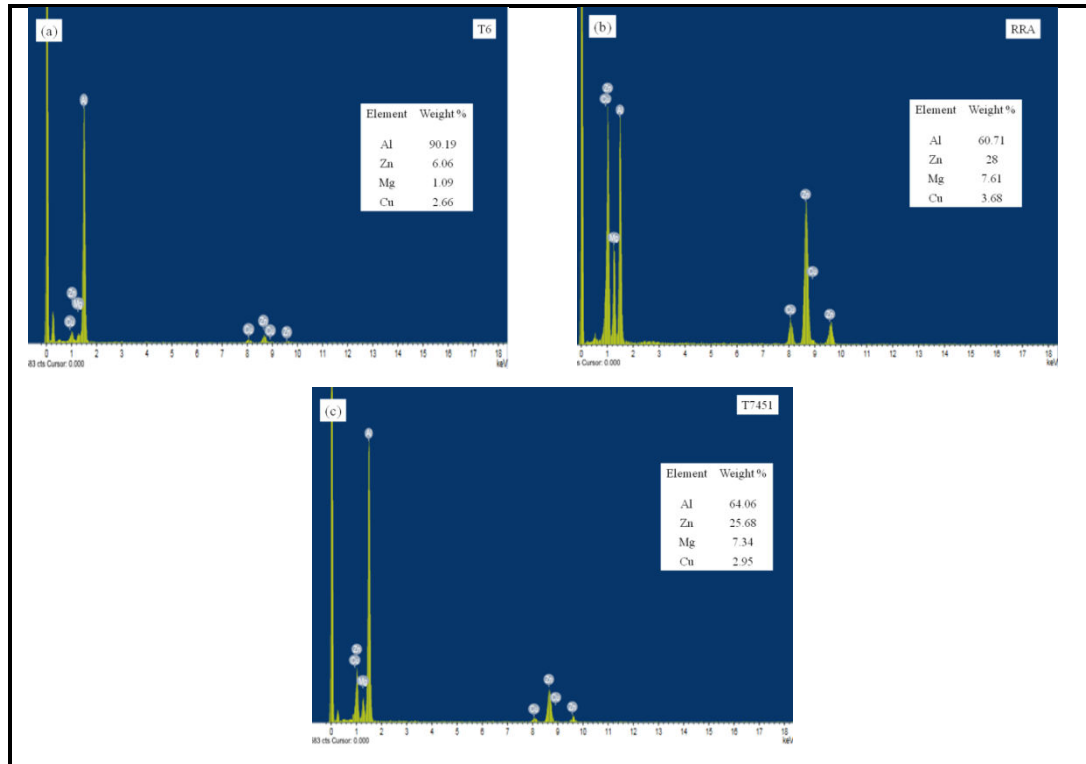
Fig. 7.20 TEM-EDS analysis carried on GBPs of alloys with different temper conditions; a) T6, b) RRA, c) T7451
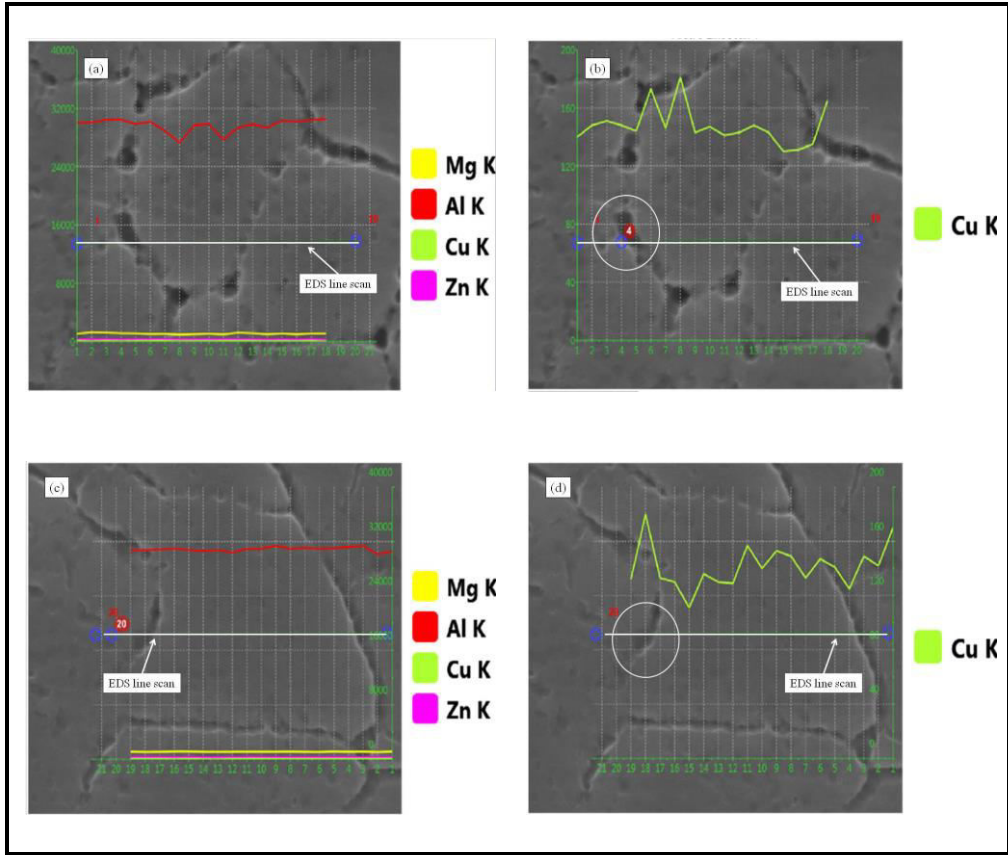
Fig. 7.21 SEM-EDS performed on alloys with different temper conditions; a, b) T6, c, d) RRA

CHAPTER 8

CONCLUSIONS

In the present study, a multi step heat treatment known as RRA was applied on the high strength Al-Zn-Mg-Cu alloy. This heat treatment was carried out by performing a high temperature reversion/retrogression treatment at 180-220 ˚C for various time intervals. The optimization of reversion temperature and duration of heat treatment was evaluated to be 200 ˚C for 20 minutes. The aim was to attain RRA treated alloy with ultimate tensile strength as equivalent to that of the T6 condition. Ultimately the microstructure of RRA treated alloy is supposed to have grain boundary characteristics similar to that of the T7451 condition. Thereby alloy acquires stress corrosion cracking resistance without losing the peak strength characteristics. Further, the effect of reversion treatment on the fatigue crack growth behavior was studied in detail and compared between the two different heat treatment conditions i.e., RRA and T6. Also, the performance of the treated alloys under aircraft service simulating fatigue loads like FALSTAFF was evaluated. Finally, the corrosion behavior and exfoliation corrosion behavior of the alloy was studied. Based on these experimental results and discussion, following conclusions are drawn:

- The RRA treatment with reversion carried for 20 min at 200 ˚C was concluded to be optimized parameter to obtain peak strength of 586 MPa that is equivalent or close to the T6 alloy strength i.e., 581 MPa.
- The matrix of RRA alloy was found to occupy with two different types of precipitates, one type of which were smaller in size ranging about 4-6 nm. Other type being, a larger size ranging about 12-20 nm. Though the precipitates were grown in size they still exhibit dislocation shearing mechanism.
- The grain boundaries of T6 treated alloy consists of $MgZn_2$ precipitates which were of continuous along the grain boundaries. Unlike T6, the RRA alloy was

consisting of discrete, disintegrated $MgZn_2$ precipitates enriched with Cu in them which was similar to the characteristics of an over-aged (T7451) alloy.

- The fracture toughness of RRA treated alloy was evaluated to be 41 MPa√m which was slightly reduced by a unit value when compared to the T6 treated alloy (42 MPa√m).

- A significant improvement in the performance of RRA treated alloy under constant amplitude fatigue crack growth tests was evident, such that an increase in threshold SIF by about 0.5-1.1 MPa√m was achieved in different stress ratio tests.

- The fatigue crack growth rate was significantly reduced in the near-threshold regime of fatigue crack growth curve by about 2-3 times after RRA treatment when compared to the crack growth rate in standard T6 treated alloy.

- The improvement in the resistance to crack propagation was evidenced and supported by the enhanced damage tolerant characteristics when tested under service simulating loads like FALSTAFF. The RRA alloy exhibited a 22 % improvement in fatigue crack growth life. The RRA test specimen served for about 59 blocks of loads when compared to 48 blocks loads under T6 condition.

- The fatigue crack growth predicted for FALSTAFF loading, using the CA FCGR data also matched fairly well with the experimentally determined crack growth behavior.

- The corrosion resistance of the RRA treated alloy was much higher compared to T6 alloy in terms of corrosion current density which was reduced by about 50 %. Also, the corrosion potential of RRA alloy shifted towards noble direction, thereby reducing the number of pit formation. The total passive film resistance of the RRA treated alloy was higher by about 22 % when compared to that of the T6 alloy.

- Exfoliation corrosion resistance of the alloy was also increased after the RRA treatment. The depth of corrosion attack was reduced to 70-90 μm when compared to 250 μm depth observed for the T6 alloy.

- The redistribution of Cu in the matrix and enrichment of Cu on the grain boundary precipitates by about 50 % has caused the enhanced resistance to corrosion and exfoliation corrosion after RRA treatment.

Scope for future work

In the present study, RRA treatment with retrogression treatment was optimized for alloy 7010 up to a thickness of 15 mm. Based on the section thickness mechanical, fatigue and microstructural characterization following studies could be considered for future work.

- The fatigue studies such as corrosion fatigue behavior of RRA treated alloy could be one of the important studies applied to the aircraft industry.
- Stress corrosion crack studies on the RRA treated alloy under slow strain rate conditions could be carried out in future.
- In situ studies such as precipitate coarsening effect during reversion treatment as a microstructural characterization could be carried in future.
- The effect of retrogression heating rate on various mechanical and fatigue properties could be studied.

REFERENCES

Adler, P. N., Delasi, R., and Geschwind, G. (1972). "Influence of microstructure on the mechanical properties and stress corrosion susceptibilty of 7075 aluminum alloy." *Metall. Trans.*, 3(12), 3191–3200.

Al-Rubaie, K. S., Barroso, E. K. L., and Godefroid, L. B. (2005). "Fatigue crack growth analysis of pre-strained 7475–T7351 aluminum alloy." *Int. J. Fatigue*, 28, 934–942.

Andersen, S. J., Marioara, C. D., Friis, J., Wenner, S., and Holmestad, R. (2018). "Precipitates in aluminum alloys." *Adv. Phys. X*, 3(1), 790–814.

Angappan, M., Sampath, V., Ashok, B., and Deepkumar, V. P. (2011). "Retrogression and re-aging treatment on short transverse tensile properties of 7010 aluminum alloy extrusions." *Mater. Des.*, 32(7), 4050–4053.

ASM Handbook Vol 3. (2004). *Alloy Phase Diagrams*. American Society for Metals.

ASTM E1049-85. (2011). "Standard practices for cycle counting in fatigue analysis." *Annu. B. ASTM Stand. West Conshohocken, PA*, 85(Reapproved 2011), 1–10.

ASTM E399. (2013). "Standard test method for linear-elastic plane-strain fracture toughness K1C of metallic material." *ASTM Int.*, 1–33.

ASTM E8. (2010). "ASTM E8/E8M standard test methods for tension testing of metallic materials 1." *ASTM Int.*, (C), 1–27.

ASTM G 34-01. (2001). "Standard test method for exfoliation corrosion susceptibility in 2XXX and 7XXX series aluminum alloys (EXCO Test) 1." *ASTM Int.*, 11, 1–7.

Austral Wright Metals. (2014). *Introduction to aluminum and aluminum alloys*.

Bobby Kannan, M., Raja, V. S., Raman, R., and Mukhopadhyay, A. K. (2003). "Influence of multistep aging on the stress corrosion cracking behavior of aluminum alloy 7010." *Corrosion*, 59(10), 881–889.

Bora, C. (1974). "Reducing the susceptiibility of alloys, particularly aluminum alloys,

to stress corrosion cracking."

Borrego, L. P., Costa, J. M., Antunes, F. V., and Ferreira, J. M. (2010). "Fatigue crack growth in heat-treated aluminum alloys." *Eng. Fail. Anal.*, 17(1), 11–18.

Borrego, L. P., Costa, J. M., Silva, S., and Ferreira, J. M. (2004). "Microstructure dependent fatigue crack growth in aged hardened aluminum alloys." *Int. J. Fatigue*, 26(12), 1321–1331.

Braga, D. F. O., Tavares, S. M. O., Silva, L. F. M. Da, Moreira, P. M. G. P., and Castro, P. M. S. T. De. (2014). "Advanced design for lightweight structures: Review and prospects." *Prog. Aerosp. Sci.*, 69, 29–39.

Buha, J., Lumley, R. N., and Crosky, A. G. (2008). "Secondary ageing in an aluminum alloy 7050." *Mater. Sci. Eng. A*, 492(1-2), 1–10.

Carvalho, A. L. M. de, and Martins, J. de P. (2018). "Effect of interrupted ageing and retrogression-reageing treatments on fatigue crack growth with a single applied overload in 7050 aluminum alloy." *Mater. Res.*, 21(3), 1–13.

Chemin, A. E. A., Saconi, F., Bose Filho, W. W., Spinelli, D., and Ruchert, C. O. F. T. (2015). "Effect of saline corrosion environment on fatigue crack growth of 7475-T7351 aluminum alloy under TWIST flight loading." *Eng. Fract. Mech.*, 141, 274–290.

Chen, D. L., and Chaturvedi, M. C. (2000). "Near-threshold fatigue crack growth behavior of 2195 aluminum-lithium-alloy�prediction of crack propagation direction and influence of stress ratio." *Metall. Mater. Trans. A*, 31(6), 1531–1541.

Chen, X., Liu, Z., Lin, M., Ning, A., and Zeng, S. (2012). "Enhanced fatigue crack propagation resistance in an Al-Zn-Mg-Cu alloy by retrogression and reaging treatment." *J. Mater. Eng. Perform.*, 21(11), 2345–2353.

Chen, X., Liu, Z., Xia, P., Ning, A., and Zeng, S. (2013a). "Transition of crack propagation from a transgranular to an intergranular path in an overaged Al-Zn-Mg-Cu alloy during cyclic loading." *Met. Mater. Int.*, 19(2), 197–203.

Chen, Y., Weyland, M., and Hutchinson, C. R. (2013b). "The effect of interrupted aging on the yield strength and uniform elongation of precipitation-hardened Al alloys." *Acta Mater.*, 61(15), 5877–5894.

Costa, J. D., and Ja, M. (2017). "Plasticity induced closure under variable amplitude loading in AlMgSi aluminum alloys." *2nd Int. Conf. Struct. Integrity, ICSI 2017, 4-7 Sept. 2017, Funchal, Madeira, Port.*

Danh, N. C., Rajan, K., and Wallace, W. (1983). "A TEM study of microstructural changes during retrogression and reaging in 7075 aluminum." *Metall. Trans. A*, 14(9), 1843–1850.

Deshpande, N. U., Gokhale, A. M., Denzer, D. K., and Liu, J. (1998). "Relationship between fracture toughness, fracture path, and microstructure of 7050 aluminum lloy: Part I. Quantitative characterization." *Metall. Mater. Trans. A*, 29(4), 1191–1201.

Desmukh, M. N., Pandey, R. K., and Mukhopadhyay, A. K. (2006). "Effect of aging treatments on the kinetics of fatigue crack growth in 7010 aluminum alloy." *Mater. Sci. Eng. A*, 435-436, 318–326.

Dinda, S., and Kujawski, D. (2004). "Correlation and prediction of fatigue crack growth for different R-ratios using Kmaxand ∆K+parameters." *Eng. Fract. Mech.*, 71(12), 1779–1790.

Dorward, R. C., and Beerntsen, D. (1995). "Grain structure and quench-rate effects on strength and toughness of AA7050 Al-Zn-Mg-Cu-Zr alloy plate." *Metall. Mater. Trans. A*, 26(9), 2481–2484.

Elber W. (1970). "Fatigue crack closure under cyclic tension." *Eng. Fract. Mech.*, 2(1), 37–45.

Feng Chun, Liu Zhi-yi, Ning Ai-lin, Liu Yan-bin, Z. S. (2006). "Retrogression and re-aging treatment of A1-9.99YoZn- 1.72%Cu-2.5%Mg-O. 13%Zr aluminum alloy." *Trans. Nonferrous Met. Soc. China*, 16, 1163–1170.

Ge, F., Moshe, Z., Li, J., and Tan, L. (2001). "GP-zones in Al-Zn-Mg alloys and their

role in artificial aging." *Acta Mater.*, 49(2001), 3443–3451.

Gysler, A., and Lindigkeit, J. (1981). "The Effect of Microstructure on the Fatigue Crack Propagation Behavior of an AI-Zn-Mg-Cu Alloy." 12(September), 1613–1619.

Han, N. M., Zhang, X. M., Liu, S. D., Ke, B., and Xin, X. (2011). "Effects of pre-stretching and ageing on the strength and fracture toughness of aluminum alloy 7050." *Mater. Sci. Eng. A*, 528(10-11), 3714–3721.

Hertzberg, R., Newton, C., and Jaccard, R. (1988). "Crack closure: correlation and confusion." *Mech. Fatigue Crack Clos.*, 139–148.

Heuler, P., and Klatschke, H. (2005). "Generation and use of standardised load spectra and load-time histories." *Int. J. Fatigue*, 27(8), 974–990.

Holt, R. T., Raizenne, M. D., Wallace, W., and DuQuesnay, D. L. (1999). "RRA heat treatment of large Al 7075-T6 components." *New Met. Mater. Struct. Aging Aircr.*, 7.1–7.11.

Kamp, N., Sinclair, I., and Starink, M. J. (2002). "Toughness-strength relations in the overaged 7449 Al-based alloy." *Metall. Mater. Trans. A*, 33(4), 1125–1136.

Kanno, M., and Araki, I. (1994). "Precipitation behaviour of 7010 alloys during retrogression and reaging treatment." *Mater. Sci. Technol.*, 10(July), 599–603.

Kovács, I., Lendvai, J., Ungar, T., Groma, G., and Lakner, J. (1980). "Mechanical properties of AlZnMg alloys." *Acta Metall.*, 28(12), 1621–1631.

Kujawski, D. (2001a). "A fatigue crack driving force parameter with load ratio effects." *Int. J. Fatigue*, 23, S239–S246.

Kujawski, D. (2001b). "Enhanced model of partial crack closure for correlation of R-ratio effects in aluminum alloys." *Int. J. Fatigue*, 23(2), 95–102.

Li, B., Wang, X., Chen, H., Hu, J., Huang, C., and Gou, G. (2016). "Influence of heat treatment on the strength and fracture toughness of 7N01 aluminum alloy." *J. Alloys Compd.*, 678, 160–166.

LI, G., ZHANG, X., LI, P., and YOU, J. (2010). "Effects of retrogression heating rate on microstructures and mechanical properties of aluminum alloy 7050." *Trans. Nonferrous Met. Soc. China*, 20(6), 935–941.

Li, Y., Wang, H., and Gong, D. (2012). "The interrelation of the parameters in the paris equation of fatigue crack growth." *Eng. Fract. Mech.*, 96, 500–509.

Lim, S. T., Eun, I. S., and Nam, S. W. (2003). "Control of Equilibrium Phases (M,T,S) in the Modified Aluminum Alloy 7175 for Thick Forging Applications." *Mater. Trans.*, 44(1), 181–187.

Löffler, H., Kovács, I., and Lendvai, J. (1983). "Decomposition processes in Al-Zn-Mg alloys." *J. Mater. Sci.*, 18(8), 2215–2240.

Ma, K., Wen, H., Hu, T., Topping, T. D., Isheim, D., Seidman, D. N., Lavernia, E. J., and Schoenung, J. M. (2014). "Mechanical behavior and strengthening mechanisms in ultrafine grain precipitation-strengthened aluminum alloy." *Acta Mater.*, 62, 141–155.

Manjunatha, C. M. (2008). "Fatigue crack growth prediction under spectrum load sequence in an aluminum alloy by K*-RMS approach." *Int. J. Damage Mech.*, 17(6), 477–492.

Marlaud, T., Deschamps, A., Bley, F., Lefebvre, W., and Baroux, B. (2010a). "Evolution of precipitate microstructures during the retrogression and re-ageing heat treatment of an Al-Zn-Mg-Cu alloy." *Acta Mater.*, 58(14), 4814–4826.

Marlaud, T., Deschamps, A., Bley, F., Lefebvre, W., and Baroux, B. (2010b). "Influence of alloy composition and heat treatment on precipitate composition in Al-Zn-Mg-Cu alloys." *Acta Mater.*, 58(1), 248–260.

McClung, R. C. (1991). "The influence of applied stress, crack length, and stress intensity factor on crack closure." *Metall. Trans. A*, 22(7), 1559–1571.

Meng, C. F., Long, H. W., and Zheng, Y. (1997). "A study of the mechanism of hardness change of Al-Zn-Mg alloy during retrogression reaging treatments by small angle X-ray scattering (SAXS)." *Metall. Mater. Trans. a-Physical Metall. Mater. Sci.*,

28(10), 2067–2071.

Mukhopadhyay, A. K. (1994). "Guinier-preston zones in a high-purity al-zn-mg alloy." *Philos. Mag. Lett.*, 70(3), 135–140.

Newman, J. (1981). "A crack-closure model for predicting fatigue crack growth under aircraft spectrum loading." *Methods Model. Predict. fatigue crack growth under random loading, STP748-EB, Chang. J. Hudson, C., Ed., ASTM Int. West Conshohocken, PA*, 748, 53–84.

Ogura, T., Hirosawa, S., Cerezo, A., and Sato, T. (2006). "Quantitative correlation between strength, ductility and precipitate microstructures with PFZ in Al-Zn-Mg(-Ag, Cu) alloys." *Mater. Sci. Forum*, 519-521, 431–436.

Ogura, T., Hirosawa, S., Hirose, A., and Sato, T. (2011). "Effects of microalloying tin and combined addition of silver and tin on the formation of precipitate free zones and mechanical properties in Al-Zn-Mg alloys." *Mater. Trans.*, 52(5), 900–905.

Paris, P., and Erdogan, F. (1963). "A critical analysis of crack propagation laws." *J. Basic Eng.*, 85(4), 528.

Park, J. K., and Ardell, A. J. (1984). "Effect of retrogression and reaging treatments on the microstructure of Ai-7075-T651." *Metall. Mater. Trans. A*, 15(8), 1531–1543.

Park, J. K., and Ardell, A. J. (1991). "Microchemical analysis of precipitate free zones in 7075-A1 in the T6, T7 and RRA tempers." *Acta Metall. Mater.*, 39(4), 591–598.

Peng, G., Chen, K., Chen, S., and Fang, H. (2011). "Influence of repetitious-RRA treatment on the strength and SCC resistance of Al-Zn-Mg-Cu alloy." *Mater. Sci. Eng. A*, 528(12), 4014–4018.

Pokorny, P., Vojtek, T., Nahlik, L., and Hutar, P. (2017). "Crack closure in near-threshold fatigue crack propagation in railway axle steel EA4T." *Eng. Fract. Mech.*, 185, 2–19.

Reda, Y., Abdel-Karim, R., and Elmahallawi, I. (2008). "Improvements in mechanical and stress corrosion cracking properties in Al-alloy 7075 via retrogression and

reaging." *Mater. Sci. Eng. A*, 485(1-2), 468–475.

Ricardo, L. C. H., and Miranda, C. A. J. (2016). "Crack simulation models in variable amplitude loading - a review." *Frat. ed Integrita Strutt.*, 10(35), 456–471.

Ringer, S. P., and Hono, K. (2000). "Microstructural evolution and age hardening in aluminum alloys: atom probe field-ion microscopy and transmission electron microscopy studies." *Mater. Charact.*, 44(1-2), 101–131.

Ritchie, R. O. (1988). "Mechanisms of fatigure crack propagation in metals, ceramics, and composites: Role of crack tip shielding." *Mater. Sci. Eng. A*, 103(1), 15–28.

Robinson, P. (1990). *Properties of wrought coppers and copper alloys*. ASM International.

Rometsch, P. A., Zhang, Y., and Knight, S. (2014). "Heat treatment of 7xxx series aluminum alloys - some recent developments." *Trans. Nonferrous Met. Soc. China*, 24(7), 2003–2017.

Rout, P. K., Ghosh, M. M., and Ghosh, K. S. (2015a). "Microstructural, mechanical and electrochemical behaviour of a 7017 Al-Zn-Mg alloy of different tempers." *Mater. Charact.*, 104, 49–60.

Rout, P. K., Ghosh, M. M., and Ghosh, K. S. (2015b). "Microstructural, mechanical and electrochemical behaviour of a 7017 Al – Zn – Mg alloy of different tempers." *Mater. Charact.*, 104, 49–60.

Schijve, J. (2001). *Fatigue of structures and materials*. United States of America.

Schijve, J. (2009). "Fatigue damage in aircraft structures, not wanted, but tolerated?" *Int. J. Fatigue*, 31(6), 998–1011.

Sree, P. C. R., and Kujawski, D. (2014). "A two-parameter fatigue crack growth correlation uing ΔK and Kmax parameters." *Proc. ASME 2014 Int. Mech. Eng. Congr. Expo. IMECE2014*, 11–14.

Srivatsan, T. S., Sriram, S., Veeraraghavan, D., and Vasudevan, V. K. (1997).

"Microstructure, tensile deformation and fracture behaviour of aluminum alloy 7055." *J. Mater. Sci.*, 32(11), 2883–2894.

Suresh, S. (1998). *Fatigue of Materials*.

Talianker, M., and Cina, B. (1989). "Retrogression and reaging and the role of dislocations in the stress corrosion of 7000-type aluminum alloys." *Metall. Trans. A*, 20(10), 2087–2092.

Vasudevan, A. K., and Sadananda, K. (1995). "Analysis of fatigue crack closure and thresholds." *Fract. Mech. Am. Soc. Test. Mater. STP 1220*, 25, 484–501.

Vasudevan, A. K., Sadananda, K., and Iyyer, N. (2016). "Fatigue damage analysis : Issues and challenges." *Int. J. Fatigue*, 82, 120–133.

Vasudeven, A. K., Sadananda, K., Louat, N., A.K Vasudeven, K. Sadananda, and N. Louat. (1994). "A review of crack closure, fatigue crack threshold and related phenomena." *Mater. Sci. Eng.*, 188(1-2), 1–22.

Viana, F., Pinto, A. M. P., Santos, H. M. C., and Lopes, A. B. (1999). "Retrogression and re-ageing of 7075 aluminum alloy: microstructural characterization." *J. Mater. Process. Technol.*, 92-93, 54–59.

Walker, K. (1970). "The effect of stress ratio during crack propagation and fatigue for 2024-T3 and 7075-T6 aluminum." *ASTM STP 462, Am. Soc. Test. Mater.*, 1–14.

Wang, T., Yin, Z. min, Shen, K., Li, J., and Huang, ji wu. (2007). "Single-aging characteristics of 7055 aluminum alloy." *Trans. Nonferrous Met. Soc. China*, 17(3), 548–552.

Wang, Y. L., Pan, Q. L., Wei, L. L., Li, B., and Wang, Y. (2014). "Effect of retrogression and reaging treatment on the microstructure and fatigue crack growth behavior of 7050 aluminum alloy thick plate." *Mater. Des.*, 55, 857–863.

Williamson, G. K., and Smallman, R. E. (1956). "III. Dislocation densities in some annealed and cold-worked metals from measurements on the X-ray debye-scherrer spectrum." *Philos. Mag. A J. Theor. Exp. Appl. Phys.*, 1(1), 34–46.

Wu, M., Wen, L., Tang, B., Peng, L., and Ding, W. (2010). "First-principles study of elastic and electronic properties of MgZn 2 and ScZn 2 phases in Mg – Sc – Zn alloy." 506, 412–417.

Xia, P., Liu, Z., Bai, S., Lu, L., and Gao, L. (2016). "Enhanced fatigue crack propagation resistance in a superhigh strength Al–Zn–Mg–Cu alloy by modifying RRA treatment." *Mater. Charact.*, 118, 438–445.

YANG, R. xian, LIU, Z. yi, YING, P. you, LI, J. lin, LIN, L. hua, and ZENG, S. min. (2016). "Multistage-aging process effect on formation of GP zones and mechanical properties in Al–Zn–Mg–Cu alloy." *Trans. Nonferrous Met. Soc. China*, 26(5), 1183–1190.

Zhao, Z., Zhang, H., Li, Y., Chen, X., and Liu, Y. (2019). "Effect of static mechanical load on intergranular stress-corrosion cracking of 7050-T7451 C-Ring specimens." *Corros. Eng. Sci. Technol.*, 54(2), 122–130.
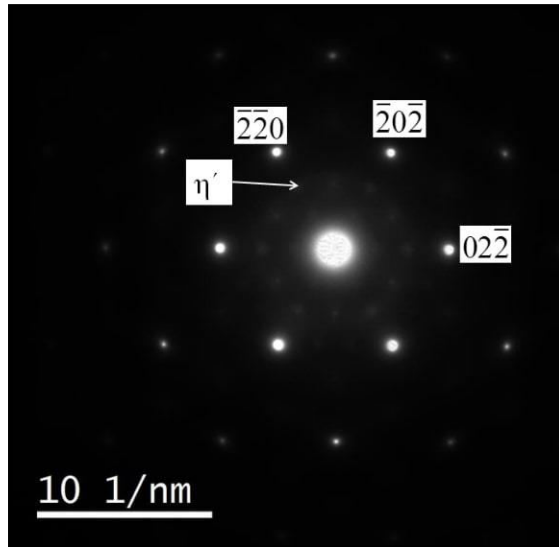
Fig. A1-1 SAED pattern from the 7010 alloy in T6 treated condition
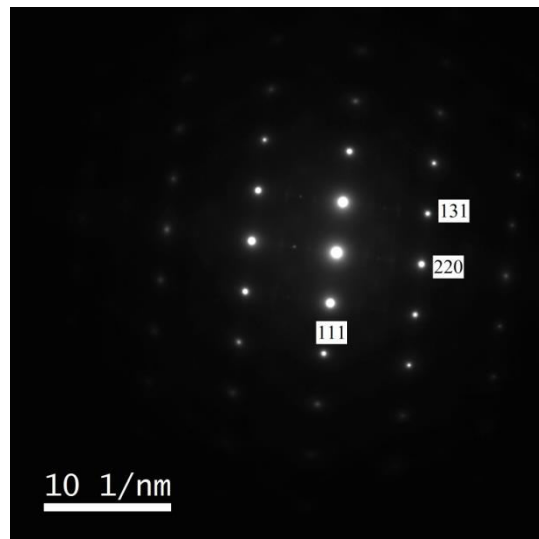
Fig. A1-2 SAED pattern from the 7010 alloy in RRA (60 min reversion) [112 zone axis]
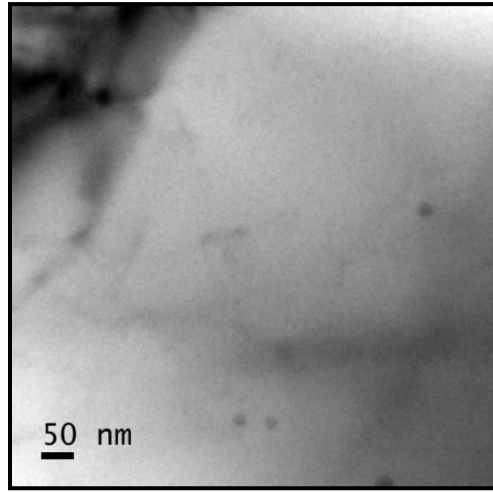
Fig. A1-3 TEM micrograph of alloy solution treated at 490 °C for 6 hrs
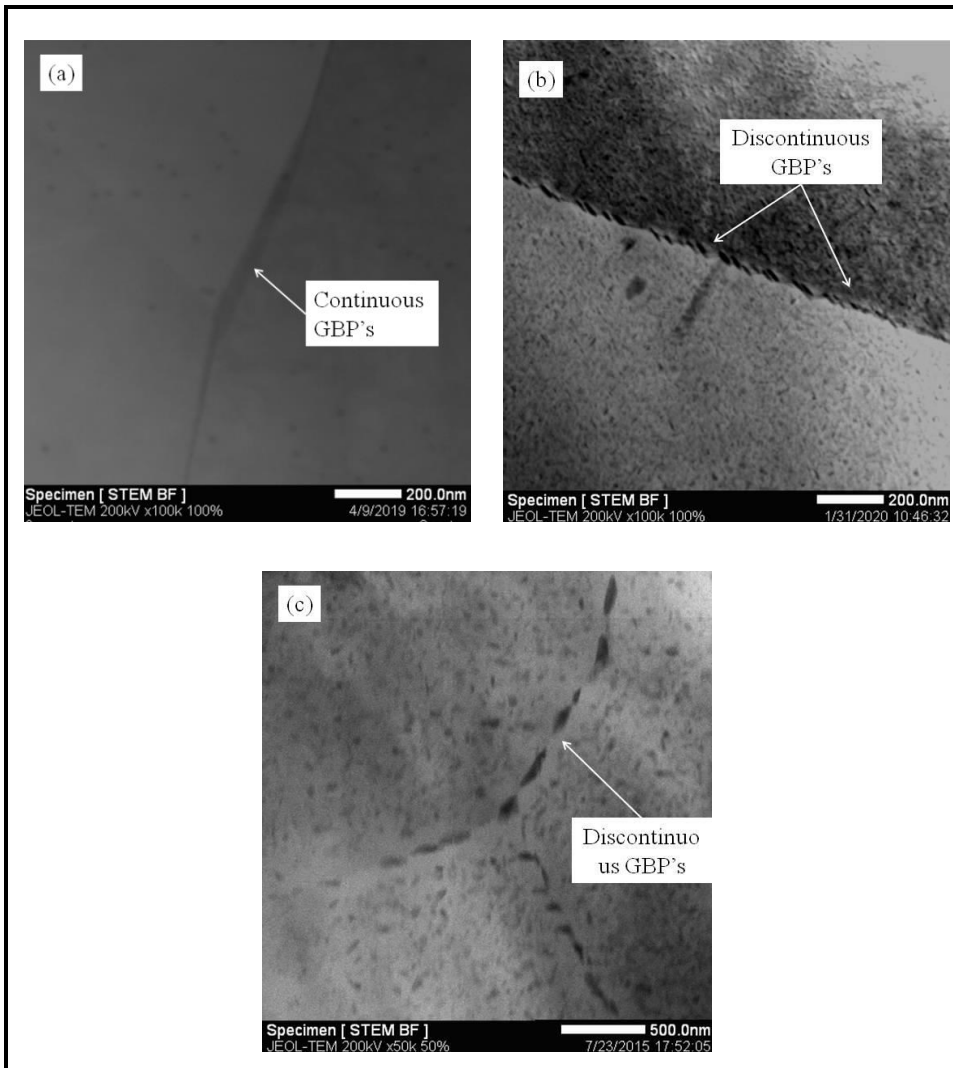

Fig. A1-4 STEM micrographs of the alloy; a) T6, b) RRA, c) T7451

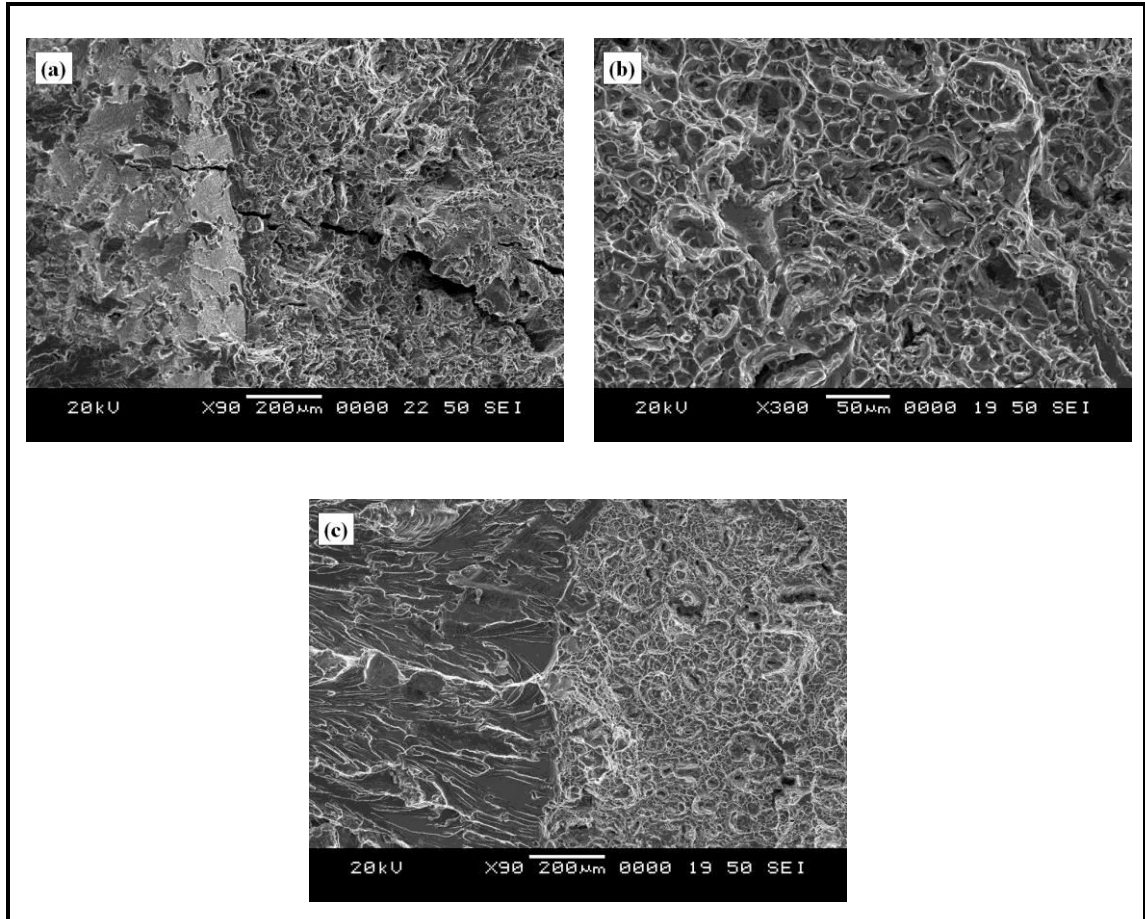**APPENDIX II:** Fractographs of test samples

Fig. A2-1 Fractography of CT samples tested for fracture toughness test; a) T6, b) RRA, c) T7451
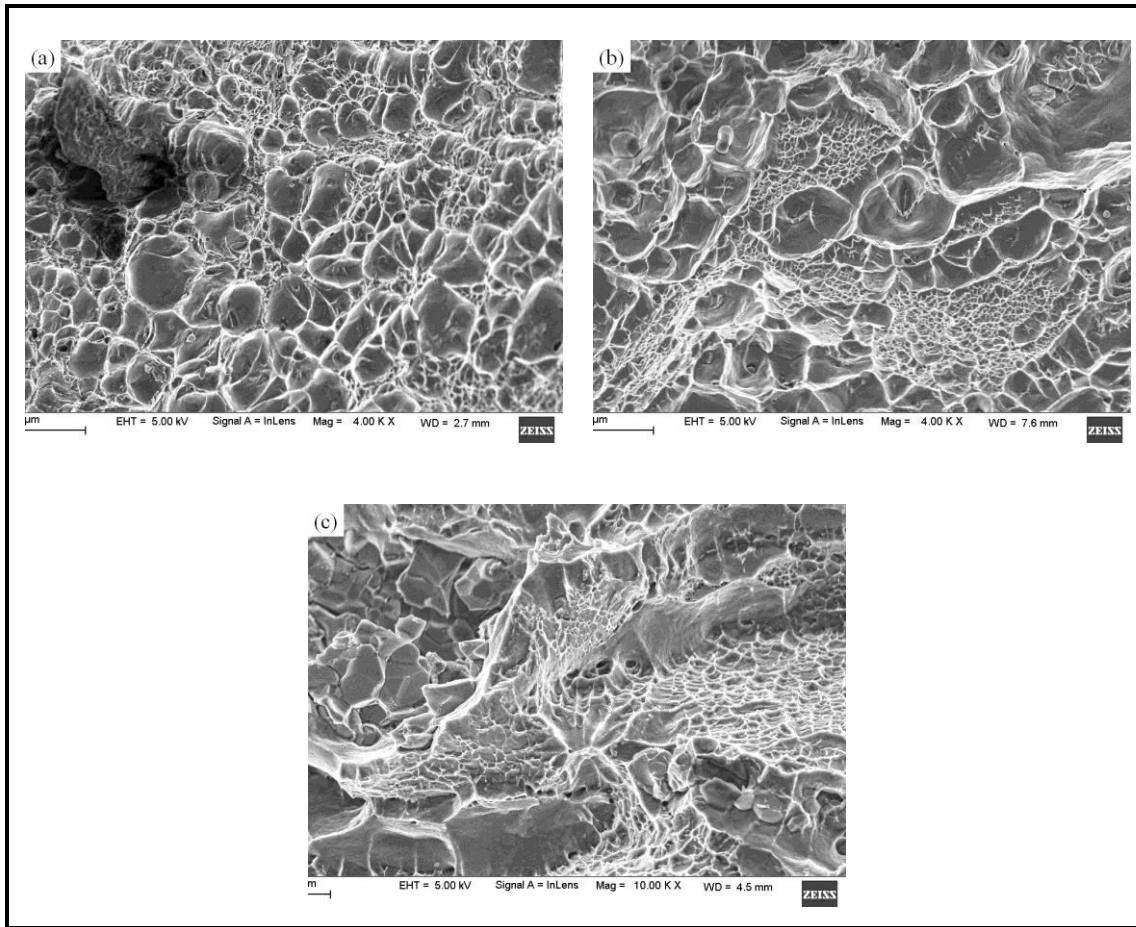
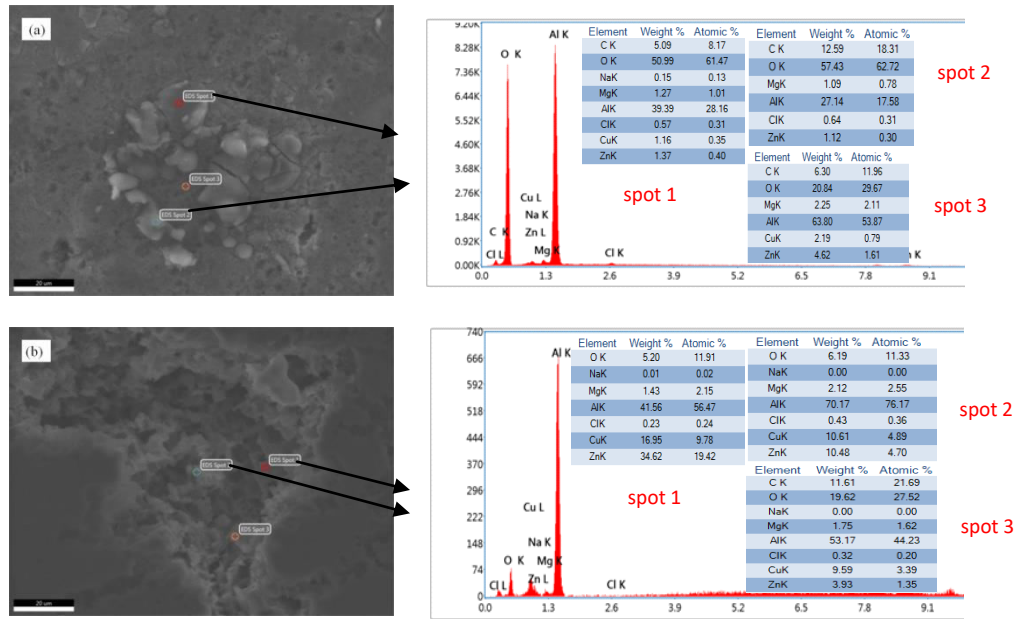Fig. A2-2 Fractography of tensile test samples; a) T6, b) RRA, c) T7451

Fig. A2-3 SEM-EDS analysis on the corrosion products formed on different tempered alloys; a) T6, b) RRA

APPENDIX III: VBA code used for crack growth prediction under FALSTAFF
loading

```vba
Sub Calculate11()

Dim i As Integer
Dim original_peak As Double
Dim load, load1, j, dp, original_peak1, pmax, w, b, a, aw,
faw, dk, r, rt, alpha, beta, gama, f1, f2, dkstr, c1, c2, c3,
dkth, f3, f4, f5, dabydn, da As Double

Dim x As Integer

w = 0.0505
b = 0.0125
rt = 0.33
alpha = 0.66
beta = 0.34
c1 = 0.00000000004
c2 = 3.1
dkth = 10.3
c3 = 30
'original_peak = Sheets("mini-FALSTAFF").Range("A2").Value
'load1 = original_peak * 20000
a = 0.012


For x = 1 To 2


For i = 3 To 18013
'i = 3
original_peak = Sheets("sheet").Range("A" & i & "").Value
'MsgBox ("orginal peak is " & original_peak & "")
j = i - 1
original_peak1 = Sheets("sheet").Range("A" & j & "").Value
'Dim load1, load2
'MsgBox ("orginal peak1 is " & original_peak1 & "")
load1 = original_peak * 15000
load2 = original_peak1 * 15000

'load = load2 - load1


'MsgBox ("load is" & load & "")
dp = load2 - load1
dp = Abs(dp)
'MsgBox ("dp" & dp & "")
    If load2 > load1 Then
    pmax = load2
Else
pmax = load1
End If
'MsgBox ("pmax is" & pmax & "")
```

```
aw = a / w
'MsgBox ("aw is" & aw & "")
faw = ((2 + aw) * (0.886 + (4.64 * aw) - (13.32 * aw ^ 2) +
(14.72 * aw ^ 3) - (5.6 * aw ^ 4)) / (1 - aw) ^ 1.5)
'MsgBox ("faw is" & faw & "")
dk = ((dp * faw) / (b * (w ^ 0.5)) / 1000000)
'MsgBox ("dk is" & dk & "")
r = (1 - (dp / pmax))
'MsgBox ("r is" & r & "")

If r > rt Then
gama = alpha
Else
gama = beta
End If

f1 = ((1 - rt) / (1 - r))

f1 = Abs(f1)

f2 = f1 ^ gama
dkstr = dk * f2
f3 = (1 - (dkth / dkstr) ^ 2)

f3 = Abs(f3)
f4 = (1 - (dkstr / c3) ^ 2)

f5 = f3 / f4

dabydn = (c1 * (dkstr ^ c2) * f5)
da = dabydn * 0.5
a = da + a


Next
Next

MsgBox ("" & a & "")
End Sub
```

Page intentionally left blank

List of Publications based on PhD research work

Sl. No	Title of the paper	Authors (in the same order as in the paper, Underline the Research Scholar's name)	Name of the Journal/Conference/ Symposium, Vol., No., Pages	Month and Year of Publication	Category
1.	Effect of retrogression heat-treatment time on microstructure and mechanical properties of AA7010	Nandana, M. S., Udaya Bhat, K., and Manjunatha, C. M	Journal of Materials Engineering and Performance, Springer Vol 27, Page: 1628–1634	April 2018	1
2.	Improved fatigue crack growth resistance by retrogression and re-aging heat-treatment in 7010 aluminum alloy	Nandana, M. S., Udaya Bhat, K., and Manjunatha, C. M	Fatigue & Fracture of Engineering Materials & Structures, Wiley Vol 42, Page: 719-731	October 2018	1
3.	Electrochemical and Exfoliation Corrosion Behavior of Reversion Treated High Strength Aluminum Alloy	Nandana, M. S., Udaya Bhat, K., Manjunatha, C. M and Shashi Bhushan Arya	Transactions of Indian Institute of Metals, Springer Vol 73, Page:1489-1495	March 2020	1
4.	Damage tolerance capability of retrogression and re-aged 7010 aluminum alloy under FALSTAFF loading	Nandana, M. S., Udaya Bhat, K., and Manjunatha, C. M	Transactions of Indian Institute of Metals, Springer Vol 73, Page: 1073-1080	March 2020	1
5.	Influence of retrogression and re-aging heat-treatment on the fatigue crack growth behavior of 7010 aluminum alloy	Nandana, M. S., Udaya Bhat, K., and Manjunatha, C. M	Procedia Structural Integrity, Elsevier Vol 14, Pages: 314-321	January 2019	3
6.	Effect of microstructure on the fatigue crack growth behavior in Al-Zn-Mg-Cu alloy	Nandana, M. S., Udaya Bhat, K., and Manjunatha, C. M	Lecture Notes in Mechanical Engineering, Springer, Vol 2195-4356, Pages: 545-554	July 2019	3
7.	Influence of heat-treatment on the near-threshold fatigue crack growth behavior in high strength Aluminum alloy 7010	Nandana, M. S., Udaya Bhat, K., and Manjunatha, C. M	Lecture Notes in Mechanical Engineering, Springer, Vol 1, Pages: 444-451	June 2019	3
8.	Effect of retrogression and re-aging heat-treatment on microstructure and microhardness of Aluminum 7010 alloy	Nandana, M. S., Udaya Bhat, K., and Manjunatha, C. M	Proc., Int. Symp. on Rimes. MATEC Web of Conference, Vol 144, Page: 02003	June 2018	3
9.	Effect of Retrogression Duration on the Grain Boundary Microstructure and Microchemistry of AA7010	Nandana, M. S., Udaya Bhat, K., and Manjunatha, C. M	AIP Conference Proceedings Vol 1943, Page: 020085	April 2018	3

<superscript>*</superscript> Category: 1: Journal paper, full paper reviewed

                   2: Journal paper, Abstract reviewed

                   3: Conference/Symposium paper, full paper reviewed

                   4: Conference/Symposium paper, abstract reviewed

                   5: others (including papers in Workshops, NITK Research Bulletins, short notes etc.)

(If the paper has been accepted for publication but yet to be published, the supporting documents must be attached.)

Research Scholar   **Research Guides**

(Nandana M S)   (Prof. Udaya Bhat K)   (Dr. Manjunatha C M)

Date: Date: Date:

140

BIO DATA

Name	: Nandana M S.
Father's Name	: Shivarama M
Date of birth	: 01-02-1988
Permanent address	: # 121 Shedikare House, Kalmadka Post Sullia Taluk Dakshina Kannada District Mangalore -574212
Mobile	: +91-9483922501/8073083034
Email ID	nandanams88@gmail.com

Academic qualification:

Bachelor of Engineering (B.E) in Mechanical Engineering from Sri Jayachamarajendra College of Engineering Mysore (2009).

Master of Technology (M.Tech) in Machine Design from R.V college of Engineering Bangalore (2014)).

Work Experience: 3 years of work experience in TCS Bangalore.

Google Scholar Citations

No. of publications: 9

Total citations: 20

h-index: 2